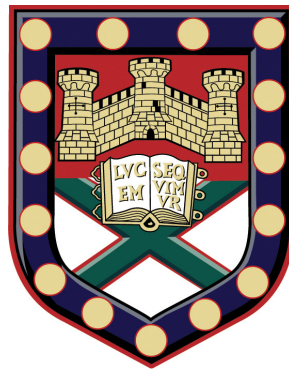


Two dimensional atomically thin materials and hybrid superconducting devices



David Christopher Hudson

School of Physics

University of Exeter

A thesis submitted for the degree of

Doctor of Philosophy in Physics

September 2014

Two dimensional atomically thin materials and hybrid superconducting devices

Submitted by David Christopher Hudson to the University of Exeter as
a thesis for the degree of Doctor of Philosophy in Physics.

September 2014

This thesis is available for library use on the understanding that it is copyright material
and that no quotation from the thesis may be published without proper acknowledge-
ment.

I certify that all material in this thesis which is not my own work has been identified
and that no material has previously submitted and approved for the award of a degree
by this or any other university.

David Christopher Hudson

September 2014

Abstract

In this thesis a variety of topics concerning 2D materials that have been separated from bulk layered crystals are discussed. Throughout the thesis, single and few layers of graphene, fluorinated graphene, MoS₂ and WS₂ are used. Two new methods of freely suspending 2D materials are presented as well as a method of removing the background from optical images. This aids contrast measurements for the determination of the number of layers.

Fluorinated graphene is found to be sensitive to beta radiation; the resistance of fluorinated graphene transistors is shown to decrease upon exposure to the radiation. This happens due to the carbon-fluorine bond breaking. The sp^3 hybridised structure of the fluorinated graphene is reduced back into the sp^2 hybridised structure of pristine graphene.

The superconducting properties of molybdenum-rhenium are characterised. It is shown to have a transition temperature of 7.5 K. It is also discovered that the material has a resistance to hydrofluoric acid; the acid etches nearly all other superconducting materials. This makes MoRe a possible candidate to explore superconductivity in conjunction with high mobility suspended graphene. To see if the material is compatible with graphene, a supported Josephson junction is fabricated. A proximity induced super current is sustained through the junction up to biases of ~ 200 nA.

The temperature dependence of the conductivity is measured for both suspended MoS₂ and WS₂ on a hexagonal boron nitride substrate. The dominant hopping mechanism that contributes to the conductivity at low temperatures is found to be Mott variable range hopping, with the characteristic $T^{-1/3}$ dependence. The hopping transport is due to impurities that are intrinsic to the crystals, this is confirmed by comparing the results with those of supported devices on SiO₂.

Acknowledgements

First I would like to say thanks to my supervisor Saverio Russo. It was clear from the beginning to see the passion and dedication he has for not only research, but also family. I would also like to thank Monica Craciun for useful discussions. I have learnt a great deal from both of them and I put that down to the working environment they created, which feels like a family. Everyone looking out for and helping each other, while also striving to do the best work possible each time. A big thank you to Russo and Craciun lab members past and present: Tymofiy Khodkov, Ivan Khrapach and Freddie Withers, who were already in the group when I joined and along with Saverio taught me everything I know about fabrication and measurement techniques. Steve Martins, Mohsin Aziz, Selim Unal, Mukond Khetani, Gareth Jones, Dominique Wehenkel, Matthew Barnes, Adolfo De-Sanctis it has been a pleasure working with you and even more so when not working! A special thanks to other PhD students, Sam Hornett, Claire Woollacott, Luke Coombes, Chris Downs, Charles Downing, Sneha Eashwer-Singhraj, Lachlan Marnham, Alex Pettitt, Damian Rumble, Hannah Wakeford and countless others for making my experience in Exeter a great one.

I would like to thank all my collaborators and highlight specific contributions to this thesis. Chris Downs for always being available to put his life in mortal danger and pour hydrofluoric acid over my devices. Marc Dubois for providing the technical knowledge and means of fluorinating graphite. Matthew Barnes for transferring CVD graphene and fabricating a device for chapter 4. Steve Martins for his initial measurements of the exfoliated fluorinated graphene devices. Freddie Withers for measurements on WS_2 and immensely improving my understanding of hopping conduction. Thomas Bointon for his help in Raman and AFM characterisation of devices.

I would also like to thank the technical, experimental officers and academic staff

at the University, without who this thesis would not be possible. Thank you to Adam Woodgate and David Gregory who supply liquid helium for measurements and are always available for a chat. To Paul Wilkins who has helped me cut many, many pieces of metal and wood for the most obscure purposes. His help has propped up my research both literally and figuratively and he is never too busy to help. I would like to thank David Anderson whose expert knowledge on electron beam lithography has been invaluable, he always has a solution and the time to help. To Mark Heath for keeping the cleanroom in perfect working order and providing assistance whenever possible. A special mention to David Horsell for his knowledge of cryogenic systems and guidance when cooling down a cryostat. To Alan Usher, my masters supervisor, whose project sparked my interest in condensed matter physics.

Finally a thanks to my closest friends and family for their constant support. My friends who have been with me since my undergraduate degree, many of whom I have lived with, Thomas Bointon, Alex Pearce, Thomas Haworth, Adam Snitch, Nikeel Patel. The shared experiences of our time in Exeter will stay with me forever. To my parents, Chris and Bridgit for their love and unwavering support; my brothers, Robbie and Sam; and to Sophie Worsfold, who has stuck by my side and provided constant motivation to help me finish my PhD.

All the best to everyone in the Russo-Craciun team and I hope to read many more papers from these wonderful people in the future.

List of publications

Electrical transport in suspended and double gated trilayer graphene. T. Khodkov, F. Withers, D. C. Hudson, M. F. Craciun and S. Russo, *Appl. Phys. Lett.* **100**, 013114 (2012)

Electron transport of WS₂ transistors in a hexagonal boron nitride dielectric environment. F. Withers, T. H. Bointon, D. C. Hudson, M. F. Craciun and S. Russo, *Scientific Reports* **4**, 4967 (2014)

Molybdenum-Rhenium superconducting suspended nanostructures. M. Aziz, D. C. Hudson, and S. Russo, *Appl. Phys. Lett.* **104**, 233102 (2014)

Beta radiation detection using fluorinated graphene. D. C. Hudson, M. D. Barns, S. E. Martins, M. Dubois, and S. Russo (in preparation)

List of Figures

- 2.1 The crystal lattice and Brillouin zone in graphene: **a)** The hexagonal lattice of a single graphene sheet is divided into two sub lattices with inequivalent atoms labelled A and B. The sub lattice vectors are labelled \mathbf{a}_1 and \mathbf{a}_2 , the nearest neighbour vectors $\boldsymbol{\delta}_1$, $\boldsymbol{\delta}_2$ and $\boldsymbol{\delta}_3$. The dashed diamond indicates the primitive unit cell of the lattice. **b)** The Brillouin zone scheme: high symmetry points are labelled such as the zone centre (Γ); the mid-point of a zone edge (\mathbf{M}); and corners of the Brillouin zone (\mathbf{K}) and (\mathbf{K}'). The Brillouin zone vectors are labelled \mathbf{b}_1 and \mathbf{b}_2 12
- 2.2 The band structure of monolayer graphene: **a)** The π and π^* bands as a function of k_x and k_y . The two bands meet at six points in the Brillouin zone where $E(\mathbf{k}) = 0$. A zoom around of one of these points is shown next to the main panel highlighting the linear dispersion. **b)** A trace of $E(\mathbf{k})$ along the high symmetry points $\Gamma - \mathbf{M} - \mathbf{K}$, notable is the asymmetry between the π and π^* bands due to the non-zero wave function overlap parameter s_0 18

- 2.3 Fluorinated graphene: **a)** A 3D representation of the crystal lattice (upper [8]) and isometric (lower). The grey atoms are carbon and the green atoms are fluorine. The sp^2 hybridization of graphene is modified by the attachment of the fluorine atoms and a 3D sp^3 structure is obtained. The angle between a carbon atom and two nearest neighbours is decreased to $\sim 110^\circ$ as the structure is transposed up and down on adjacent sites. **b)** The band structure of fully fluorinated graphene as calculated from first principles [7]. There is a band gap at the Γ -point of around 3.5 eV. 21
- 2.4 The trigonal prismatic structure of the TMDs: here atom a is a chalcogen and atom b is a transition metal. **a)** 3D view of the van der Waals stacked layers [14]. **b)** A side and top view of the hexagonal arrangement of the atoms [15]. **c)** The left panel shows the band structure of bulk MoS_2 ; there is an indirect transition at the Γ point. The band structure of monolayer MoS_2 is shown in the right panel; there is a direct transition at the K-point [16]. Note that the band structure of WS_2 , although not shown, has similar features to MoS_2 . The Hartree is the atomic unit of energy, where $1E_{\text{Hartree}} \sim 27.2$ eV. 23

- 2.5 Spin orbit splitting in TMDs: Spin split bands of monolayer **a)** MoS₂ and **b)** WS₂. The dashed red lines indicate the band structure calculated without the spin orbit interaction and the solid black lines with spin orbit interaction [17] There is a large splitting at the K-point in the valence band for both cases but the splitting size in WS₂ > MoS₂. The conduction band at the K-point becomes doubly degenerate. **c)** The allowed optical transitions from the valence bands of the K and K' valleys to the conduction band. Time reversal symmetry between the same bands in adjacent K-points leads to opposite spin split populations in each valley (indicated by the dashed and solid lines)[19]. 25
- 2.6 **a)** A depiction of the impurity bands that are introduced due to doping in a semiconductor. The transition from the lowest filled impurity band to the conduction band is labeled ϵ_{act} and the width of this band is ϵ_{nh} . **b)** The temperature dependence of the conductivity in a lightly doped semiconductor, plotted logarithmically as a function of T^{-1} . Region A corresponds to the intrinsic conductivity of the semiconductor at high temperatures. Regions B to D are due to the extrinsic conductivity governed by the specific nature of the impurities, as described in the main text. Modified from [21]. 26

- 2.7 **a)** An illustration of the density of states $g(\epsilon)$ in a highly disordered semiconductor. The continuous region of states within the forbidden region is known as the mobility gap. This separates the extended states of the conduction and valence bands from the localised states in the gap. **b)** A comparison of the nearest neighbour hopping (blue) and variable range hopping (red). At low temperatures it may require less energy for an electron to hop to a state at a further distance. **c)** A band of states with width $2\epsilon_0$ around the Fermi level in the centre of the mobility gap. These states will contribute to the variable range hopping. A constant density of states is assumed close to E_F 29
- 2.8 Types of Raman scattering: **a)** Elastic Rayleigh Scattering, a photon excites an electron into a virtual level which then decays and emits a photon of the same energy. **b)** Stokes and **c)** anti-Stokes, Inelastic, non-resonant scattering. After excitation with a photon to a virtual state the electron will emit (Stokes) or absorb (anti-Stokes) a phonon before decaying and emitting a photon of different energy. **d)** Stokes and **e)** anti-Stokes, inelastic resonant scattering. In these cases it is the same for **b)** and **c)** except that the incident photon has an energy that matches a transition to a real unoccupied electronic state. The resonant scattering processes produce more prominent peaks in the Raman spectra of the 2D materials. Adapted from [27]. 32

-
- 2.9 **a)** Phonon dispersion of monolayer graphene. Red circles identify the locations of the main Raman active phonon modes as described in the main text, adapted from [28]. **b)** Raman spectra of pristine graphene (top) and defected graphene (bottom). [27] **c)** Outlines of the different Raman scattering processes in monolayer graphene, adapted from [29] . 34
- 2.10 The single electron density of states and filled energy levels for **a)** a typical normal metal and **b)** a BCS superconductor. In the density of states for the superconductor at the Fermi level there is a delta function (labelled CP) representing the quasi-particle Cooper pair density of states. 39
- 2.11 Andreev reflection: **a)** An electron in a normal metal lead impinging upon the superconductor interface with energy $E_F + \epsilon$ where $\epsilon < \Delta$. **b)** The charge transfer process at the interface during Andreev reflection; a total charge of $2e$ is transferred to the superconductor. Electrons are shown as filled black circles and holes as outlined circles. 40
- 2.12 Andreev reflection in a SNS junction. Electrons are represented by filled black circles, holes by outlined circles. 42
- 2.13 Reflection processes between: **a)** A normal metal and an insulator; an electron is specularly reflected back into the normal metal. **b)** A normal metal and a superconductor or doped graphene and a superconductor; an electron undergoes Andreev reflection and a hole is retro-reflected. **c)** Undoped graphene and a superconductor; the Andreev reflection process is specular meaning the hole is specularly reflected. Adapted from [44]. 45

-
- 3.1 Standard electron beam lithography procedure for depositing metallic contacts: **a)** After spin coating PMMA resist, it is exposed to electron beam irradiation defining a pattern for metallic contacts. **b)** The exposed regions are removed by developing in MIBK for 20 seconds. **c)** The metals for the contacts are evaporated onto the substrate; a discontinuous film is achieved by the developed regions. **d)** The unwanted metal can be removed by dissolving the remaining PMMA in acetone. 53
- 3.2 Hydrofluoric acid etching process: **a)** A schematic showing the supported sample after metallic contact deposition but before the etching process. **b)** The device is placed in a buffered HF solution for 2.5 mins, which etches 200 nm; then it is subsequently transferred to DI water then IPA. **c)** A view of an etched sample, the oxide layer is 300 nm thick, so a thin layer still remains after etching; however there is an undercut beneath the gold contacts. **d)** The IPA is heated to 60°C and then transferred to a glass slide on a hot plate. This causes the IPA to evaporate with low surface tension. **e)** SEM image of a suspended graphene device. 56

- 3.3 Cross-linked PMMA suspension process: **a)** PMMA is spun onto a SiO₂ substrate and then few layer flakes are mechanically exfoliated onto the PMMA. A ramp from the PMMA surface down to the SiO₂ is constructed by a varying low dose of e-beam exposure. **b)** The PMMA is developed in MIBK leaving the ramps in tact. A large dose is then applied to the ramps to cause them to cross-link as shown in **c)**. **d)** A new layer of PMMA is spun on top to fill the gaps and allow the standard procedure of e-beam lithography to take place in step **e)**. **f)** For the final lift-off step in acetone all of the PMMA will be removed except for the cross-linked regions. Depending on how thick the layer of cross-linked PMMA is, it may be necessary to dry the sample on a hotplate as in Fig. 3.2. **g)** Dose versus height calibration for the PMMA ramps. **h)** AFM measurement of a PMMA ramp courtesy of Thomas Bointon. **i)** SEM image of a finished device showing two suspended regions. 58
- 3.4 HSQ suspension process: **a)** HSQ is spun onto SiO₂ and few layer flakes are then mechanically exfoliated onto HSQ. A layer of PMMA is then spun on top of this structure and the regions defining the contacts are exposed by standard e-beam doses. **b)** The exposure cross-links the HSQ, so after the PMMA is developed the HSQ remains untouched. Metallic contacts can be deposited. **c)** The metal is removed by lift-off in acetone but this does not affect the unexposed HSQ. **d)** To remove the unexposed HSQ and suspend the flakes the sample is washed in MF 319. It is then dried on a hot plate as in Fig. 3.2. **f)** SEM image of a finished device. 60

3.5	Device annealing methods: a) Heating in a furnace at 200°C under either a hydrogen/argon atmosphere (pictured) or vacuum. b) Electrical circuit for current annealing. c) Back gate dependence of resistance for a graphene flake before and after current annealing [7].	63
3.6	Representations of the sp^2 hybridised structure of graphene (left) and the sp^3 hybridised structure of fully fluorinated graphene (right).	64
3.7	a) An example of multiple graphene flakes of different thicknesses; ranked in order of increasing contrast. b) The measured average contrast of over 130 graphene flakes. There are clear plateaus distinguishing up to three layers. c) An example of a vignette that is subtracted from the optical images (the contrast has been modified to exaggerate the effect).	65
3.8	Raman spectra for graphene flakes of different layer numbers. The solid black lines are Lorentzian fits to the 2D-peak and the dashed black line is the final fit. Adapted from [17].	68
3.9	Raman characterisation of TMDs. a) Phonon dispersion for monolayer MoS ₂ (left) b) and WS ₂ (right), adapted from [22]. c) Raman spectrum of bulk WS ₂ , the peak at 350 cm ⁻¹ is fitted to two Lorentzians corresponding to the $E_{2g}^1(\Gamma)$ and 2LA(M) modes; the peak at 420 cm ⁻¹ corresponds to the $A_{1g}(\Gamma)$ mode [23]. d) The vibrational directions of the atoms for the $E_{2g}^1(\Gamma)$ mode (left), the 2LA(M) mode (centre) and the $A_{1g}(\Gamma)$ mode (right). e) Raman spectrum of WS ₂ for increasing number of layers [23]. f) Peak positions of the Raman active modes for increasing layer count [23]. All Raman spectra in this figure were taken with a laser wavelength of 532 nm with a spot size of 1.5 μm and 1 mW incident power.	70

- 3.10 **a)** Gate voltage dependence of the resistivity $R(V_g)$ for a monolayer graphene transistor device, adapted from [27]. **b)** Constant current circuit diagram for measuring $R(V_g)$. **c)** Gate voltage dependence of the source-drain current $I(V_g)$ for a monolayer MoS₂ device, adapted from [28]. **d)** Constant voltage circuit diagram for measuring $I(V_g)$ 73
- 4.1 Decay Process for ⁹⁰Sr. The initial decay process into ⁹⁰Y has a half-life of $\lambda = 28.5$ years and produces almost exclusively β radiation with an energy of 546 keV. These beta processes do not have enough energy to leave the radioactive source; the second decay process into ⁹⁰Zr produces much higher energy β particles ~ 2.3 MeV. These particles have a high enough energy to leave the source and reach the sample. 81
- 4.2 **a)** False colour SEM image of a typical device. Yellow represents the Cr/Au contacts, purple is the SiO₂ substrate and the green areas are FG. **b)** I_{SD} as a function of bias voltage V_{bias} for a FG flake unexposed to beta radiation. **c)** Schematic of the experimental setup, the ⁹⁰Sr beta source exposes the surface of the FG flake to β^- particles. **d)** The structure of fully fluorinated graphene, before (left) and after (right) exposure. The blue atoms represent carbon and the yellow atoms represent fluorine. 83
- 4.3 Calibration of the Strontium-90 source: **a)** The number of counts recorded on a Geiger counter as a function of distance in air. The counts decrease at an exponential rate with distance. **b)** The normalised profile of the emitted beam from the source, the maximum emission angle is $\sim 60^\circ$ 85
- 4.4 IV characteristics before (blue) and after (red) exposure to ⁹⁰Sr for: **a)** pristine graphene for 12 hours and **b)** FG for 30 minutes. **c)** The evolution of the IV curves for a FG device after exposure for 16 hours. 86

-
- 4.5 The estimated resistance of the sample plotted against the exposure time/dose. The shaded regions indicate regimes with different defluorination rates (yellow higher/blue lower). Inset: A log-log plot of the high dose regime. The dose required to fully defluorinate the graphene is extracted from the fit. 89
- 4.6 CVD grown fluorinated graphene with dimensions $L = 1 \text{ cm} \times W = 0.85 \text{ cm}$: **a)** Photograph of the device on a flexible transparent substrate. **b)** Resistance as a function of exposure time/dose. 91
- 5.1 **a)** A 100 nm sputter deposition of MoRe with a 5 nm Pd sticking layer; 300 W power and 3 mTorr gas pressure. The blue outline corresponds to a region where e-beam contacts have been defined. **b)** Close up of the MoRe leads after lift-off in acetone showing defects. Below the images are side on representations of the current stage in the lithography process. 97
- 5.2 Characterisation of a 200 nm wide channel of MoRe: **a)** The temperature dependence of the resistance measured upon cooling the device. The superconducting transition temperature $T_C = 5.67 \text{ K}$. The inset is an optical image of the channel after successful MoRe deposition. **b)** The VI characteristics of the channel at 250 mK, arrows indicate the direction of the sweeps. The critical current $I_C = 2.98 \text{ mA}$ and the re-trapping current $I_R = 0.16 \text{ mA}$ 99

- 5.3 Magnetic field dependence of the MoRe Channel: **a)** Downsweep and **b)** upswing colour plots of the voltage drop along the length of the channel as a function of source-drain current and magnetic field, $T = 250$ mK. **c)** and **d)** are the same data as above but plotted in a signed binary colour scheme where positive values are red, zero values are green and negative values are blue. In the green regions the resistance of the device is 0Ω . **e)** Left axis: The zero-bias resistance of the channel for increasing magnetic field. The critical field $B_C \sim 8$ T. Right axis: The extracted values of I_C from the upswing measurements. **f)** The computed values of the critical field as a function of temperature. 101
- 5.4 Temperature dependence of the resistance for a $250 \mu\text{m} \times 250 \mu\text{m}$ MoRe square with thickness 120 nm. The transition temperature where the resistance drops to 0Ω is ~ 7.5 K. 102
- 5.5 **a)** A false colour SEM image of a MoRe channel after HF etching. **b)** Voltage-current characteristics for the etched MoRe channel. 103
- 5.6 Characterisation of a Ti/MoRe (5 nm/120 nm) Josephson junction with graphene weak link of channel length 200 nm: **a)** An optical image of the device with multiple channel lengths (100, 150 & 200 nm). **b)** The gate voltage dependence of the resistance of the at ~ 270 mK. The graphene is electron doped to only a few volts. **c)** The VI characteristics at a gate voltage of 0 V (blue curve) and 50 V (red curve) at $T = 30$ mK. **d)** The differential resistance as a function of the source drain current. The dashed lines are a guide to match the features with the VI curve. . . 105

- 5.7 **a)** Temperature dependence of the differential resistance in the bias range $\pm 50 \mu\text{A}$. T increases from 280 mK (blue) to 13 K (red). Features of interest are labeled with Roman numerals; the inset is a zoom showing the evolution of the low bias peak that appears for low T . **b)** The differential resistance as a function of bias voltage for $T = 280 \text{ mK}$, labelled are the BCS predicted values of the superconducting gap Δ for MoRe. All plots in this figure were taken at $V_g = 0$ 107
- 6.1 The dry transfer process for flakes: **a)** The substrate is prepared by first spinning a water soluble polymer (aquasave) on SiO_2 and then a layer of PMMA. WS_2 flakes are exfoliated onto the PMMA. **b)** A membrane is constructed using tape with a small square hole cut in the centre. The substrate is attached to the tape. **c)** The sample is exposed to water and the aquasave dissolves leaving the PMMA and flakes freely suspended over the hole in the tape. **d)** A second substrate is prepared with boron nitride flakes. The flakes on the membrane can be aligned over the boron nitride using an optical microscope and a height adjustable stage. The substrate is heated to melt the PMMA and complete the transfer process. 115
- 6.2 **a)** IV characteristics of a device before and after annealing. **b)** The circuit setup for annealing, a large $1 \text{ G}\Omega$ resistor is placed in series to the device to prevent damage to the flake if the resistance drops sharply. 116
- 6.3 Field effect transfer characteristics for **a)** single layer MoS_2 on SiO_2 , **b)** 4-layer MoS_2 on SiO_2 and **c)** 4-layer MoS_2 on h-BN. The device in **c)** has the largest mobility with $\mu = 80 \text{ cm}^{-2}\text{V}^{-1}\text{s}^{-1}$. The mobilities are calculated using the method described in chapter 3.4.2. 117

- 6.4 **a)** The temperature dependence of $\sigma(V_g)$ for 4-layer WS₂ on h-BN. The temperature range is from 200 K down to 4.2 K over a narrow gate voltage range. **b)** The temperature dependence of $\sigma(V_g)$ for 4-layer WS₂ on SiO₂. An expanded gate voltage range is shown. 118
- 6.5 Thermally activated transport data: **a)** An Arrhenius plot of the conductivity as a function of T^{-1} for $V_g = 60.5$ V. The fit is consistent with thermally activated transport. The units of S/1S represent a ‘dimensionless conductance’ for purposes of taking a logarithm. **b)** The extracted activation energy for different gate voltages (each point is an average over an 0.2 V range). 120
- 6.6 **a)** The $\sigma(T)$ dependence at $V_g = 60.5$ V plotted as a function of T^{-p} , where p takes the value of 1 for NNH, 1/2 for Efros-Shklovskii VRH, 1/3 for Mott VRH in 2D. The best fit was determined to be $p = 1/3$. **b)** The red curve is a plot of $\sigma(V_g)$ at $T = 4.2$ K; the overlaid blue data points are extracted values of the hopping parameter T_0 121
- 6.7 **a)** 4-layer WS₂ on h-BN. Top panel: A stability diagram of the differential conductance as a function of source drain voltage and gate voltage at $T = 4.2$ K. Bottom panel: $\sigma(V_g)$ at $T = 4.2$ K. Inset: Conductance traces as a function of source drain voltage, from the regions labeled A (61.5 V) up to B (62 V) on the main panel. **b)** 4-layer WS₂ on SiO₂, differential conductance as a function of source drain voltage and gate voltage at $T = 4.2$ K 123

-
- 6.8 Suspended MoS₂: **a)** A false colour SEM image of a suspended MoS₂ flake: purple is the etched SiO₂; yellow is the Au contacts; and green is the flake. **b)** An overview of the field effect transfer characteristic for a range of temperatures. The device is biased at $V_{SD} = 500$ mV. **c)** Mobility values extracted from the $I(V_g)$ curves at different temperatures. **d)** A closer look at the low temperature $I(V_g)$ curves. There appears to be repeatable features up to 20 K, two of which are identified by the dashed lines. 125
- 6.9 Hopping data: **a)** The conductivity data for different gate voltages plotted in terms of thermally activated transport (T^{-1}). Dashed lines are a guide for the eyes to see where the data deviates from the fit. **b)** Conductivity data for different gate voltages plotted in terms of Mott VRH ($T^{-1/3}$). 126

Contents

1	Introduction	1
1.1	Emergence of 2D single layered materials	1
1.2	This thesis	4
2	Theoretical concepts	11
2.1	Crystal structure of graphene	11
2.1.1	Tight binding model for monolayer graphene	13
2.1.2	Massless Dirac fermions	19
2.2	Fluorinated graphene	20
2.3	Transition metal dichalcogenides	21
2.4	Conduction mechanisms in disordered systems	24
2.4.1	Temperature dependence of the conductivity in a lightly doped semiconductor	24
2.4.2	Mott variable range hopping	27
2.5	Raman spectroscopy	31
2.5.1	Raman scattering	31
2.5.2	Raman spectrum of graphene	33
2.6	Superconductivity	35
2.6.1	Cooper pairs and the BCS ground state	36

2.6.2	Andreev reflection	40
3	Device fabrication and measurement techniques	51
3.1	Device fabrication procedures	51
3.1.1	Mechanical exfoliation and fabricating a simple transistor structure	51
3.1.2	Methods of suspending atomically thin materials	54
3.1.3	Improved performance through annealing	61
3.2	Synthesis of fluorinated graphene	62
3.3	Characterisation of 2D materials	64
3.3.1	Optical contrast of graphene	64
3.3.2	Determining the number of graphene layers using Raman spectroscopy	67
3.4	Electrical characterisation	71
3.4.1	Graphene and constant current measurements	71
3.4.2	TMDs and constant voltage measurements	72
3.5	Summary	74
4	Atomically thin and flexible beta radiation detectors based on fluorinated graphene	79
4.1	Introduction	79
4.2	Methods	80
4.2.1	Fabrication	80
4.2.2	Radioactive source calibration	82
4.3	Results	84
4.4	Discussion and conclusions	87
4.4.1	CVD fluorinated graphene device	88

4.5	Conclusions	91
5	Towards suspended MoRe Josephson junctions with a graphene weak link	95
5.1	Introduction	96
5.2	Deposition of superconducting metals	96
5.3	Characterisation of MoRe	98
5.3.1	Thin channels	98
5.3.2	Bulk material	102
5.4	Resistance to hydrofluoric acid	102
5.5	MoRe Josephson junctions with a graphene weak link	104
5.6	Conclusions	108
6	The nature of electronic transport in WS₂ and MoS₂	113
6.1	Introduction	114
6.2	WS ₂	114
6.2.1	Methods	114
6.2.2	Results	118
6.2.3	Discussion	119
6.3	MoS ₂	124
6.4	Conclusions	127
7	Conclusions and proposals for future work	131

Chapter 1

Introduction

1.1 Emergence of 2D single layered materials

The experimental realisation of graphene in 2004 [1] could prove to be one of the most technologically important discoveries of the 21st century. It is being touted as *the* material of the future, with applications as diverse and rich as the fundamental physics exhibited by this simple one atom thick sheet of carbon atoms [2]. The electronic structure of graphene has been studied since the 1940s when Wallace described the band theory of graphite, starting from a single layer of graphene [3]; later expanded on by Slonczewski, Weiss and McClure [4, 5]. Experimentally however it was not isolated until 2004 because it had previously been thought that a 2D material could not exist in a free state, due to a lack of long range ordering in a 2D crystal [6]. Attempts to produce graphene also suffered because of its high optical transparency making it ‘invisible’ on certain substrates. By selecting a suitably thick oxide layer on silicon and using a monochromatic wavelength of light, graphene can be easily seen under a microscope [7].

Graphene exhibits a wealth of exotic physics that arises from its linear band struc-

ture and the chiral nature of the quasi-particles that exist at low energy excitations. These charge carriers behave like massless Dirac-fermions [8]. Although graphene exhibits exceptional mobility [9] and flexible strength [10], the potential to be used as a transistor in the next generation of transparent and flexible electronics is limited by the lack of a band gap. This is required for fast switching, low power transistors with a high on/off ratio. A band gap has been demonstrated in bi-layer [11] and tri-layer [12] graphene under dual gated conditions. However in the case of bi-layer graphene this band gap is small, on the order of 250 meV. There have been a number of attempts to engineer a band gap in monolayer graphene, one such route is chemical functionalization. Since each carbon atom has 4 valence electrons and only 3 contribute to the in-plane σ bonding there is a ‘spare’ electron ready to form covalent bonds. Functionalization with hydrogen and fluorine removes the out of plane π -bonding which is so crucial to the high conductivity of graphene. As a result a wide band gap semiconductor is formed with band gaps theorised to be around 3 – 5 eV [13]. Another way to chemically modify graphene is by the intercalation of molecules that sit between the graphene sheets; only weakly bonded to the graphene via the Van der Waals interaction. Graphite intercalation compounds have been well studied [14] and so there is the potential to modify the properties of graphene for applications beyond pristine graphene. For example, graphene intercalated with FeCl_3 is hole doped and displays a lower resistance per square, and similar transparency to the leading commercial transparent conductor, indium-tin oxide [15].

But perhaps more important than the discovery of graphene itself, is the field of research it has established in two dimensional atomically thin materials. The simple micro-mechanical cleavage technique used to exfoliate graphene from graphite spurred research onto other layered crystals such as hexagonal boron-nitride (h-BN) and the

transition metal dichalcogenides (TMDs), such as molybdenum-disulphide (MoS_2) and tungsten-disulphide (WS_2). These crystals exhibit interesting physics in their own right, such as spin and valley coupling in MoS_2 and WS_2 [16]. But it is the possibility to combine and layer these crystals on top of each other that is of interest for future applications [17]. It is therefore important to understand the underlying transport mechanisms and fundamental limits of these materials.

The possibility of using graphene in conjunction with superconducting metals opens up more avenues for research. An important property of Josephson junctions is the phase coherence length of the charge carriers in the normal metal region. This is maximised in the case that the weak link of the system is a ballistic conductor. In clean graphene the ballistic transport regime is accessible [18, 19] where the mean free path is estimated to be $\approx 3 \mu\text{m}$. This could enhance certain phenomena in superconducting devices such as in a Cooper pair splitting junction [20, 21], where the physics of entangled fermions can be explored. The limiting factors of such devices, where the tunnelling medium is an InAs nanowire, is related to having a low charge carrier density and the fact that the mean free path is smaller than the coherence length. This leads to a low transmission probability for the Cooper pairs and the system is restricted to the diffusive limit; using high mobility graphene could resolve these issues. Another example is the Josephson quantum electron pump. Such a device exploits the time dependent superconducting phases of the two arms in a superconducting quantum interference device [22]. In these devices a current can flow across an unbiased normal metal conductor that links the two arms due to adiabatic quantum pumping. So far only signatures of this pumped current have been observed in devices using InAs as the normal metal conductor. It has also been predicted that a pumped spin current can be observed in zig-zag edges of graphene nano ribbons [23].

1.2 This thesis

In **chapter 2**, the band structure of graphene will be calculated showing how the hexagonal lattice leads to massless Dirac fermions. The properties of fluorinated graphene and transition metal dichalcogenides will also be discussed. The theory of hopping conduction in these materials will be presented in terms of the lightly doped semiconductor model, the conditions for nearest neighbour hopping and Mott variable range hopping will be described. Finally the formation of Cooper pairs that are responsible for superconductivity will be discussed as well as the charge conversion processes that happen at normal-superconducting interfaces.

In **chapter 3**, the standard fabrication procedure for obtaining the 2D crystals is outlined, as well as two new ways of freely suspending the thin sheets. The optical and electrical characterisation procedures are outlined, including optical contrast, Raman spectroscopy and electrical measurement techniques to determine the charge carrier mobility.

In **chapter 4**, graphene functionalized by fluorine is subjected to beta radiation. This has the effect of breaking the carbon-fluorine bonds, lowering the resistance of the devices. In addition to mechanically exfoliated flakes, a prototype device made from CVD grown graphene is transferred onto a flexible substrate. The devices are irradiated for several hours to determine their sensitivity for use in real world applications, such as personal dosimeters or to be embedded within food packaging.

In **chapter 5**, a relatively unknown superconducting material MoRe is investigated. The initial challenges in achieving a uniform film are shown before the superconducting properties of the material are characterised at low temperatures. The material is then used to create a Josephson junction with graphene as a weak link.

In **chapter 6**, the low temperature conductivities of WS₂ and MoS₂ are investigated

on hexagonal boron nitride and in freely suspended structures respectively. In this way the dominant hopping mechanisms that contribute to the transport at these low temperatures can be explored in a nearly defect free environment.

Bibliography

- [1] K. S. Novoselov, A. K. Geim, S. V. Morozov, D. Jiang, Y. Zhang, S. V. Dubonos, I. V. Grigorieva, and A. A. Firsov, *Science* **306**, 666 (2004).
- [2] K. S. Novoselov, V. I. Fal'ko, L. Colombo, P. R. Gellert, M. G. Schwab, and K. Kim, *Nature* **490**, 192 (2012).
- [3] P. R. Wallace, *Phys. Rev.* **71**, 622 (1947).
- [4] J. W. McClure, *Phys. Rev.* **108**, 612 (1957).
- [5] J. C. Slonczewski and P. R. Weiss, *Phys. Rev.* **109**, 272 (1958).
- [6] N. D. Mermin, *Phys. Rev.* **176**, 250 (1968).
- [7] P. Blake, E. W. Hill, A. H. Castro Neto, K. S. Novoselov, D. Jiang, R. Yang, T. J. Booth, and A. K. Geim, *Applied Physics Letters* **91**, (2007).
- [8] K. S. Novoselov, A. K. Geim, S. V. Morozov, D. Jiang, M. I. Katsnelson, I. V. Grigorieva, S. V. Dubonos, and A. A. Firsov, *Nature* **438**, 197 (2005).
- [9] K. Bolotin, K. Sikes, Z. Jiang, M. Klima, G. Fudenberg, J. Hone, P. Kim, and H. Stormer, *Solid State Communications* **146**, 351 (2008).
- [10] C. Lee, X. Wei, J. W. Kysar, and J. Hone, *Science* **321**, 385 (2008).

-
- [11] Y. Zhang, T.-T. Tang, C. Girit, Z. Hao, M. C. Martin, A. Zettl, M. F. Crommie, Y. R. Shen, and F. Wang, *Nature* **459**, 820 (2009).
- [12] M. F. Craciun, S. Russo, M. Yamamoto, J. B. Oostinga, A. F. Morpurgo, and S. Tarucha, *Nat Nano* **4**, 383 (2009).
- [13] O. Leenaerts, H. Peelaers, A. D. Hernández-Nieves, B. Partoens, and F. M. Peeters, *Phys. Rev. B* **82**, 195436 (2010).
- [14] L. B. Ebert, *Annual Review of Materials Science* **6**, 181 (1976).
- [15] I. Khrapach, F. Withers, T. H. Bointon, D. K. Polyushkin, W. L. Barnes, S. Russo, and M. F. Craciun, *Advanced Materials* **24**, 2844 (2012).
- [16] D. Xiao, G.-B. Liu, W. Feng, X. Xu, and W. Yao, *Phys. Rev. Lett.* **108**, 196802 (2012).
- [17] A. K. Geim and I. V. Grigorieva, *Nature* **499**, 419 (2013).
- [18] A. S. Mayorov, R. V. Gorbachev, S. V. Morozov, L. Britnell, R. Jalil, L. A. Ponomarenko, P. Blake, K. S. Novoselov, K. Watanabe, T. Taniguchi, et al., *Nano Letters* **11**, 2396 (2011).
- [19] J. Baringhaus, M. Ruan, F. Edler, A. Tejada, M. Sicot, Taleb-IbrahimiAmina, A.-P. Li, Z. Jiang, E. H. Conrad, C. Berger, et al., *Nature* **506**, 349 (2014).
- [20] P. Cadden-Zimansky, J. Wei, and V. Chandrasekhar, *Nat Phys* **5**, 393 (2009).
- [21] L. Hofstetter, S. Csonka, J. Nygard, and C. Schonenberger, *Nature* **461**, 960 (2009).

- [22] F. Giazotto, P. Spathis, S. Roddaro, S. Biswas, F. Taddei, M. Governale, and L. Sorba, *Nat Phys* **7**, 857 (2011).
- [23] S. Souma and M. Ogawa, *Applied Physics Letters* **104**, (2014).

Chapter 2

Theoretical concepts

2.1 Crystal structure of graphene

The remarkable electronic properties of graphene can be explained by looking at its band structure. This section will introduce the basic concepts of the tight binding model in graphene, leading to Dirac electrons. A single sheet of graphene is a hexagonal arrangement of sp^2 hybridised carbon atoms. The $2s$, $2p_x$ and $2p_y$ orbitals contribute to three sp^2 orbitals and form in-plane σ -bonds with neighbouring carbon atoms. Each σ -bond is occupied by 2 electrons of opposite spin and the remaining carbon electron occupies the $2p_z$ orbital, which is out of plane and forms π -bonds with neighbouring $2p_z$ orbitals. The band structure associated with the π -bonding can be calculated with the tight binding method discussed in the next section.

The honeycomb structure can be divided into two sub lattices with inequivalent atoms, labelled A and B in Fig. 2.1 (a). Each sub lattice has a basis of 2, with the lattice vectors:

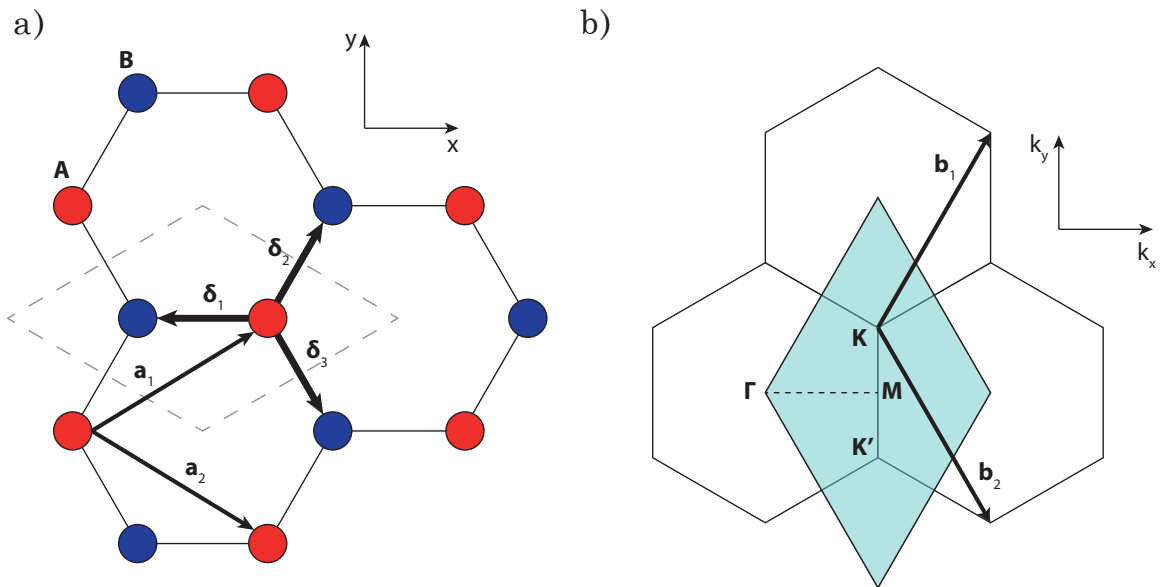


Figure 2.1: The crystal lattice and Brillouin zone in graphene: **a)** The hexagonal lattice of a single graphene sheet is divided into two sub lattices with inequivalent atoms labelled A and B. The sub lattice vectors are labelled \mathbf{a}_1 and \mathbf{a}_2 , the nearest neighbour vectors δ_1 , δ_2 and δ_3 . The dashed diamond indicates the primitive unit cell of the lattice. **b)** The Brillouin zone scheme: high symmetry points are labelled such as the zone centre (Γ); the mid-point of a zone edge (\mathbf{M}); and corners of the Brillouin zone (\mathbf{K}) and (\mathbf{K}'). The Brillouin zone vectors are labelled \mathbf{b}_1 and \mathbf{b}_2 .

$$\mathbf{a}_1 = \frac{a}{2} (3, \sqrt{3}), \quad \mathbf{a}_2 = \frac{a}{2} (3, -\sqrt{3}), \quad (2.1)$$

where a is the distance between neighbouring carbon atoms ($a \approx 1.42 \text{ \AA}$) [1]. The reciprocal lattice vectors are given by:

$$\mathbf{b}_1 = \frac{2\pi}{3a} (1, \sqrt{3}), \quad \mathbf{b}_2 = \frac{2\pi}{3a} (1, -\sqrt{3}), \quad (2.2)$$

and are highlighted in the Brillouin zone scheme in Fig. 2.1 (b). For the tight binding calculation in the next section, the nearest neighbour approximation is taken so the vectors of the nearest neighbour atoms are also needed:

$$\boldsymbol{\delta}_1 = a(-1, 0), \quad \boldsymbol{\delta}_2 = \frac{a}{2}(1, \sqrt{3}), \quad \boldsymbol{\delta}_3 = \frac{a}{2}(1, -\sqrt{3}). \quad (2.3)$$

2.1.1 Tight binding model for monolayer graphene

The derivation in this section follows the methods in [2] and [3]. The tight binding model considers the wave functions of electrons that are tightly bound to an atom in the lattice. This requires that the electron has little interaction with neighbouring electrons, therefore the isolated electron wave functions should be similar to the electronic orbital of an individual atom. The periodic nature of the lattice allows the system to be described as a Wannier function (which satisfies the Bloch condition):

$$\psi_j = \frac{1}{\sqrt{N}} \sum_{i=1}^N e^{i\mathbf{k} \cdot \mathbf{R}_{i,j}} \phi(\mathbf{r} - \mathbf{R}_{i,j}), \quad (2.4)$$

where ($i = 1, \dots, N$) counts over the number of unit cells in the crystal. There are j orbitals per unit cell, so for the case of graphene where there are two atoms, ($j = A, B$). The position of the atom in the i th unit cell at orbital site j is given by $\mathbf{R}_{i,j}$. The

wave function of the $2p_z$ orbital for carbon is represented by $\phi(\mathbf{r} - \mathbf{R}_{i,j})$. The total wave function describing the system is a sum of the Bloch functions ψ_j describing the electrons on sites A and B:

$$|\psi\rangle = c_A |\psi_A\rangle + c_B |\psi_B\rangle. \quad (2.5)$$

This form of the wave function can be input to the Schrödinger equation:

$$H |\psi\rangle = E_{\mathbf{k}} |\psi\rangle \quad (2.6)$$

$$c_A H |\psi_A\rangle + c_B H |\psi_B\rangle = E_{\mathbf{k}} (c_A |\psi_A\rangle + c_B |\psi_B\rangle). \quad (2.7)$$

Now multiplying through with the bras $\langle\psi_A|$ and $\langle\psi_B|$ will yield a system of linear equations:

$$c_A \langle\psi_A| H |\psi_A\rangle + c_B \langle\psi_A| H |\psi_B\rangle = E_{\mathbf{k}} (c_A \langle\psi_A|\psi_A\rangle + c_B \langle\psi_A|\psi_B\rangle) \quad (2.8)$$

$$c_A \langle\psi_B| H |\psi_A\rangle + c_B \langle\psi_B| H |\psi_B\rangle = E_{\mathbf{k}} (c_A \langle\psi_B|\psi_A\rangle + c_B \langle\psi_B|\psi_B\rangle), \quad (2.9)$$

where $\langle\psi_i| H |\psi_j\rangle$ represents the matrix element of the Hamiltonian H_{ij} and $\langle\psi_i|\psi_j\rangle$ represents the overlap matrix element S_{ij} . It is therefore convenient to represent these equations in matrix form:

$$\begin{pmatrix} H_{AA} & H_{AB} \\ H_{BA} & H_{BB} \end{pmatrix} \begin{pmatrix} c_A \\ c_B \end{pmatrix} = E_{\mathbf{k}} \begin{pmatrix} S_{AA} & S_{AB} \\ S_{BA} & S_{BB} \end{pmatrix} \begin{pmatrix} c_A \\ c_B \end{pmatrix}. \quad (2.10)$$

This is now an equation in the form of $H |\psi\rangle = E_{\mathbf{k}} S |\psi\rangle$, which can be rearranged to obtain:

$$(H - E_{\mathbf{k}}S) \{ c_j \} = 0. \quad (2.11)$$

The coefficients c_j must have a non-zero value to define the wave function, so to find the eigenvalues $E_{\mathbf{k}}$, the secular equation needs to be solved:

$$|H - E_{\mathbf{k}}S| = 0. \quad (2.12)$$

There will be two solutions since there are two lattice sites in the unit cell. The problem can be simplified for monolayer graphene when you consider that the on-site energies of the A and B atoms are equal, therefore $H_{AA} = H_{BB}$. For the off-diagonal elements $H_{AB} = H_{BA}^*$. The initial assumption for the tight binding model was that the wave functions of the isolated atoms do not interact with their neighbours so the off-diagonal overlap integrals $\langle \psi_A | \psi_B \rangle = \langle \psi_B | \psi_A \rangle^*$ should vanish. In practice however there is a small overlap, the value of which can be calculated by density functional theory (DFT). Since the original Bloch functions are normalised the diagonal overlap integrals $\langle \psi_A | \psi_A \rangle = \langle \psi_B | \psi_B \rangle = 1$. The statements above will now be used to find the matrix elements for both S and H .

Diagonal matrix elements

The on site energy for the lattice site A can be found by substituting Eqn. 2.4 into $\langle \psi_A | H | \psi_A \rangle$:

$$H_{AA} = \frac{1}{N} \sum_{i=1}^N \sum_{j=1}^N e^{i\mathbf{k} \cdot (\mathbf{R}_{A,j} - \mathbf{R}_{A,i})} \langle \phi_A(\mathbf{r} - \mathbf{R}_{A,j}) | H | \phi_A(\mathbf{r} - \mathbf{R}_{A,i}) \rangle. \quad (2.13)$$

Assuming that the dominant contribution occurs from the lattice site of the unit

cell under consideration ($i = j$) and not from sites further away, the exponential in Eqn. 2.13 becomes unity and the matrix element $\langle \phi_A | H | \phi_A \rangle$ is simply the energy of the $2p_z$ orbital, ϵ_{2p} .

$$H_{AA} \approx \frac{1}{N} \sum_{i=1}^N \epsilon_{2p} = \epsilon_{2p}. \quad (2.14)$$

A similar reasoning for the lattice site B shows that $H_{BB} = H_{AA} = \epsilon_{2p}$. The matrix overlap coefficient S_{AA} can be calculated in a similar way and using the property $\langle \psi_A | \psi_A \rangle = 1$ gives:

$$S_{AA} = \frac{1}{N} \sum_{i=1}^N \langle \phi_A(\mathbf{R}_{A,j} - \mathbf{R}_{A,i}) | \phi_A(\mathbf{R}_{A,j} - \mathbf{R}_{A,i}) \rangle = 1. \quad (2.15)$$

Off-diagonal matrix elements

$$H_{AB} = \frac{1}{N} \sum_{i=1}^N \sum_{j=1}^N e^{i\mathbf{k} \cdot (\mathbf{R}_{B,j} - \mathbf{R}_{A,i})} \langle \phi_A(\mathbf{r} - \mathbf{R}_{A,j}) | H | \phi_B(\mathbf{r} - \mathbf{R}_{B,i}) \rangle. \quad (2.16)$$

The off-diagonal matrix element H_{AB} describes the energy of the hopping process from the A to B sub-lattices. The dominant contribution can be found by considering only the first set of nearest neighbours for each lattice site ($i = 1, \dots, N$ & $j = l = 1, 2, 3$). The matrix element $\langle \phi_A | H | \phi_B \rangle$ (hopping parameter), has the same value for each nearest neighbour and so it can be set to a constant, $\gamma_0 = -t = -\langle \phi_A(\mathbf{r} - \mathbf{R}_{A,l}) | H | \phi_B(\mathbf{r} - \mathbf{R}_{B,i}) \rangle$.

$$H_{AB} = -\frac{\gamma_0}{N} \sum_{i=1}^N \sum_{l=1}^3 e^{i\mathbf{k} \cdot (\mathbf{R}_{B,l} - \mathbf{R}_{A,i})}. \quad (2.17)$$

The quantity in the exponential, $\mathbf{R}_{B,l} - \mathbf{R}_{A,i}$ is simply the vector of the nearest neighbour l from lattice site A as defined in Eqn. 2.3. The matrix element then simplifies to:

$$H_{AB} = -\frac{\gamma_0}{N} \sum_{i=1}^N \sum_{l=1}^3 e^{i\mathbf{k}\cdot\delta_l} = -\gamma_0 f(\mathbf{k}). \quad (2.18)$$

The value of $f(\mathbf{k})$ will be evaluated later. The other off-diagonal element H_{BA} is the complex conjugate of H_{AB} . The overlap integral for S_{AB} and S_{BA} can be found by using the same process:

$$S_{AB} = s_0 f(\mathbf{k}), \quad S_{BA} = s_0 f^*(\mathbf{k}), \quad (2.19)$$

where the overlap parameter $s_0 = \langle \phi_A(\mathbf{r} - \mathbf{R}_{A,i}) | \phi_B(\mathbf{r} - \mathbf{R}_{B,l}) \rangle$. The matrix elements for S and H now become:

$$H = \begin{pmatrix} \epsilon_{2p} & -\gamma_0 f(\mathbf{k}) \\ -\gamma_0 f^*(\mathbf{k}) & \epsilon_{2p} \end{pmatrix}, \quad S = \begin{pmatrix} 1 & s_0 f(\mathbf{k}) \\ s_0 f(\mathbf{k}) & 1 \end{pmatrix}.$$

The secular equation (2.12) can now be solved:

$$\begin{vmatrix} \epsilon_{2p} - E_{\mathbf{k}} & -(\gamma_0 + E s_0) f(\mathbf{k}) \\ -(\gamma_0 + E s_0) f^*(\mathbf{k}) & \epsilon_{2p} - E_{\mathbf{k}} \end{vmatrix} = 0 \quad (2.20)$$

$$E_{\mathbf{k}} = \frac{\epsilon_{2p} \pm \gamma_0 |f(\mathbf{k})|}{1 \mp s_0 |f(\mathbf{k})|}. \quad (2.21)$$

Here the $+$ root in the numerator corresponds to the π (conduction) band and the $-$ root the π^* (valence) band. The parameters $\gamma_0 = 3.033$ eV and $s_0 = 0.129$, as calculated by DFT [2]. To simplify further ϵ_{2p} is set to zero as the origin for the energy scale. The function $f(\mathbf{k})$ is the last requirement to generate the band structure:

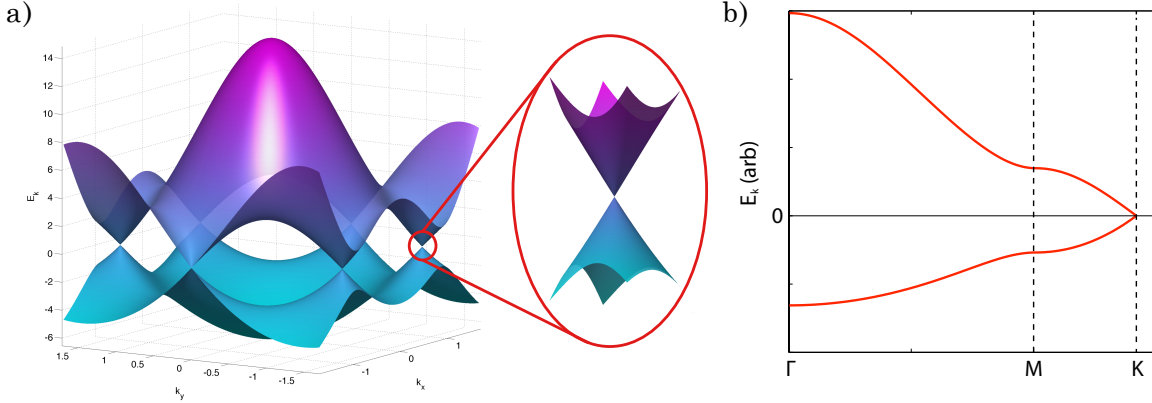


Figure 2.2: The band structure of monolayer graphene: **a)** The π and π^* bands as a function of k_x and k_y . The two bands meet at six points in the Brillouin zone where $E(\mathbf{k}) = 0$. A zoom around of one of these points is shown next to the main panel highlighting the linear dispersion. **b)** A trace of $E(\mathbf{k})$ along the high symmetry points $\Gamma - \mathbf{M} - \mathbf{K}$, notable is the asymmetry between the π and π^* bands due to the non-zero wave function overlap parameter s_0 .

$$f(\mathbf{k}) = \sum_{l=1}^3 e^{i\mathbf{k}\cdot\delta_l} \quad (2.22)$$

$$= e^{-ik_x a} + e^{ik_x a/2} e^{ik_y \sqrt{3}a/2} + e^{ik_x a/2} e^{-ik_y \sqrt{3}a/2} \quad (2.23)$$

$$|f(\mathbf{k})| = \sqrt{1 + 4 \cos(k_y \sqrt{3}a/2) \cos(k_x 3a/2) + 4 \cos^2(k_y \sqrt{3}a/2)}. \quad (2.24)$$

The final band structure for monolayer graphene as calculated using Eqn. 2.21 is shown in Fig. 2.2 (a). The Fermi level lies at zero energy for un-doped monolayer graphene; at this energy the conduction and valence bands meet in the six corners of the Brillouin zone (\mathbf{K} -points). There is no band gap in monolayer graphene and in the vicinity of the \mathbf{K} -points the energy dispersion is linear, Fig. 2.2 (a, zoom). The electrons in the vicinity of the \mathbf{K} -points can be described by a Dirac-like Hamiltonian

which will be described in the next section, hence the \mathbf{K} -points are also known as Dirac points. Finally there is an asymmetry between the conduction and valence bands which is attributed to the finite value of the overlap parameter s_0 , it is easier to see this asymmetry in the $E(\mathbf{k})$ trace along the points $\Gamma - \mathbf{M} - \mathbf{K}$ in Fig. 2.2 (c).

2.1.2 Massless Dirac fermions

Two important points within the Brillouin zone are the inequivalent points, \mathbf{K} and \mathbf{K}' . There are six corners in total but choosing the two inequivalent points to be located at

$$\mathbf{K}_{\pm} = \pm \left(0, \frac{4\pi}{3\sqrt{3}a} \right), \quad (2.25)$$

simplifies the following equations and the remaining \mathbf{K} -points can be reached via the reciprocal lattice vectors. By expanding the Hamiltonian around the two Dirac points, an expression for the linear energy dispersion close to \mathbf{K} can be obtained. Let $\mathbf{k} = \mathbf{K}_{\pm} + \Delta\mathbf{k}$ and the Hamiltonian becomes [4]:

$$H = \frac{3a\gamma_0}{2} \begin{pmatrix} 0 & -i\Delta k_x \mp \Delta k_y \\ i\Delta k_x \pm \Delta k_y & 0 \end{pmatrix} \quad (2.26)$$

Using this form of the Hamiltonian to solve the secular equation gives the energy eigenvalues [4]:

$$E_k = \pm \frac{3a\gamma_0}{2} |\mathbf{k}| = \pm v_F |\mathbf{k}| \quad (2.27)$$

Where $v_F \approx 10^6 \text{ ms}^{-1}$ is the Fermi velocity for graphene [1]. The dispersion relation is therefore linear around the \mathbf{K} -points, creating conical bands, Fig. 2.2 (a, zoom). The effective mass of the charge carriers is zero close to \mathbf{K} .

2.2 Fluorinated graphene

The extra electron from each carbon atom that forms the sp_z orbital in pristine graphene makes each carbon site readily able to form covalent bonds. Hydrogen and fluorine, both having a vacant position in their electronic valence shell, are ideal candidates to functionalize graphene with. Graphite intercalation compounds have been well studied [5, 6], but only recently due to the discovery of graphene has there been an interest in the single layered versions of these materials. Consider the case of fully fluorinated graphene where each carbon atom is covalently bonded to a fluorine atom. The sp^2 hybridised structure of the graphene is modified as the carbon atoms become sp^3 hybridised; a 3D structure is formed, Fig. 2.3 (a). All of the electrons are now localised in σ -bonds and the π -bands disappear. This results in the opening of a large band gap which is calculated to be around 3.5 eV [7]. Fig. 2.3 (b) shows the band structure of fully fluorinated graphene.

The percentage of the fluorine coverage can be controlled by the growth process, which will be discussed in the next chapter, but the fluorine content has a dramatic impact on the conduction processes. Partial fluorination coverage does not lead to a clean band gap, the random dispersion of fluorine adatoms acts as a source of disorder within the crystal. Impurity states are introduced into the forbidden gap which leads to variable range hopping (VRH) at low temperatures. The type of VRH can also be tuned by the fluorine coverage, for monolayers with a ratio of $CF_{0.24}$ displaying non-interacting Mott VRH in 2D and $CF_{0.28}$ displaying Efros-Shklovskii VRH [8]. Methods of hopping conduction will be discussed in Sec. 2.4. It has been shown recently that the C-F bond can be broken by electron beam irradiation [9], this reduces the 3D sp^3 structure back to the 2D sp^2 structure, pristine graphene is recovered. This property will be exploited in chapter 4 to create beta radiation detectors out of fluorinated

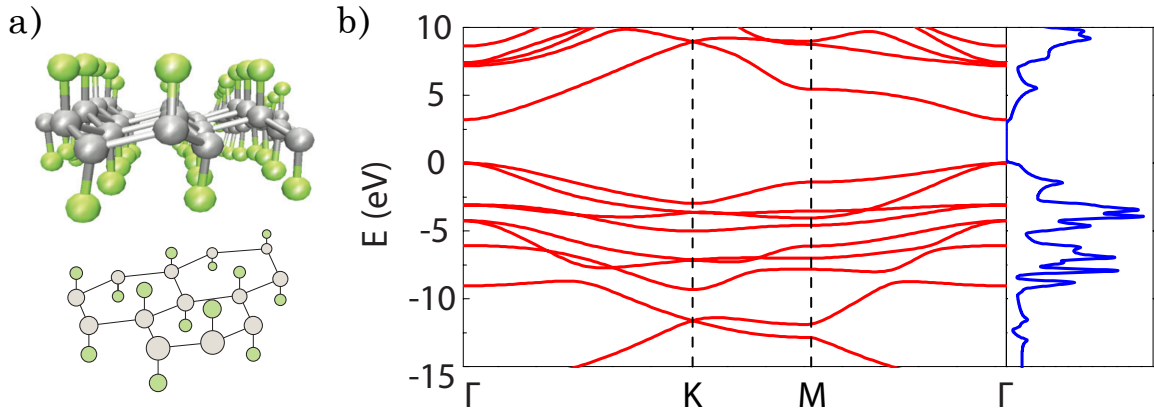


Figure 2.3: Fluorinated graphene: **a)** A 3D representation of the crystal lattice (upper [8]) and isometric (lower). The grey atoms are carbon and the green atoms are fluorine. The sp^2 hybridization of graphene is modified by the attachment of the fluorine atoms and a 3D sp^3 structure is obtained. The angle between a carbon atom and two nearest neighbours is decreased to $\sim 110^\circ$ as the structure is transposed up and down on adjacent sites. **b)** The band structure of fully fluorinated graphene as calculated from first principles [7]. There is a band gap at the Γ -point of around 3.5 eV.

graphene.

2.3 Transition metal dichalcogenides

The transition metal dichalcogenides (TMDs) are a class of van der Waals bonded, vertically layered materials. Their original use as a dry lubricant is due to the weak coupling between the layers allowing them to slide apart easily. They mostly share a common lattice structure as shown in Fig. 2.4 (a). A layer of transition metal atoms is sandwiched between two layers of chalcogen atoms (S, Se or Te). They can be arranged in either a trigonal prismatic or octahedral structure [10]. This thesis focuses on the group 6 elements, molybdenum and tungsten; in a trigonal prismatic arrangement with sulphur as the chalcogen (MoS_2 and WS_2). Both materials display

the similar properties with almost identical band structures, Fig. 2.4 (b) and (c) show the electronic dispersion for bulk and monolayer MoS₂ respectively. The bulk material is an indirect-gap semiconductor with a transition originating at the Γ -point. The size of the gap is 1.2 eV in MoS₂ [11] and 1.3 eV [12] in WS₂. As the number of layers decreases towards monolayer, the valence band energy at the K-point shifts upwards and the conduction band near the Γ -point also shifts upwards. The resultant effect is that in monolayer MoS₂ and WS₂, there is now a direct transition at the K-point with a gap of 1.9 eV [11] and 2 eV [12] respectively. The electronic states near the Γ -point are due to the anti-bonding p_z orbitals on the S atoms and the d orbitals on the Mo/W atoms [13]. The p_z states have a strong interlayer coupling, so reducing the number of layers has a pronounced effect on the band structure near Γ . The states near the K-point are mainly due to the localised d orbitals on the Mo/W atoms and as such are not as affected by the number of layers [13].

Monolayer MoS₂ and WS₂ have a number of properties which come together to create a coupling between the spin and valley indices of the electron/hole populations. There is a lack of inversion symmetry in the monolayer case, whereby on one sub lattice there is a single atom (Mo/W) and on the other sub lattice there are two sulphur atoms. This combined with the large spin orbit interaction of the heavy transition metal atoms, leads to a splitting of the valence band at the K-point (≈ 148 meV in MoS₂ and ≈ 426 meV in WS₂) [17], Fig. 2.5 (a, b). The conduction band remains doubly degenerate at the K-point, although it has also been calculated that there could be small splitting [18]. There is also a time reversal symmetry between the carriers of opposite spin in different valleys [$E_{\uparrow}(\mathbf{k}) = E_{\downarrow}(-\mathbf{k})$], which couples the spin and valley of the valence bands [19]. The spin-valley coupling is unique to these two dimensional materials and may lead to a new class of ‘spin+valleytronic’ devices; it has already been shown that carriers can

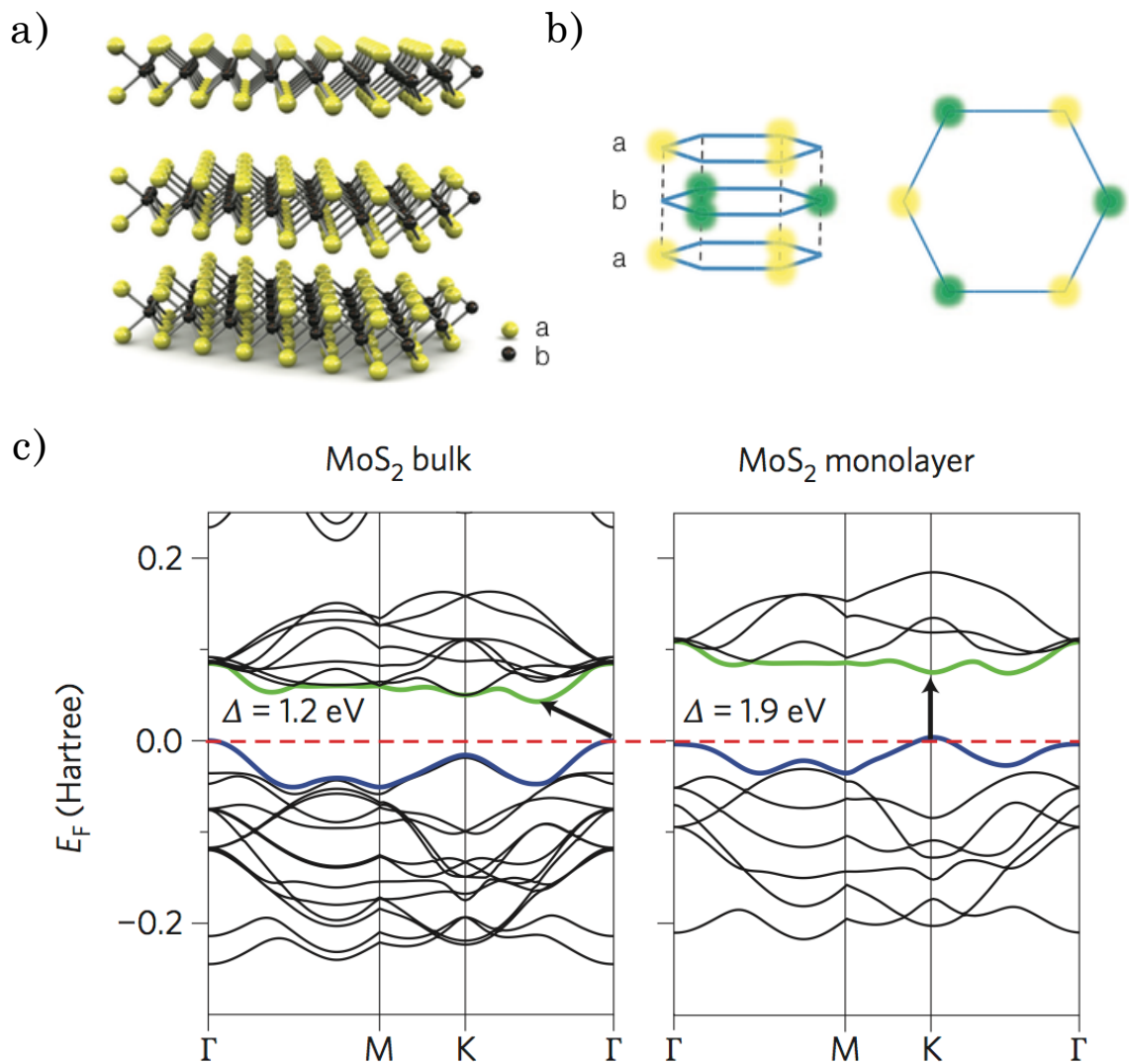


Figure 2.4: The trigonal prismatic structure of the TMDs: here atom a is a chalcogen and atom b is a transition metal. **a)** 3D view of the van der Waals stacked layers [14]. **b)** A side and top view of the hexagonal arrangement of the atoms [15]. **c)** The left panel shows the band structure of bulk MoS₂; there is an indirect transition at the Γ -point. The band structure of monolayer MoS₂ is shown in the right panel; there is a direct transition at the K-point [16]. Note that the band structure of WS₂, although not shown, has similar features to MoS₂. The Hartree is the atomic unit of energy, where $1E_{\text{Hartree}} \sim 27.2$ eV.

be excited from a specific valley, chosen by the direction of circularly polarised light [20]. A schematic of the spin-split band structure and allowed transitions is shown in Fig. 2.5 (c). It is theorised that it may be possible to create devices that exploit spin and valley Hall effects [17] as well as there being evidence for quasiparticle trion states in MoS₂ [15]. Understanding the limitations of the mobility in MoS₂ and WS₂ will hopefully lead to the realisation of devices which take advantage of these interesting properties.

2.4 Conduction mechanisms in disordered systems

As we have seen in the previous sections both fluorinated graphene and MoS₂/WS₂ are semiconducting materials. In chapter 6 the low temperature transport of MoS₂ and WS₂ is investigated, so in this section the transport mechanisms that contribute to the conduction are introduced. While this thesis does not investigate the low temperature transport of fluorinated graphene it is worth noting that the conduction mechanisms below also apply for certain fluorination coverages [8].

2.4.1 Temperature dependence of the conductivity in a lightly doped semiconductor

In an intrinsic semiconductor the band gap is clean and at high temperatures electrons from the valence band can be easily thermally activated to the conduction band. The number of carriers is related to the temperature of the system by [21]:

$$n = p = \frac{(2\pi\sqrt{m_e m_h} k_B T)^{3/2}}{2\pi\hbar^3} \exp(-E_g/k_B T), \quad (2.28)$$

where n and p are the carrier concentrations of electrons and holes and m_e and m_h

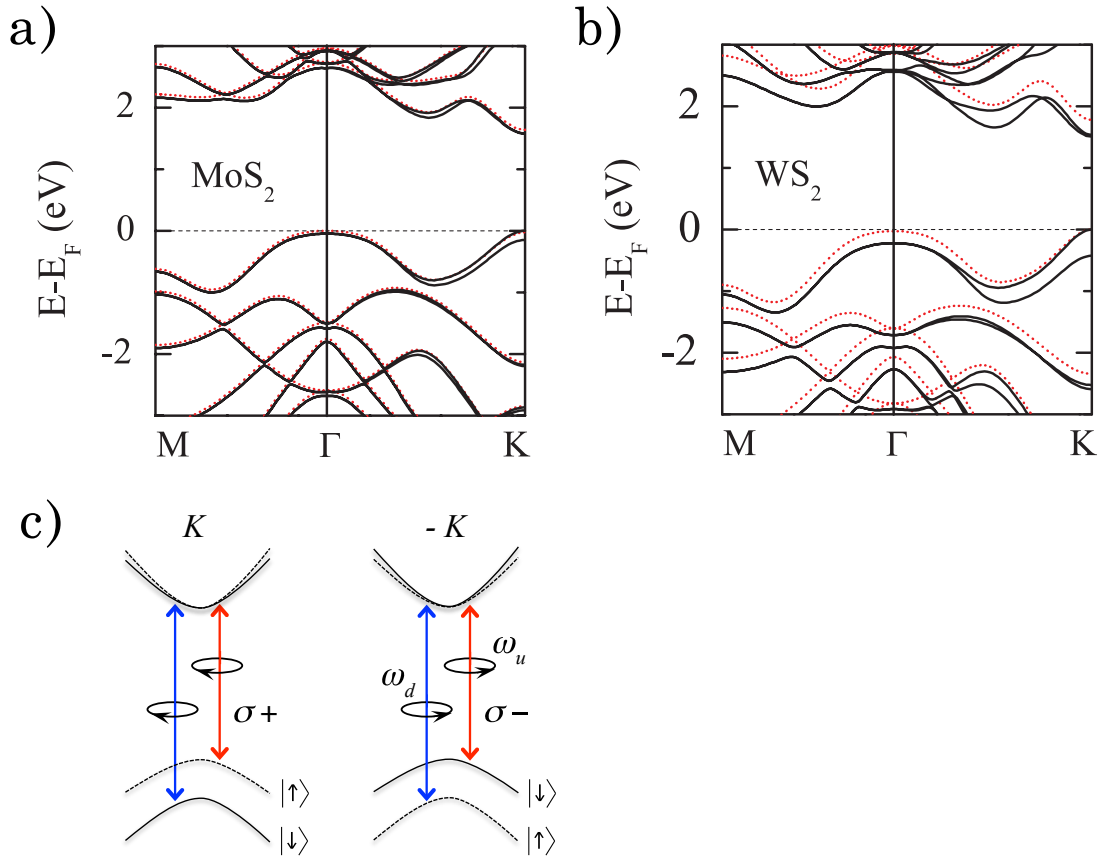


Figure 2.5: Spin orbit splitting in TMDs: Spin split bands of monolayer **a)** MoS₂ and **b)** WS₂. The dashed red lines indicate the band structure calculated without the spin orbit interaction and the solid black lines with spin orbit interaction [17]. There is a large splitting at the K-point in the valence band for both cases but the splitting size in WS₂ > MoS₂. The conduction band at the K-point becomes doubly degenerate. **c)** The allowed optical transitions from the valence bands of the K and K' valleys to the conduction band. Time reversal symmetry between the same bands in adjacent K-points leads to opposite spin split populations in each valley (indicated by the dashed and solid lines)[19].

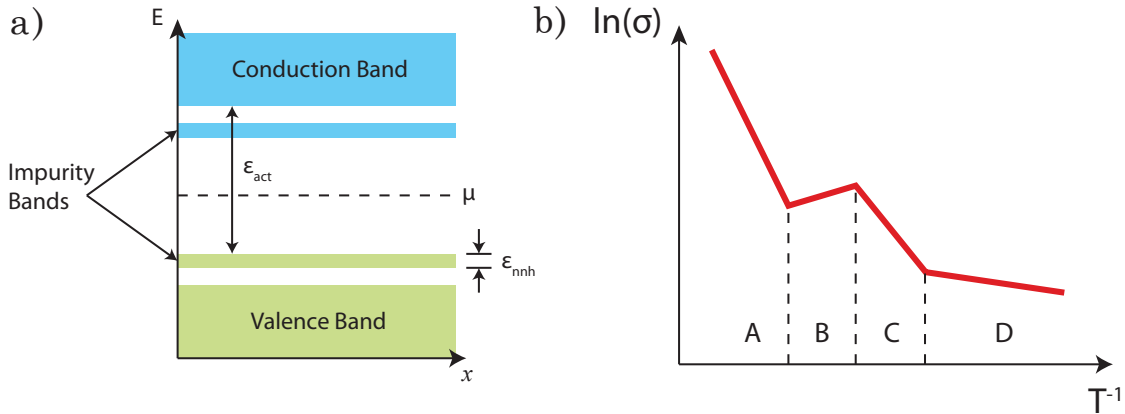


Figure 2.6: a) A depiction of the impurity bands that are introduced due to doping in a semiconductor. The transition from the lowest filled impurity band to the conduction band is labeled ϵ_{act} and the width of this band is ϵ_{nnh} . b) The temperature dependence of the conductivity in a lightly doped semiconductor, plotted logarithmically as a function of T^{-1} . Region A corresponds to the intrinsic conductivity of the semiconductor at high temperatures. Regions B to D are due to the extrinsic conductivity governed by the specific nature of the impurities, as described in the main text. Modified from [21].

are their effective masses respectively. If the size of the band gap E_g is large, then the exponential term will dominate at low temperatures and the concentration of carriers decreases rapidly. By introducing a small amount of doping to the semiconductor, a band of impurity states are introduced, which will have a profound effect on the temperature dependence of the semiconductor. A schematic overview of the band structure of such a system is shown in Fig. 2.6 (a).

Within the intrinsic band gap of the semiconductor there now exists a ‘band’ of impurity states of width ϵ_{nnh} . This is not a continuous band, in the sense that the wave functions of the electronic states do not spread out throughout the entirety of the crystal, instead the states are localised with a small overlap between neighbouring sites. The temperature dependence of a lightly doped semiconductor is shown in Fig.

2.6 (b), the high temperature region A corresponds to the conductivity due to the intrinsic carriers of the semiconductor and decreases rapidly with temperature.

Due to the smaller energy required to thermally activate a carrier from the impurity band than from the valence band when the temperature is low enough there may come a point where the number of carriers contributed by the impurity band exceeds the intrinsic carrier concentration. The conductivity of the system can actually increase in this regime (region B), attributed to a weakening of electron-phonon scattering. Upon reduction of the temperature further, the impurities freeze out the carriers, therefore the decreased conductivity in region C is attributed to a decrease in the number of free carriers. When the temperature decreases even further, hopping conduction occurring directly between free states in the impurity band is observed (region D). Hopping to a nearest neighbour requires an activation energy ϵ_{nnh} on the order of the width of the impurity band. The temperature dependence of the conductivity of such a system can be approximated by [21]:

$$\sigma(T) = \sigma_{\text{act}} \exp(\epsilon_{\text{act}}/k_B T) + \sigma_{\text{nnh}} \exp(\epsilon_{\text{nnh}}/k_B T). \quad (2.29)$$

The first term describes the thermally activated transport and the second term describes nearest neighbour hopping where $\epsilon_{\text{nnh}} < \epsilon_{\text{act}}$. The first term dominates at high T and the second term at low T . In the next section, Mott variable range hopping (VRH) for a system of non-interacting electrons is discussed, which has a different characteristic temperature dependence.

2.4.2 Mott variable range hopping

VRH was first introduced by Mott [22, 23, 24], it describes the low temperature hopping conductivity of carriers within a disordered crystal such as an amorphous semiconduc-

tor. In this case the intrinsic band gap is not fully developed; rather than having a narrow band of impurity states there will exist a continuous density of localised states. This introduces tails to the conduction and valence bands Fig. 2.7 (a). If the Fermi level lies within this band of localised states, known as the mobility gap, then at zero temperature the conductivity will vanish and at finite temperatures VRH will occur. The crux of the idea is that at sufficiently low temperatures, it may be more energetically favourable for a carrier to hop to a state of similar energy that is far away, than a neighbouring state which requires a large activation, Fig. 2.7 (b).

Consider a narrow band of states around the Fermi level with width $2\epsilon_0$, Fig. 2.7 (c). The energy of a particular state ϵ_i that contributes to the conduction must be within this band i.e. $|\epsilon_i - E_F| \leq \epsilon_0$. It will be shown that the width of this band is temperature dependent. Since the band is narrow there is a large separation between the states and at low temperature, the density of states near the Fermi level is constant [21]. The concentration of states is given by:

$$N(\epsilon_0) = 2g(E_F)\epsilon_0. \quad (2.30)$$

The probability of a hopping process occurring over a distance R is given by [22]:

$$p(R) \approx \exp \left[-\frac{2R}{\xi} - \frac{\epsilon_0}{k_B T} \right], \quad (2.31)$$

here ξ is the localisation radius of the electron. There is competition between the left term in the exponential, which describes tunnelling to a state at distance R and the right term which describes the thermal activation of a carrier. In three-dimensions the average distance R between the localised states is given by $R = \left(\frac{3}{4\pi} \frac{1}{N(\epsilon_0)} \right)^{1/3}$. The maximum probability for an electron to hop to a state at a distance R , can be found by differentiating p with respect to the band width ϵ_0 and finding the maximum:

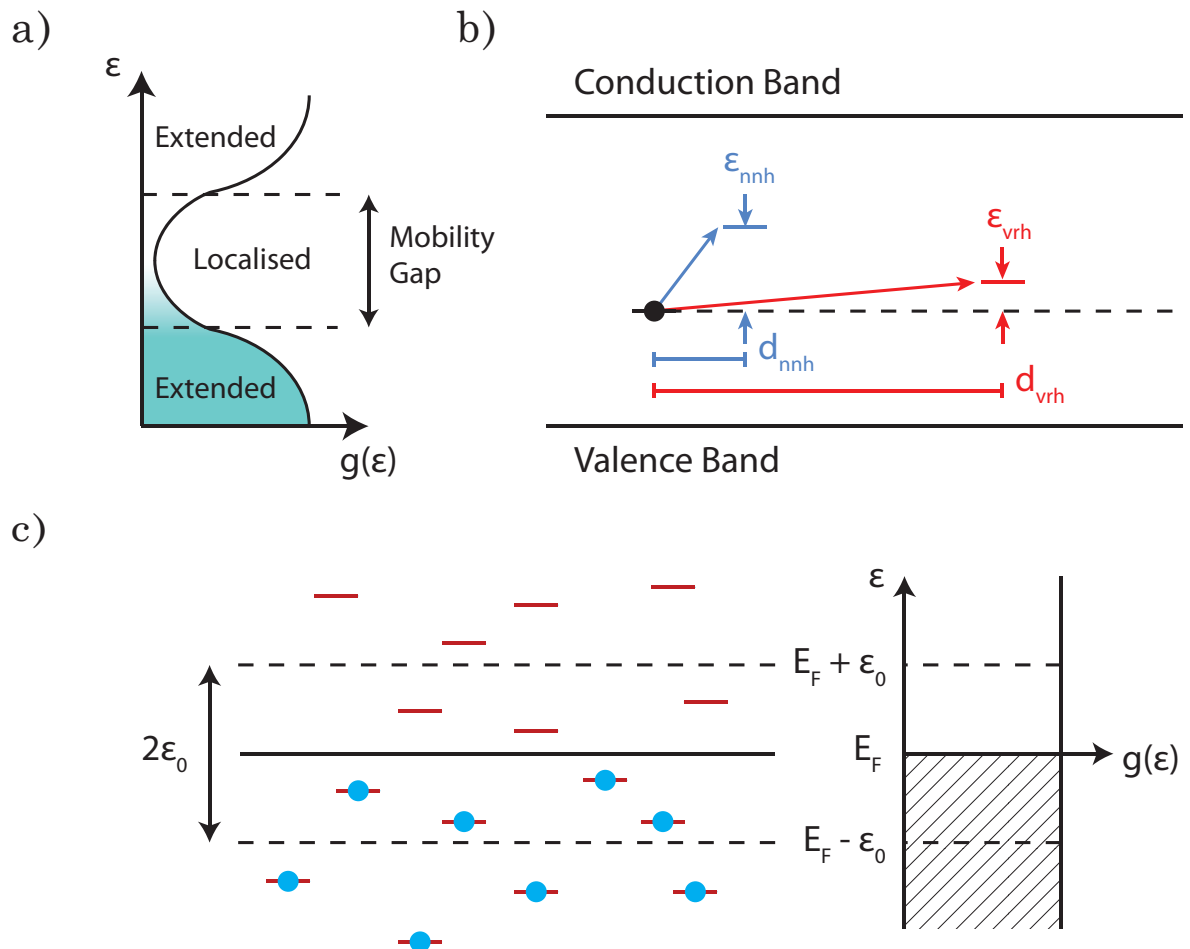


Figure 2.7: **a)** An illustration of the density of states $g(\epsilon)$ in a highly disordered semiconductor. The continuous region of states within the forbidden region is known as the mobility gap. This separates the extended states of the conduction and valence bands from the localised states in the gap. **b)** A comparison of the nearest neighbour hopping (blue) and variable range hopping (red). At low temperatures it may require less energy for an electron to hop to a state at a further distance. **c)** A band of states with width $2\epsilon_0$ around the Fermi level in the centre of the mobility gap. These states will contribute to the variable range hopping. A constant density of states is assumed close to E_F .

$$\frac{\partial p(R)}{\partial \epsilon_0} = 0 \quad \Rightarrow \quad \epsilon_0 = \epsilon_0(T) = \frac{\alpha(kT)^{3/4}}{(g(E_F)\xi^3)^{1/4}}, \quad (2.32)$$

where α is a constant and $\epsilon_0(T)$ is shown to be temperature dependent, it is known as the optimal band of states that contribute to the variable range hopping. By substituting this back into the Eqn. 2.31 the expression for Mott's VRH is obtained:

$$p(T) \approx \sigma(T) = \sigma_0 \exp \left[\left(-\frac{T_0}{T} \right)^{1/4} \right], \quad (2.33)$$

where $T_0 = \frac{\beta}{g(E_F)k_B\xi^3}$ and β is a dimensionless constant whose value can be obtained from the percolation description of the Mott VRH [21]. A more general description of VRH can be obtained for a system of d dimensions, then the expression in Eqn. 2.33 becomes [21]:

$$\sigma(T) = \sigma_0 \exp \left[\left(-\frac{T_0}{T} \right)^{1/(d+1)} \right]. \quad (2.34)$$

In this thesis the two dimensional form is considered and the constant β has a value of 13.8 for $d = 2$ [21]. The above description of the VRH only considers a system of independent electrons. The conductivity temperature dependence for a system of interacting electrons is modified by the presence of the Coulomb interaction. The derivation will not be discussed as it is not needed to explain the transport in WS₂ or MoS₂ but the result will be stated below so that this method of conduction can be ruled out when discussing the transport data in chapter 6.

$$\sigma(T) = \sigma_0 \exp \left[\left(-\frac{T_0}{T} \right)^{1/2} \right]. \quad (2.35)$$

This is known as Efros-Shklovskii VRH, it has the same temperature dependence

($T^{-1/2}$) regardless of the dimensionality of the system [25, 26].

2.5 Raman spectroscopy

When dealing with 2D materials it is important to know the number of layers, the properties of the system can dramatically change with increasing layers. For example, monolayer MoS₂ is a direct gap semiconductor, which due to lack of inversion symmetry and a large spin orbit interaction has a coupling between the spin and valley quantum numbers. By adding just one layer this inversion symmetry is reinstated and the system no longer has spin-valley coupling; additionally the band gap transition becomes indirect. Having a reliable method to identify the layer count is therefore extremely important. There are a variety of different techniques that could be employed; atomic force microscopy is accurate but slow; optical contrast measurements are good for a quick estimate, but are affected by dirt and height variations on the substrate; Raman spectroscopy offers a quick, non-destructive, high resolution probe of both the electronic and structural information of the system. This section will introduce the concept of Raman scattering and the mechanisms that play a role in graphene.

2.5.1 Raman scattering

To start with a basic explanation of Raman scattering, consider the electron energy levels in Fig. 2.8. A photon of energy $\hbar\omega_L$ is absorbed by an electron in a material and the electron is promoted to an excited state; creating an electron-hole pair. The nature of this state depends on the energy of the incident photon and the availability of a stationary state for the electron to transition into. The most common scenario is when there are no unoccupied electronic states matching the energy level of the

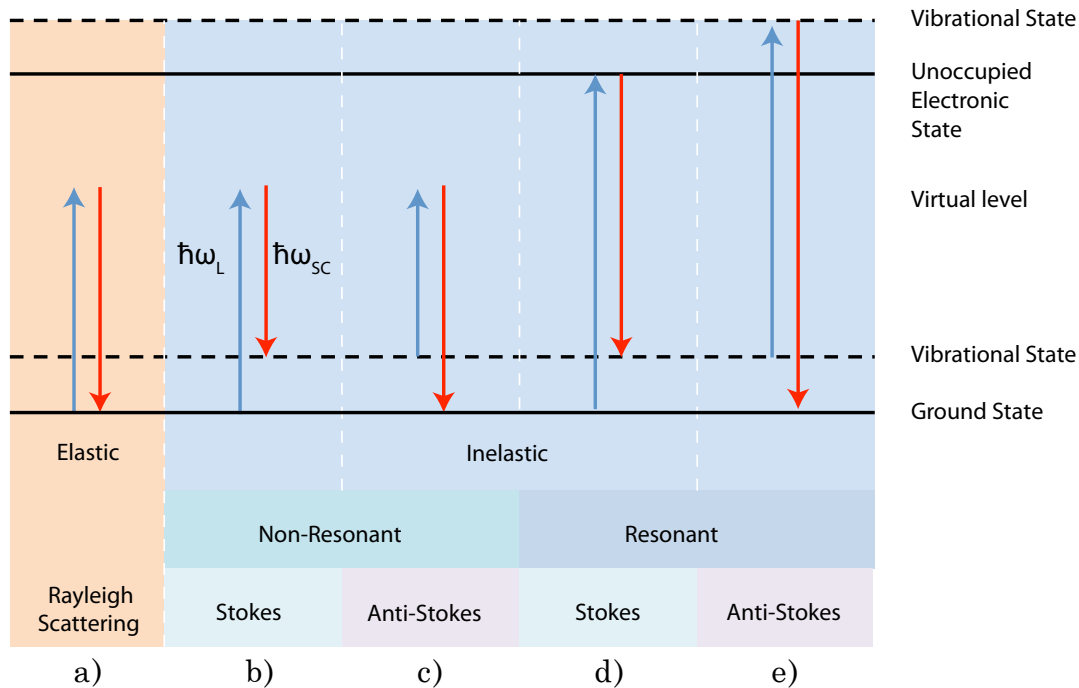


Figure 2.8: Types of Raman scattering: **a)** Elastic Rayleigh Scattering, a photon excites an electron into a virtual level which then decays and emits a photon of the same energy. **b)** Stokes and **c)** anti-Stokes, Inelastic, non-resonant scattering. After excitation with a photon to a virtual state the electron will emit (Stokes) or absorb (anti-Stokes) a phonon before decaying and emitting a photon of different energy. **d)** Stokes and **e)** anti-Stokes, inelastic resonant scattering. In these cases it is the same for **b)** and **c)** except that the incident photon has an energy that matches a transition to a real unoccupied electronic state. The resonant scattering processes produce more prominent peaks in the Raman spectra of the 2D materials. Adapted from [27].

incoming photon. In this case the electron resides in a short lived virtual state (a, b, c in Fig. 2.8). If the electron simply recombines with the hole without interaction with the lattice then the energy of the emitted photon will be the same as the incident photon. This is known as Rayleigh scattering, an elastic process shown in (a). If however the electron then interacts with a phonon, either by emission (Stokes, b), or absorption (Anti-Stokes, c), then the energy of the scattered electron is changed and becomes $\hbar\omega_{SC}$. Upon recombining with the hole, a photon with a different wavelength is emitted. Raman scattering is essentially the inelastic scattering of photons by phonons. A special case, resonant scattering occurs when the energy of the incident photon matches the transition energy to an unoccupied electronic state (d, e). In graphene due to the linear band dispersion, excitation of any ω_L will result in resonant scattering [27]. The difference in energy between the absorbed and emitted photons is known as the Raman shift, often expressed as the change in wavelength of the photons with units of cm^{-1} .

2.5.2 Raman spectrum of graphene

Since the Raman shift is a measure of the phonon energies of the system, it is useful to look at the phonon dispersion in graphene to determine the origin of the Raman processes. The unit cell of monolayer graphene contains two inequivalent atoms, corresponding to six branches in the phonon dispersion [28] as shown in Fig. 2.9 (a). There are three optical (O) and three acoustic (A) branches, the directions of the phonon modes are determined with respect to the nearest carbon-carbon atoms. For one O mode and one A mode, the atomic vibrations are out of plane (Z) also known as flexural modes. The remaining O and A branches are in-plane oscillations with transverse (T) and longitudinal (L) directions. The in-plane transverse and longitudinal optical modes

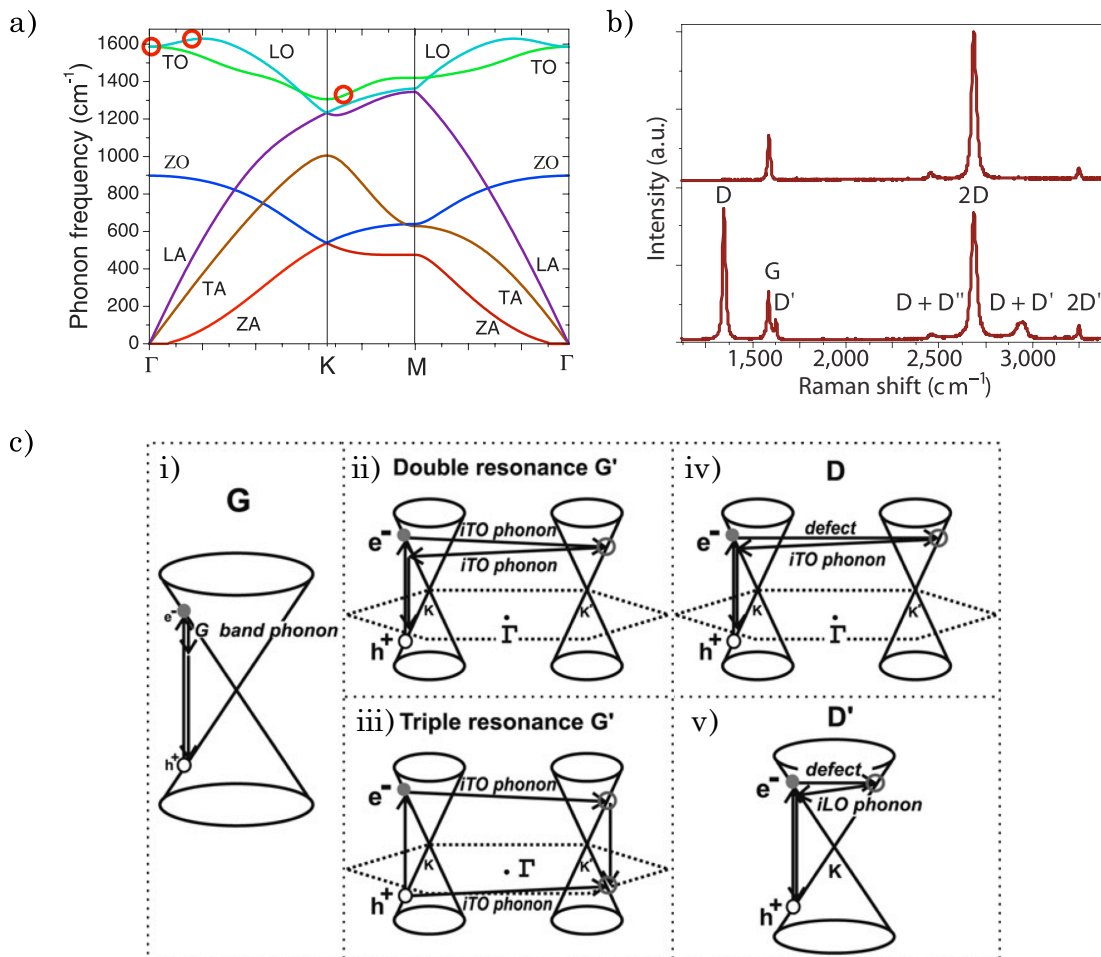


Figure 2.9: a) Phonon dispersion of monolayer graphene. Red circles identify the locations of the main Raman active phonon modes as described in the main text, adapted from [28]. b) Raman spectra of pristine graphene (top) and defected graphene (bottom). [27] c) Outlines of the different Raman scattering processes in monolayer graphene, adapted from [29]

are Raman active and become degenerate around the Γ -point. Marked on Fig. 2.9 (a) are the positions of the phonons which contribute to the main spectral features in the Raman spectrum of graphene, these will be discussed in more detail below. The top plot of Fig. 2.9 (b) displays the Raman spectrum of pristine (i.e. defect free graphene), the G-band is located at $\sim 1580 \text{ cm}^{-1}$ [30] and is from the doubly degenerate LO and TO modes at the Γ -point. The G-band is a first order scattering process as depicted in Fig. 2.9 (c, i), the excited electron emits a phonon, losing energy and recombining with a hole in the same valley. The 2D-band (also known as G') at $\sim 2700 \text{ cm}^{-1}$ [30] is associated with the TO phonons close to the Brillouin zone centre; the scattering processes can either be doubly resonant or triply resonant, Fig. 2.9 (c, ii, iii).

The lower panel in Fig. 2.9 (b) displays defected graphene, the defects can act as elastic scatterers allowing Raman processes which would be forbidden by the fundamental Raman selection rule. The D-band is seen at $\sim 1350 \text{ cm}^{-1}$ [30] and involves inter-valley scattering off of the defect before scattering with a phonon, Fig. 2.9 (c, iv). It arises from TO phonons near the K-point of the Brillouin zone. The D'-band and the 2D'-band are overtones of the D and 2D bands respectively, they are both intra-valley scattering processes as shown for D' in Fig. 2.9 (c, v). The features used to determine the layer thickness of graphene and an overview of Raman spectroscopy in $(\text{Mo}/\text{W})\text{S}_2$ will be discussed in chapter 3.1.

2.6 Superconductivity

Superconductivity was first discovered by Kamerlingh Onnes in 1911 [31], a few years after he liquified helium for the first time. It was not until the 50s and 60s however that a microscopic understanding of superconductors was developed in the Bardeen Cooper Schrieffer (BCS) theory, named after its creators [32, 33]. The theory successfully

describes many features found experimentally, as well as giving an insight into the processes that occur at the quantum level. The theory introduces the concept of a bound pairing of electrons, known as Cooper pairs. The quasi-particle pairs condense into a single ground state leaving a gap in the single electron density of states. It was shown that even a weak attractive interaction between the electrons can lead to the formation of the pairs. A mechanism for this attraction is qualitatively described by the electron-phonon interaction, whereby an electron travelling through a lattice, being negatively charged will attract nearby positively charged ions. Thus there will be a net positive charge in the vicinity of the electron. A second electron travelling through the crystal will be attracted to the first forming a weakly bound pair. If the strength of this interaction can overcome the Coulomb repulsion (such as at low temperatures), then superconductivity results. The BCS theory also ties in with the phenomenological Ginzburg-Landau description of superconductivity as a second-order phase transition [34]. The system is characterised by an order parameter representing the macroscopic wave function of all the superconducting electrons ψ . This has been shown to be proportional to the BCS predicted energy gap [35].

2.6.1 Cooper pairs and the BCS ground state

The binding of electron pairs was first proposed by Cooper in 1956, before the publication of the full BCS theory [36]. The idea is that the Fermi sea is unstable to the formation of the Cooper pairs in the presence of any attractive interaction, regardless of its strength. Consider the addition of two electrons to the Fermi sea at $T = 0$. If the electrons do not interact with the Fermi sea and only with each other, a Bloch wave function for lowest energy configuration can be described by:

$$\psi_0(\mathbf{r}_1, \mathbf{r}_2) = \sum_{\mathbf{k}} g_{\mathbf{k}} e^{i\mathbf{k}\cdot\mathbf{r}_1} e^{-i\mathbf{k}\cdot\mathbf{r}_2}. \quad (2.36)$$

Since the two electrons have opposite momenta and spin, they can be represented as a two-electron singlet wave function [37]:

$$\psi_0(\mathbf{r}_1 - \mathbf{r}_2) = \left[\sum_{\mathbf{k}} g_{\mathbf{k}} \cos \mathbf{k} \cdot (\mathbf{r}_1 - \mathbf{r}_2) \right] (\alpha_1 \beta_2 - \beta_1 \alpha_2), \quad (2.37)$$

where α_n represents the up spin state and β_n the down spin state of particle n . Eqn. 2.37 can be inserted into the Schrödinger equation, the eigenvalue E and the coefficients $g_{\mathbf{k}}$ can be determined by solving:

$$(E - 2\epsilon_{\mathbf{k}})g_{\mathbf{k}} = \sum_{k' < k_F} \mathbf{V}_{\mathbf{k}\mathbf{k}'} g_{\mathbf{k}'}, \quad (2.38)$$

here $\epsilon_{\mathbf{k}}$ are the unperturbed plane wave energies and $\mathbf{V}_{\mathbf{k}\mathbf{k}'}$ represents the matrix elements of the interaction potential. If a set of $g_{\mathbf{k}}$ exists that satisfies Eqn. 2.38 then there will exist a bound state with energy determined by the eigenvalue E . Cooper introduces an approximation that $\mathbf{V}_{\mathbf{k}\mathbf{k}'} = -V$ for energies $\hbar\omega_c$ away from the Fermi energy and $\mathbf{V}_{\mathbf{k}\mathbf{k}'} = 0$ beyond this energy [37]. Here ω_c is a cutoff frequency that specifies the energy range of the phonons that can interact with the electrons. The interaction is now constant and independent of \mathbf{k} . The $g_{\mathbf{k}}$ terms in Eqn. 2.38 can now be cancelled leading to:

$$\frac{1}{V} = \sum_{k' < k_F} (2\epsilon_{\mathbf{k}} - E)^{-1} = N(0) \int_{E_F}^{E_F + \hbar\omega_c} \frac{d\epsilon}{2\epsilon - E}, \quad (2.39)$$

where $N(0)$ is the density of states at the Fermi level. The solution to this equation is found using the weak-coupling approximation [37] and found to be:

$$E \approx 2E_F - 2\hbar\omega_c e^{-2/N(0)V}. \quad (2.40)$$

From this we can see that there is a bound state with a negative energy in respect to the Fermi surface. The wave function in Eqn. 2.37 to describe a single bound pair is not sufficient to describe the system when all of the electrons with energy up to $\hbar\omega_c$ have formed Cooper pairs. Instead a scheme of $N \times N$ Slater determinants can be used, where the singlet wave function as in Eqn. 2.37 becomes [37]:

$$|\psi_0\rangle = \sum_{k' < k_F} g_{\mathbf{k}} c_{\mathbf{k}\uparrow}^\dagger c_{-\mathbf{k}\downarrow}^\dagger |F\rangle, \quad (2.41)$$

where $c_{\mathbf{k}\uparrow}^\dagger$ is a creation operator and creates an electron of spin up and momentum \mathbf{k} , the corresponding annihilation operator $c_{\mathbf{k}\uparrow}$ empties the state. $|F\rangle$ represents all the filled states up to the Fermi level. The N-electron wave function can be expressed as:

$$|\psi_N\rangle = \sum g(\mathbf{k}_i, \dots, \mathbf{k}_t) c_{\mathbf{k}_i\uparrow}^\dagger c_{-\mathbf{k}_i\downarrow}^\dagger \dots c_{\mathbf{k}_t\uparrow}^\dagger c_{-\mathbf{k}_t\downarrow}^\dagger |\phi_0\rangle, \quad (2.42)$$

where $|\phi_0\rangle$ represents the vacuum state with no particles and the indices i and t represent the first and last values of \mathbf{k} within the particular summation. The number of summations required to compute this form of the wave function is enormous and so BCS use a mean-field approach in which the occupancy of each \mathbf{k} state is only dependent on the average occupancy of the other states [37]. The ground state BCS wave function has the form:

$$|\psi_G\rangle = \prod_{\mathbf{k}} (u_{\mathbf{k}} + v_{\mathbf{k}} c_{\mathbf{k}\uparrow}^\dagger c_{-\mathbf{k}\downarrow}^\dagger) |\phi_0\rangle, \quad (2.43)$$

where $u_{\mathbf{k}}$ and $v_{\mathbf{k}}$ are related to the occupation probabilities of a paired state such

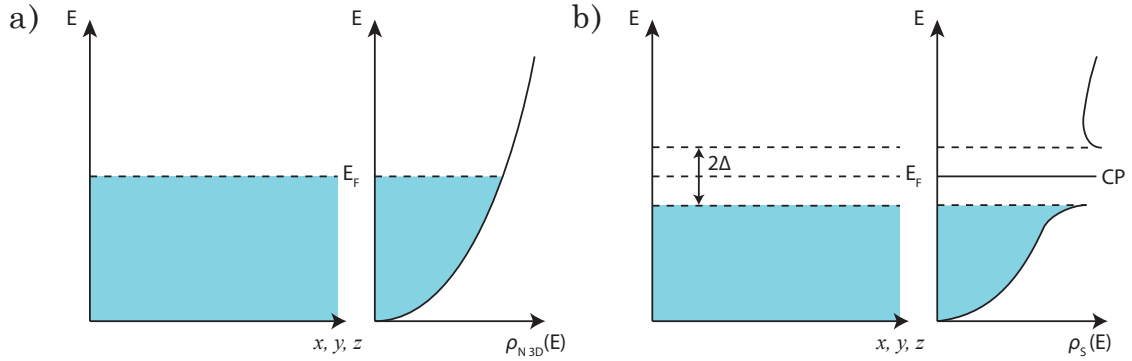


Figure 2.10: The single electron density of states and filled energy levels for **a)** a typical normal metal and **b)** a BCS superconductor. In the density of states for the superconductor at the Fermi level there is a delta function (labelled CP) representing the quasi-particle Cooper pair density of states.

that $|u_{\mathbf{k}}|^2 + |v_{\mathbf{k}}|^2 = 1$. The probability of a state $(\mathbf{k} \uparrow, -\mathbf{k} \downarrow)$ being occupied is $|v_{\mathbf{k}}|^2$ and unoccupied is $|u_{\mathbf{k}}|^2 = 1 - |v_{\mathbf{k}}|^2$. Since all of the electrons are paired into this ground state, the single electron density of states now has a gap of the size 2Δ ; as shown in Fig. 2.10 (b). The BCS theory predicts the size of this gap at $T = 0$ to be directly proportional to the superconducting transition temperature T_C :

$$\Delta_0 = 1.76k_B T_C \quad (2.44)$$

$$\Delta(T \rightarrow T_C) = 1.74\Delta_0 \left(1 - \frac{T}{T_C}\right)^{1/2}, \quad (2.45)$$

and the temperature dependence is valid as T approaches T_C .

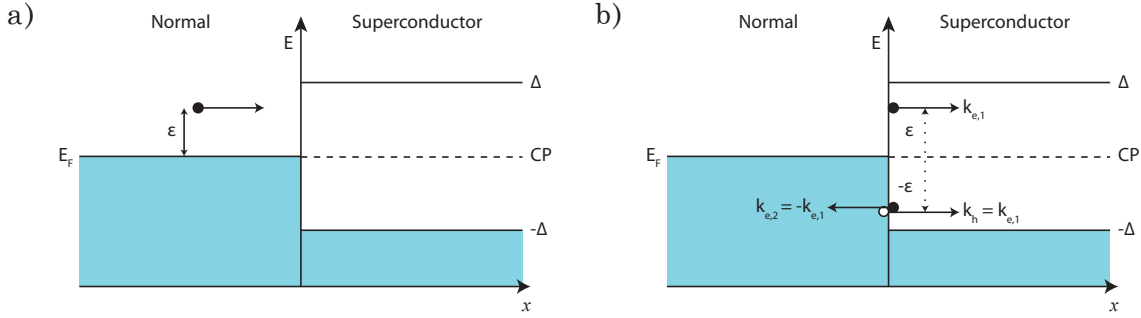


Figure 2.11: Andreev reflection: **a)** An electron in a normal metal lead impinging upon the superconductor interface with energy $E_F + \epsilon$ where $\epsilon < \Delta$. **b)** The charge transfer process at the interface during Andreev reflection; a total charge of $2e$ is transferred to the superconductor. Electrons are shown as filled black circles and holes as outlined circles.

2.6.2 Andreev reflection

Andreev Reflection at an NS interface

Andreev reflection describes the charge transfer process that occurs at the interface between a normal metal (N) and a superconductor (S), it was first proposed by Andreev in 1964 [38]. Consider the NS interface in Fig. 2.11, an electron with energy $E_1 = E_F + \epsilon$ (such that $\epsilon < \Delta$) that impinges upon the NS interface. The electron has momentum $k_{e,1}$ and a positive velocity. As per the density of states in Fig. 2.10, the electron should not be able to tunnel into the superconductor as there are no available states to hop into, instead a more complicated process happens as shown in Fig. 2.11 (b). To tunnel into the superconductor a second electron with energy $E_2 = E_F - \epsilon$ is required, this has opposite momentum to the first electron $k_{e,2} = -k_{e,1}$ and opposite spin. These two electrons form a time-reversed bound (Cooper) pair in the superconductor [39], but for this to happen a hole is left in the normal metal at energy $E_F - \epsilon$. This hole has opposite momentum to the second electron, but due to the negative mass of the hole, its velocity will be opposite to the original incoming electron. This means that the hole

traces back the path of the original electron, known as retro-reflection. However perfect retro-reflection only occurs when the incident electron energy $E_{e,1} = E_F$ [40]. Due to the energy difference between the incident electron and reflected hole ($E_{e,1} = E_h + 2\epsilon$) there will be a small difference in the momentum of each particle such that $|k_{e,1}| > |k_h|$ (assuming $m_e = -m_h$). In the Andreev reflection process the energy, momentum and charge must be conserved. The energy of the incident electrons and the hole before the reflection process must be equal to the energy of the Cooper pair and the hole after:

$$E_{e,1} + E_{e,2} + E_h = E_{CP} + E_h = 3E_F - \epsilon, \quad (2.46)$$

to conserve momentum, the difference $\Delta k = k_e - k_h$ is taken by the Cooper pair. A consequence of this momentum difference is that the reflected hole will de-phase as it retraces the path of the electron. Δk takes the value of [39]:

$$\Delta k = \frac{2\epsilon}{\hbar v_F}, \quad (2.47)$$

which corresponds to a de-phasing length (over which the hole phase changes by π), given by [39, 41]:

$$L = \frac{\pi}{\Delta k} = \frac{\hbar v_F}{4\epsilon} \quad (2.48)$$

$$\xi = \frac{\hbar v_F}{4\Delta}, \quad (2.49)$$

where ξ can be considered the coherence length for the maximum case where $\epsilon = \Delta$. Finally, a transfer of charge of $2e$ across the interface effectively doubles the conductance when the conditions for Andreev reflection are met (as compared to when the superconductor is in the normal metal state). The transmission (T) and reflectance (R) probabilities at the interface can be modelled by considering a δ -function poten-

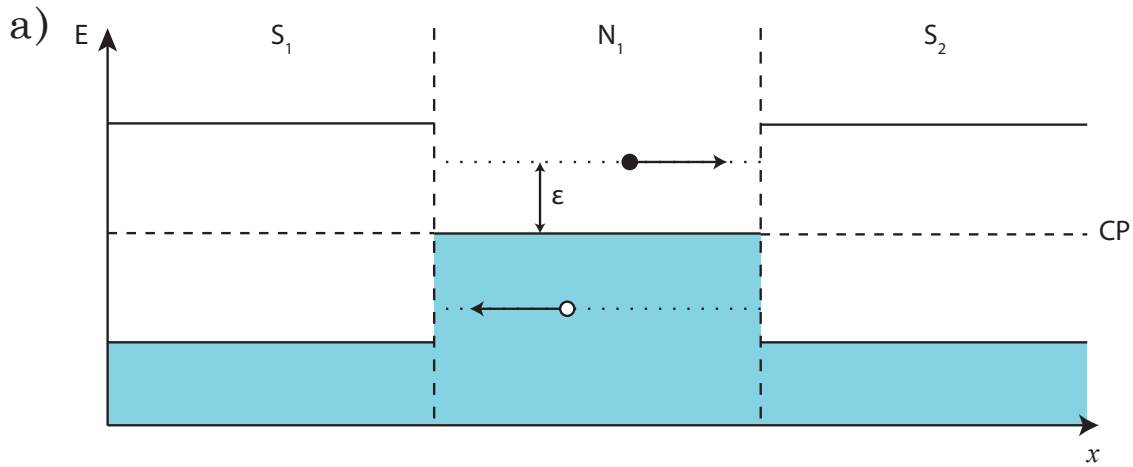


Figure 2.12: Andreev reflection in a SNS junction. Electrons are represented by filled black circles, holes by outlined circles.

tial barrier at the interface of strength Z and then solving the Bogoliubov equations [42]. The resulting T and R values can describe the conductance through the interface for a range of conditions from the case where every electron is Andreev reflected and the conductance doubled, through to the tunnelling behaviour seen in S-Insulator(I)-S junctions [43].

Andreev reflection at an SNS interface

Now consider the case of a SNS junction shown in Fig. 2.12, also known as a Josephson junction. In this case, both the superconducting materials are the same, but the wave functions describing the macroscopic Cooper pair condensate have different phases ϕ_1 and ϕ_2 . An electron in the normal metal with energy $E_F + \epsilon$ travelling towards the superconducting lead S_2 will undergo Andreev reflection at the interface. A hole is reflected back towards the other lead S_1 , with energy $E_F - \epsilon$. When the hole reaches the interface at S_1 , the reverse process of Andreev reflection occurs and a Cooper pair

in S_1 , is broken up into two electrons in the normal metal. This process effectively transfers a Cooper pair from S_1 to S_2 , the electronic states in the normal metal form a bound state if the phase of the electron remains the same after one cycle.

Andreev reflection at a graphene-S interface

The Andreev reflection process in undoped graphene is expected to be specular [44]. Fig. 2.13 gives an overview of different reflection processes. Specular reflection at a NI interface sees an electron reflected about the same angle to the normal, Fig. 2.13 (a). Andreev retro-reflection, as discussed in the previous sections, at an NS interface sees a hole retro-reflected back along the same path as the incident electron Fig. 2.13 (b). This is also true for doped graphene, where both of the electrons contributing to the Cooper pair come from the conduction band (although different valleys due to time reversal symmetry). However when electrons from undoped graphene form a Cooper pair, one will be from the conduction band and the other from the valence band. In this case the hole will also be reflected back in the valence band and will cause a change in sign of the velocity of the hole when compared to the doped case. This causes a specular reflection of the hole, Fig. 2.13 (c). The transition from the specular to retro-reflection regimes is expected to show an inversion of the voltage dependence of the subgap conductance of the interface [44]. If the ballistic conductance through a graphene-S interface in the normal state is g_0 ; in the superconducting state with regular Andreev retro-reflection, you would expect to see this conductance increase from $\frac{4}{3}g_0$ to $2g_0$ as V_{bias} approaches Δ . This corresponds to a charge of $2e$ being transferred across the interface instead of one electron in the normal metal conduction regime. For the case of specular Andreev reflection it is expected to drop in magnitude from $2g_0$ to $\frac{4}{3}g_0$ as V_{bias} approaches Δ . So far the signatures of specular reflection have not been seen

experimentally due to inhomogeneous charge puddles that exist at ‘zero’ doping [45]. It has been suggested that a de-phasing of the injected electrons occurs at the boundaries between the electron/hole and charge neutral puddles; this results in a suppression of the Josephson super current [46].

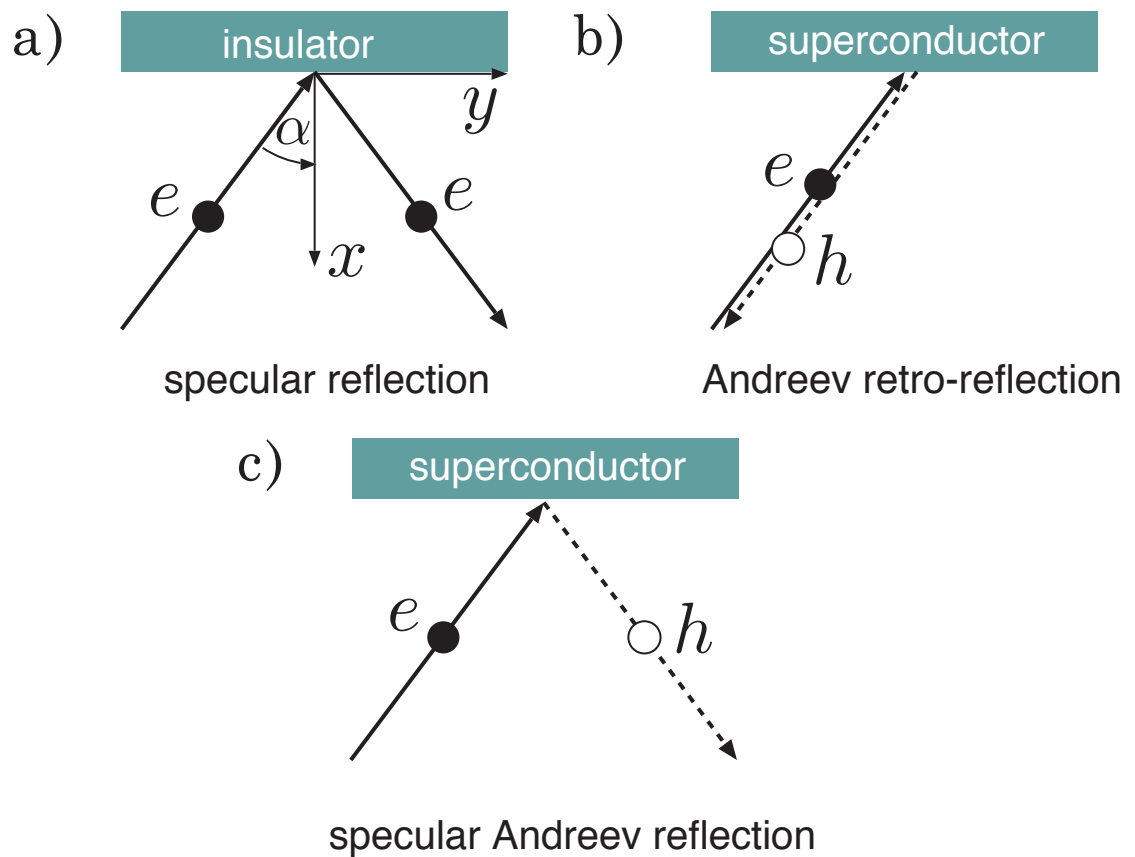


Figure 2.13: Reflection processes between: **a)** A normal metal and an insulator; an electron is specularly reflected back into the normal metal. **b)** A normal metal and a superconductor or doped graphene and a superconductor; an electron undergoes Andreev reflection and a hole is retro-reflected. **c)** Undoped graphene and a superconductor; the Andreev reflection process is specular meaning the hole is specularly reflected. Adapted from [44].

Bibliography

- [1] P. R. Wallace, Phys. Rev. **71**, 622 (1947).
- [2] G. D. R. Saito, M.S. Dresselhaus, *Physical Properties of Carbon Nanotubes* (Imperial College Press, London, 1998).
- [3] S. Reich, J. Maultzsch, C. Thomsen, and P. Ordejón, Phys. Rev. B **66**, 035412 (2002).
- [4] M. I. Katsnelson, *Graphene Carbon in Two Dimensions* (Cambridge University Press, 2012).
- [5] L. B. Ebert, Annual Review of Materials Science **6**, 181 (1976).
- [6] M. Inagaki, Journal of Materials Research **4**, 1560 (1989).
- [7] O. Leenaerts, H. Peelaers, A. D. Hernández-Nieves, B. Partoens, and F. M. Peeters, Phys. Rev. B **82**, 195436 (2010).
- [8] F. Withers, S. Russo, M. Dubois, and M. Craciun, Nanoscale Research Letters **6**, 526 (2011).
- [9] F. Withers, T. H. Bointon, M. Dubois, S. Russo, and M. F. Craciun, Nano Letters **11**, 3912 (2011).

-
- [10] M. Chhowalla, H. S. Shin, G. Eda, L.-J. Li, K. P. Loh, and H. Zhang, *Nat Chem* **5**, 263 (2013).
- [11] K. F. Mak, C. Lee, J. Hone, J. Shan, and T. F. Heinz, *Phys. Rev. Lett.* **105**, 136805 (2010).
- [12] H. R. Gutiérrez, N. Perea-López, A. L. Elías, A. Berkdemir, B. Wang, R. Lv, F. López-Urías, V. H. Crespi, H. Terrones, and M. Terrones, *Nano Letters* **13**, 3447 (2013).
- [13] Q. H. Wang, K. Kalantar-Zadeh, A. Kis, J. N. Coleman, and M. S. Strano, *Nat Nano* **7**, 699 (2012).
- [14] B. Radisavljevic, A. Radenovic, J. Brivio, V. Giacometti, and A. Kis, *Nat Nano* **6**, 147 (2011).
- [15] K. F. Mak, K. He, C. Lee, G. H. Lee, J. Hone, T. F. Heinz, and J. Shan, *Nat Mater* **12**, 207 (2013).
- [16] A. Kuc, N. Zibouche, and T. Heine, *Phys. Rev. B* **83**, 245213 (2011).
- [17] Z. Y. Zhu, Y. C. Cheng, and U. Schwingenschlögl, *Phys. Rev. B* **84**, 153402 (2011).
- [18] K. Kośmider, J. W. González, and J. Fernández-Rossier, *Phys. Rev. B* **88**, 245436 (2013).
- [19] D. Xiao, G.-B. Liu, W. Feng, X. Xu, and W. Yao, *Phys. Rev. Lett.* **108**, 196802 (2012).
- [20] K. F. Mak, K. He, J. Shan, and T. F. Heinz, *Nat Nano* **7**, 494 (2012).

-
- [21] B. I. Shklovskii and A. L. Efros, *Electronic Properties of Doped Semiconductors*, vol. Vol. 45 (Springer Series in Solid State Sciences, Berlin, 1984).
- [22] N. F. Mott, *Journal of Non-Crystalline Solids* **1**, 1 (1968).
- [23] N. F. Mott, *Philosophical Magazine* **19**, 835 (1969).
- [24] N. F. Mott, *Journal of Non-Crystalline Solids* **8–10**, 1 (1972).
- [25] A. L. Efros and B. I. Shklovskii, *Journal of Physics C: Solid State Physics* **8**, L49 (1975).
- [26] A. L. Efros, *Journal of Physics C: Solid State Physics* **9**, 2021 (1976).
- [27] A. C. Ferrari and D. M. Basko, *Nat Nano* **8**, 235 (2013).
- [28] J.-A. Yan, W. Y. Ruan, and M. Y. Chou, *Phys. Rev. B* **77**, 125401 (2008).
- [29] L. Malard, M. Pimenta, G. Dresselhaus, and M. Dresselhaus, *Physics Reports* **473**, 51 (2009).
- [30] A. C. Ferrari, J. C. Meyer, V. Scardaci, C. Casiraghi, M. Lazzeri, F. Mauri, S. Piscanec, D. Jiang, K. S. Novoselov, S. Roth, et al., *Phys. Rev. Lett.* **97**, 187401 (2006).
- [31] H. K. Onnes, *Leiden Comm.* **120b**, **122b**, **124c** (1911).
- [32] J. Bardeen, L. N. Cooper, and J. R. Schrieffer, *Phys. Rev.* **106**, 162 (1957).
- [33] J. Bardeen, L. N. Cooper, and J. R. Schrieffer, *Phys. Rev.* **108**, 1175 (1957).
- [34] V. L. Ginzburg and L. D. Landau, *Zh. Eksperim. i Teor. Fiz.* **20** (1950).
- [35] L. P. Gor'kov, *Zh. Eksperim. i Teor. Fiz.* **36** (1959).

-
- [36] L. N. Cooper, Phys. Rev. **104**, 1189 (1956).
- [37] M. Tinkham, *Introduction to Superconductivity* (McGraw-Hill, New York, 1996).
- [38] A. Andreev, JETP **19**, 1228 (1964).
- [39] T. M. Klapwijk, **17**, 593 (2004).
- [40] B. Pannetier and H. Courtois, **118**, 599 (2000).
- [41] H. van Houten and C. Beenakker, Physica B: Condensed Matter **175**, 187 (1991).
- [42] G. E. Blonder, M. Tinkham, and T. M. Klapwijk, Phys. Rev. B **25**, 4515 (1982).
- [43] B. Josephson, Physics Letters **1**, 251 (1962).
- [44] C. W. J. Beenakker, Phys. Rev. Lett. **97**, 067007 (2006).
- [45] J. Martin, N. Akerman, G. Ulbricht, T. Lohmann, J. H. Smet, K. von Klitzing, and A. Yacoby, Nat Phys **4**, 144 (2008).
- [46] K. Komatsu, C. Li, S. Autier-Laurent, H. Bouchiat, and S. Guéron, Phys. Rev. B **86**, 115412 (2012).

Chapter 3

Device fabrication and measurement techniques

3.1 Device fabrication procedures

3.1.1 Mechanical exfoliation and fabricating a simple transistor structure

It is the weak van der Waals interaction between the layers in graphite (and other similar layered materials) that allow it to be easily cleaved by an adhesive tape; the crystal reduces in thickness with each repeated peeling. To obtain a high probability of finding monolayer flakes, a high density of thin graphite peelings is required on the tape. The most crucial factor however is the cleanliness of the substrate that the flakes are being deposited on. Presence of dirt or residues may prevent the flakes from adhering to the substrate and they will remain stuck to the tape instead. Devices in this thesis are fabricated on p-doped Silicon substrates with a 280 nm SiO₂ dielectric layer, except where stated otherwise. After peeling the tape from the substrate, few

layer flakes are identified initially with an optical microscope, see Sec. 3.3.1 and then when required with Raman spectroscopy, Sec. 3.3.2.

Electron beam lithography (EBL) is employed to define metallic contacts. A polymer resist, poly(methyl methacrylate) (PMMA) is chosen for its sensitivity to high energy electrons. Upon exposure the polymer chains are broken into smaller pieces; this makes them more readily removable by a particular development solvent, methyl isobutyl ketone (MIBK). The PMMA can be applied to the substrate by spin coating at a high rpm, usually around 4000 - 7000 rpm. The thickness of the film is sensitive to the spin speed and the concentration of the PMMA. Thicknesses from around 60 - 700 nm can be achieved by varying these factors. The substrate is then baked on a hot plate, above the glass transition temperature of the PMMA (180°C) for 2 to 10 minutes to remove the solvent component. The resist is exposed by e-beam lithography to define a geometry for the metallic contacts Fig. 3.1 (a) and then the sample is developed in MIBK for 20 - 40 seconds to remove the exposed areas Fig. 3.1 (b). Modern electron beam systems use a Monte Carlo simulation to determine the backscattering of the electrons from the substrate through the PMMA. In this way the dose of applied electrons can be modified locally to sharply define the edges of the exposed areas. Metals can now be deposited by means of thermal evaporation or sputter deposition Fig. 3.1 (c). The unwanted metal is removed by immersion in a solvent such as acetone to completely remove the PMMA; this process is known as lift-off, Fig. 3.1 (d). In systems that do not use dose scaling, a bi-layer of PMMA is recommended where the lower layer has a shorter polymer chain length than the upper layer. The lower layer is then more susceptible to the electrons and an under cut region created to aid the lift-off of the evaporated metals.

After lift-off, the substrate can be packaged in an electrical chip carrier. the EBL

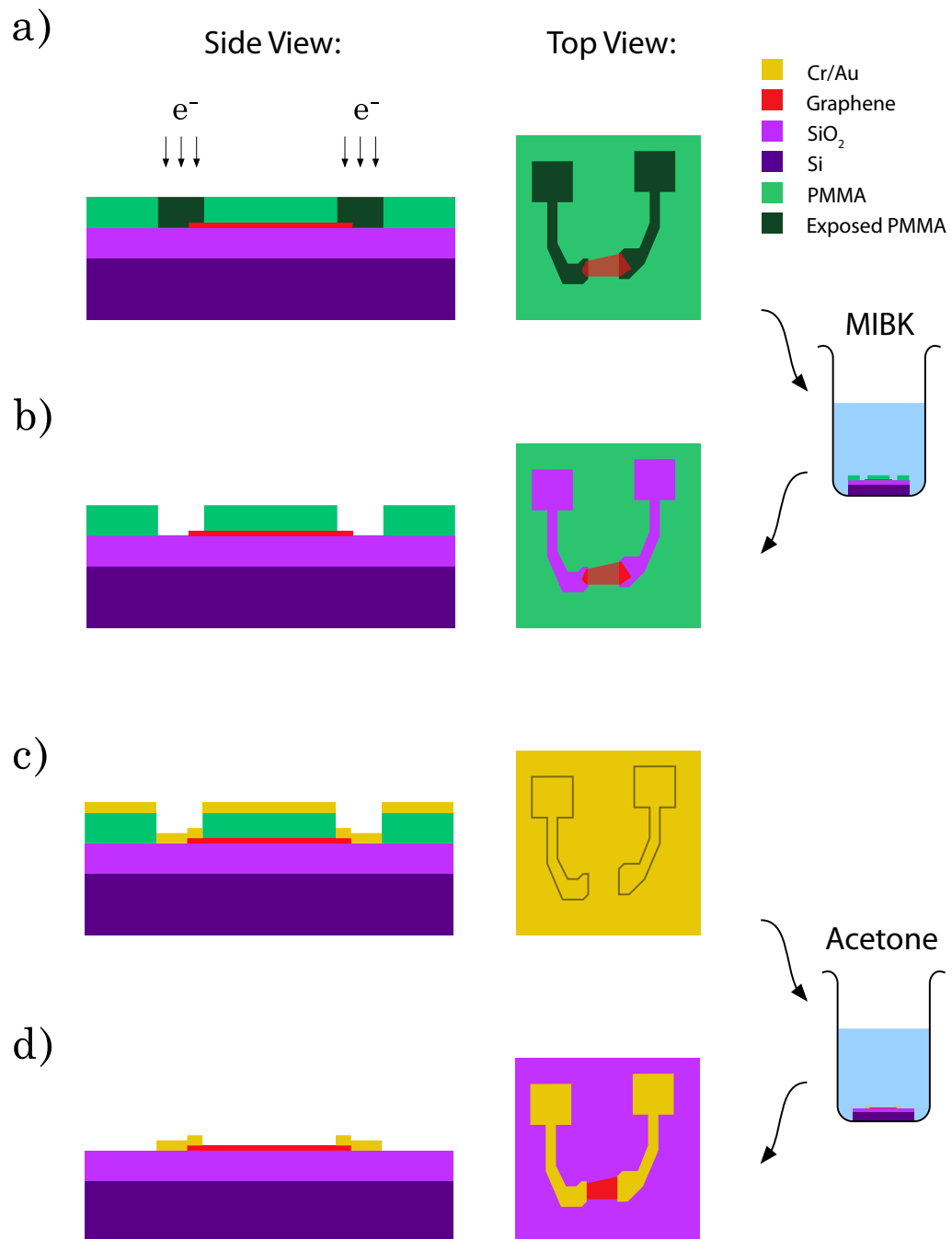


Figure 3.1: Standard electron beam lithography procedure for depositing metallic contacts: **a)** After spin coating PMMA resist, it is exposed to electron beam irradiation defining a pattern for metallic contacts. **b)** The exposed regions are removed by developing in MIBK for 20 seconds. **c)** The metals for the contacts are evaporated onto the substrate; a discontinuous film is achieved by the developed regions. **d)** The unwanted metal can be removed by dissolving the remaining PMMA in acetone.

defined contacts can be linked to the chip carrier by means of an ultrasonic wire bonder. The cleanliness of the lithography process determines how easy it is to bond wires to the device. If there is dirt or residue on top of the contacts then a good quality bond may not result, or the wire will simply refuse to attach. Likewise if there are residues underneath the evaporated metals, then the metal may tear away from the substrate upon bonding. Gold contacts do not adhere to SiO_2 very well, so a thin layer of an adhesion metal is required, usually 4 - 10 nm of chrome or titanium. Incorrect choice of the adhesion layer can cause other problems as will be seen in section 5.2.

3.1.2 Methods of suspending atomically thin materials

Initial research on graphene was performed using supported flakes on silicon substrates with a thin oxide layer. A simple transistor structure can be fabricated using the oxide layer as a global back gate. Supported devices often show a low mobility of around $1,000 - 10,000 \text{ cm}^2/\text{Vs}$ [1]. Charge trap states and other impurities in the dielectric environment disrupt the transport through the graphene sheet; since there is no screening of the coulomb potential in monolayer graphene. Freely suspending the graphene offers a way to characterise its electrical properties without the influence of the substrate. In doing so mobilities in excess of $200,000 \text{ cm}^2/\text{Vs}$ have been obtained [2]. In addition to the massive increase in the quality of samples obtained, suspending samples opens new avenues for research. For example, the mechanical properties of graphene can be explored using high frequency modulation of the back gate to vibrate the sheet. Owing to the higher values of charge carrier mobilities that can be achieved in suspended devices, it is possible to measure the quantum Hall effect at lower magnetic fields and higher temperatures. Furthermore phase coherent processes such as the Aharonov-Bohm effect will be easier to observe in suspended devices; potentially approaching macroscopic

phase coherence at high temperatures. In this section a number of ways of suspending graphene and other 2D materials are highlighted. These methods were used to create devices in this thesis such as in chapter 6, where the intrinsic transport properties of MoS₂ are investigated in an environment free of the influence of a substrate. The two latter methods were developed without wet etching of the substrate and are applicable to chapter 5, where the ultimate goal is to create Josephson junctions with a suspended graphene weak link.

Suspended atomically thin transistors fabricated by wet etching the substrate

Hydrofluoric (HF) acid can be used to etch SiO₂ as it does not damage the graphene [2], nor does it etch silicon. Fig. 3.2 (a) gives an overview of the etching process starting from a transistor structure as described in the previous section; the substrate is then placed in HF acid Fig. 3.2 (b). The etching process of SiO₂ is isotropic, however the regions of SiO₂ covered by graphene and the metallic contacts can only be etched from the sides protecting the SiO₂ underneath them. Therefore careful choice of flake size is needed for suspending graphene. If the flake is too wide then the HF acid will not etch fully underneath the graphene, likewise if the widths of the contacts are too small they can be fully under-etched and will collapse. A schematic of the profile of a desired undercut after etching is shown in Fig. 3.2 (c). The rate of etching is 80 nm per minute for 50% buffered HF. Devices can be suspended with etches as shallow as 50 nm but the probability of success is increased with deeper etches due to role of surface tension effects. When drying the sample it is possible for droplets of the liquid to pull the graphene sheet down and stick it to the substrate. A method of avoiding this is to reduce the surface tension of the liquid before drying. This is achieved by heating IPA

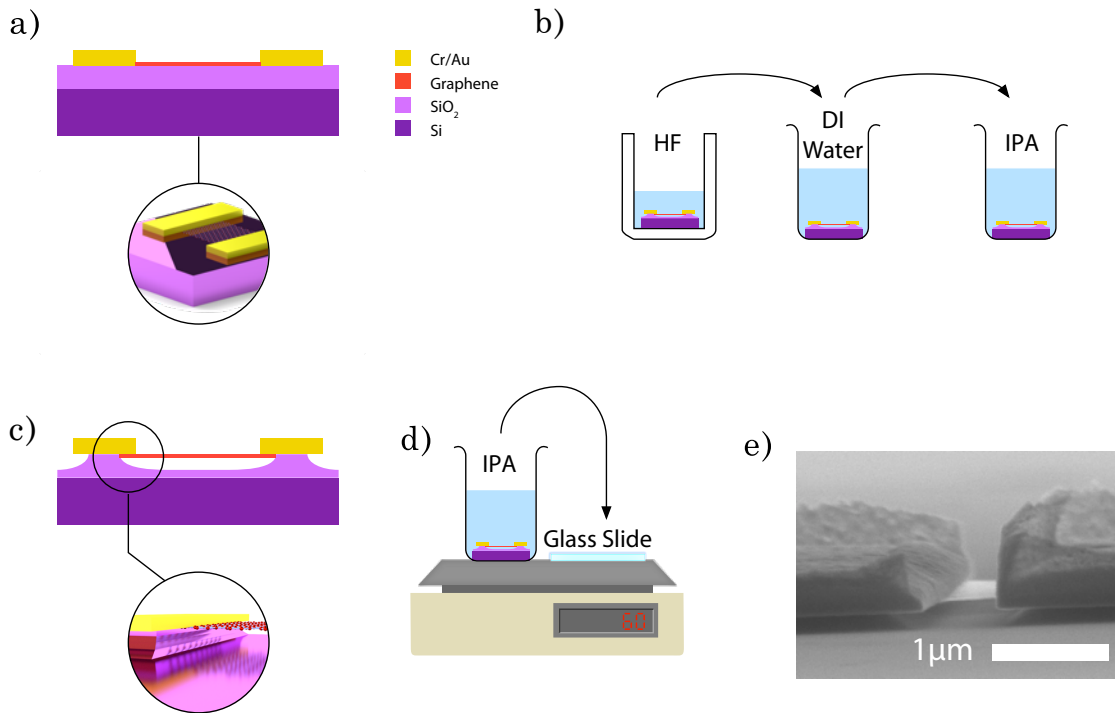


Figure 3.2: Hydrofluoric acid etching process: **a)** A schematic showing the supported sample after metallic contact deposition but before the etching process. **b)** The device is placed in a buffered HF solution for 2.5 mins, which etches 200 nm; then it is subsequently transferred to DI water then IPA. **c)** A view of an etched sample, the oxide layer is 300 nm thick, so a thin layer still remains after etching; however there is an undercut beneath the gold contacts. **d)** The IPA is heated to 60°C and then transferred to a glass slide on a hot plate. This causes the IPA to evaporate with low surface tension. **e)** SEM image of a suspended graphene device.

to 60°C and drying the device on a glass slide heated by a hot plate as depicted in Fig. 3.2 (d). A SEM image of a finished device is shown in Fig. 3.2 (e), the undercut can be clearly seen underneath the metallic contacts. Flakes with lengths in excess of 2 μm have been suspended using this method but there are numerous disadvantages to using HF acid. In gas and vapour form it is highly corrosive to the lungs, while in liquid form it is highly toxic and can be readily absorbed through the skin. The acid reacts with calcium and magnesium ions in the bloodstream disrupting critical processes within the body. It can be fatal even with burns covering only a small area of skin. HF is also not compatible with many metals, particularly superconductors. In order to be able to suspend graphene flakes with any superconducting conducting metal, two alternate methods relying on polymer-based sacrificial layers are investigated and described in the next sections.

Suspended devices with a PMMA sacrificial layer

PMMA is a commonly used polymer in electron beam lithography as described in section 3.1.1. It is a positive tone resist which means the areas that are exposed are removed upon development. When the PMMA is exposed to a much higher dose than than for standard EBL, the polymer chains bond together (cross-linking) and become much less affected by solvents such as acetone; which usually remove PMMA from the substrate. It has been demonstrated that PMMA can be used as a high resolution negative resist in this manner [3]. PMMA is spun onto a Si/SiO₂ wafer and then flakes of graphene are mechanically exfoliated onto the PMMA as shown in Fig. 3.3 (a). Due to the high doses required to cross-link PMMA (10000 C/m²), it would take an extremely long time to pattern the area underneath all of the contacts and leads to the flakes. With this in mind the PMMA is only cross-linked close to the flake and a PMMA

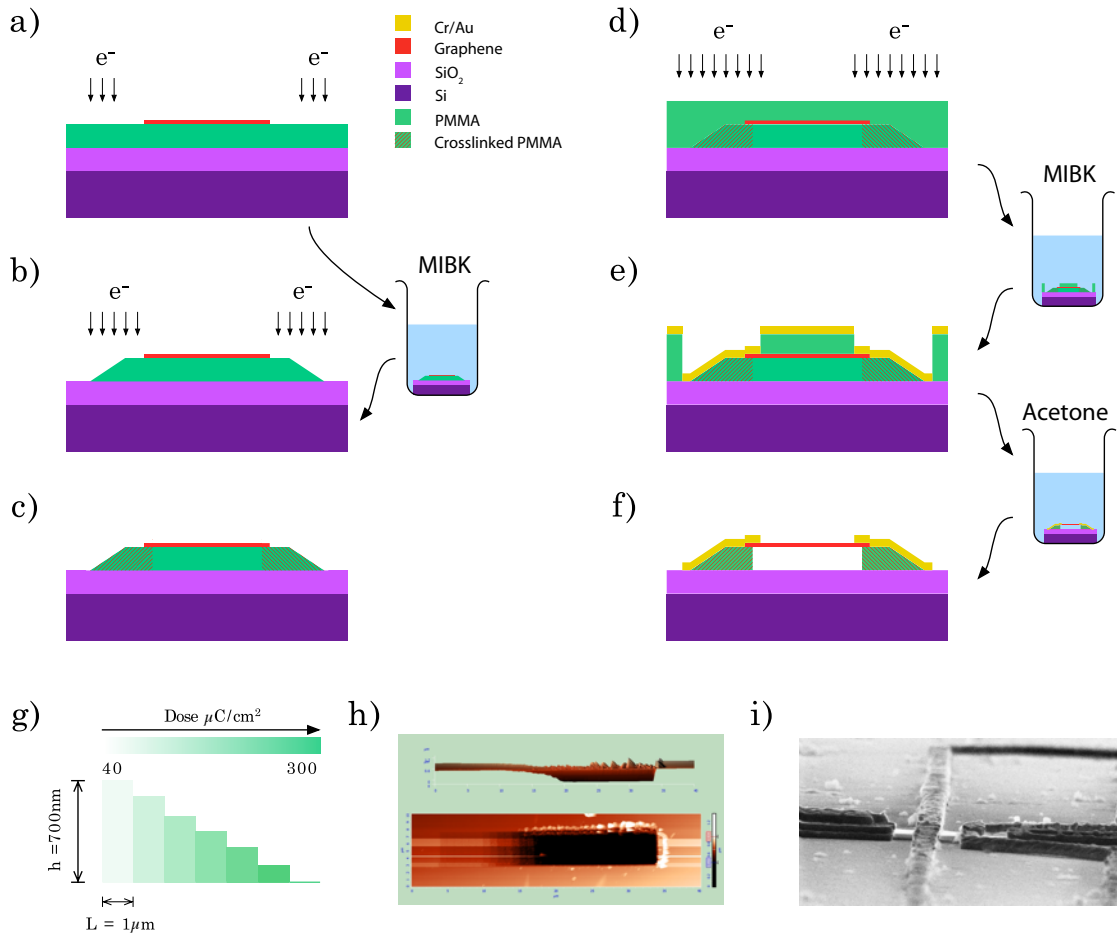


Figure 3.3: Cross-linked PMMA suspension process: **a)** PMMA is spun onto a SiO₂ substrate and then few layer flakes are mechanically exfoliated onto the PMMA. A ramp from the PMMA surface down to the SiO₂ is constructed by a varying low dose of e-beam exposure. **b)** The PMMA is developed in MIBK leaving the ramps in tact. A large dose is then applied to the ramps to cause them to cross-link as shown in **c)**. **d)** A new layer of PMMA is spun on top to fill the gaps and allow the standard procedure of e-beam lithography to take place in step **e)**. **f)** For the final lift-off step in acetone all of the PMMA will be removed except for the cross-linked regions. Depending on how thick the layer of cross-linked PMMA is, it may be necessary to dry the sample on a hotplate as in Fig. 3.2. **g)** Dose versus height calibration for the PMMA ramps. **h)** AFM measurement of a PMMA ramp courtesy of Thomas Bointon. **i)** SEM image of a finished device showing two suspended regions.

ramp down to the SiO₂ substrate is created. To do this, first the PMMA is exposed using a much lower dose than for standard PMMA development and incrementing this more and more until it completely develops the PMMA as shown in Fig. 3.3 (b). Typical doses to create the ramp are shown in Fig. 3.3 (g) and an AFM scan of a test ramp structure in Fig. 3.3 (h). After developing the ramp structure in MIBK, the device is exposed to e-beam irradiation again, but in this case the dose is much higher than for standard PMMA development. Fig. 3.3 (c) shows that the area of the ramp leading up to the flake is cross-linked. A new layer of PMMA is spun on top to allow standard deposition of metallic contacts Fig. 3.3 (d, e, f). A SEM image of a finished device is shown in Fig. 3.3 (i). The main advantage of this process stems from its use of standard lithography chemicals and solvents, making it compatible with almost any metal; it is also not an inherently dangerous process. Cross-linked PMMA channels of down to 500 nm were tested but there is potential for even narrower cross linked regions. Disadvantages of this method are the long exposure times for cross-linking and that it requires three separate e-beam exposures. This can introduce contamination in the form of residues lowering the electrical quality of the devices produced.

Suspended devices with HSQ negative resist.

Hydrogen silsesquioxane (HSQ), upon exposure to e-beam irradiation at standard doses is cross-linked and reduces into amorphous silicon. Feature sizes of less than 10 nm wide have been achieved [4]. This property can be exploited to quickly fabricate suspended devices with only one e-beam exposure step. The SiO₂ substrate is initially prepared by spinning a thin ~ 150 nm layer of HSQ. Graphene flakes are exfoliated onto the HSQ and a layer of PMMA is spun on top of the flakes, Fig. 3.4 (a). Metallic contacts can be deposited in the standard way by exposing the PMMA, developing in MIBK,

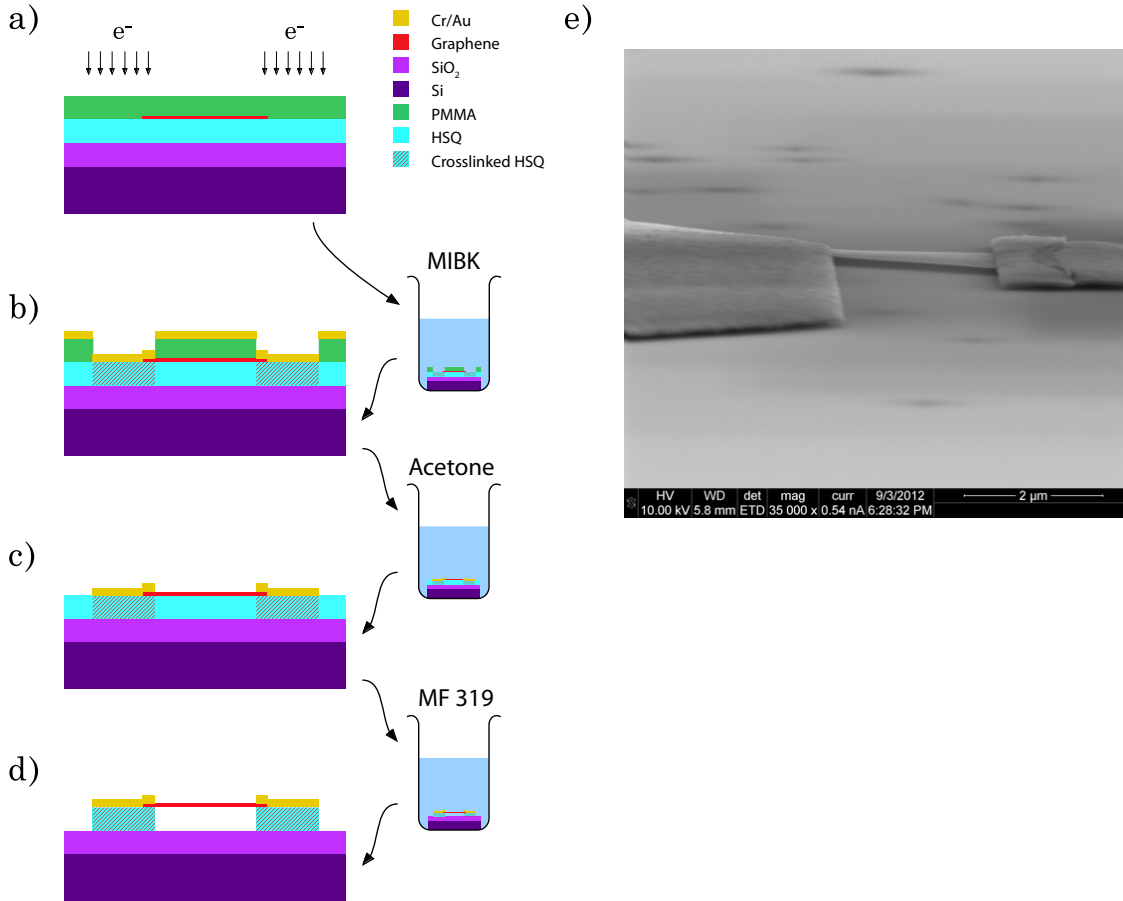


Figure 3.4: HSQ suspension process: **a)** HSQ is spun onto SiO₂ and few layer flakes are then mechanically exfoliated onto HSQ. A layer of PMMA is then spun on top of this structure and the regions defining the contacts are exposed by standard e-beam doses. **b)** The exposure cross-links the HSQ, so after the PMMA is developed the HSQ remains untouched. Metallic contacts can be deposited. **c)** The metal is removed by lift-off in acetone but this does not affect the unexposed HSQ. **d)** To remove the unexposed HSQ and suspend the flakes the sample is washed in MF 319. It is then dried on a hot plate as in Fig. 3.2. **f)** SEM image of a finished device.

evaporating metal, and lifting off in acetone as usual, Fig. 3.4 (b, c). The difference is that the regions of HSQ underneath the metal that were exposed to define the contacts will be cross-linked. The HSQ provides a stable base for the contacts to sit on. The developer and lift-off solvents for the PMMA do not affect the HSQ, which can be removed with MF 319. The device is then dried using the hot IPA method described previously, Fig. 3.4 (d). A SEM image of a finished device is shown in Fig. 3.4 (e). While quick to produce devices, the main disadvantage of this method is that the reproducibility of HSQ exposures is difficult to obtain. A systematic study is required to find consistent bake, dose and development parameters for features of different sizes. There is considerable study into this field in the literature [4, 5, 6].

3.1.3 Improved performance through annealing

During the fabrication procedure the graphene flakes can become contaminated with residues of the lithography polymers and water among other things. This has the effect of a) doping the graphene and b) reducing the mobility of the material. There are two main methods that can be used to remove these contaminants. The first involves heating the sample in a hot walled furnace, Fig. 3.5 (a). The temperature of the furnace needs to be hot enough to remove contaminants from the surface of the device but also needs to be low enough as not to damage the metallic contacts; 200°C achieves both of these conditions. The device should also be grounded so that no particular contact lead can build up electrostatic charge during the process. The annealing can be performed in either a vacuum or by flowing an argon/hydrogen gas mixture over the device and should be left for several hours. A disadvantage of using this method to anneal is that as soon as the sample is exposed to the air it will start to become contaminated again. With this in mind an in situ solution would be preferred. The

second method involves passing a high current through the device which will then heat the device via Joule heating. When the sample is in contact with the substrate at a low temperature the substrate will act as a large heat sink; thus this method is more suited to suspended devices or those exhibiting a large resistivity. A schematic of a typical circuit used to perform current annealing is shown in Fig. 3.5 (b). It is necessary to monitor the resistance of the sample when annealing. A large decrease in resistance will lead to more current flowing through the device which may cause the destruction of the flake. Fig. 3.5 (c) displays a typical $R(V_g)$ dependence for graphene before and after several annealing cycles. Notice that the charge neutrality point shifts towards zero volts, indicating the removal of dopants. The shape of the peak becomes narrower and sharper, indicating an improvement of the mobility of the sample.

3.2 Synthesis of fluorinated graphene

Fluorinated graphene (FG) can be obtained in a number of different ways; including plasma fluorination of bulk flakes [8]; or suspending graphene flakes on metallic grids before exposing them to a fluorinating agent [9]. The methods used in this thesis involve the intercalation of bulk graphite then exfoliating directly from the crystal. One method involves intercalating the bulk graphite in atmosphere of F_2 gas at temperatures above 300°C . However the intercalation conditions are harsh on the graphite. It introduces many physical defects making it difficult to obtain monolayer flakes [10]. A better method for intercalation uses a fluorinating agent, XeF_2 , at a much lower temperature (120°C). The XeF_2 decomposes into xenon and atomic fluorine allowing the fluorine atoms to disperse between the graphene sheets and adsorb onto the surface [11].

Upon fluorination the sp^2 hybridised structure of the graphene is modified as the

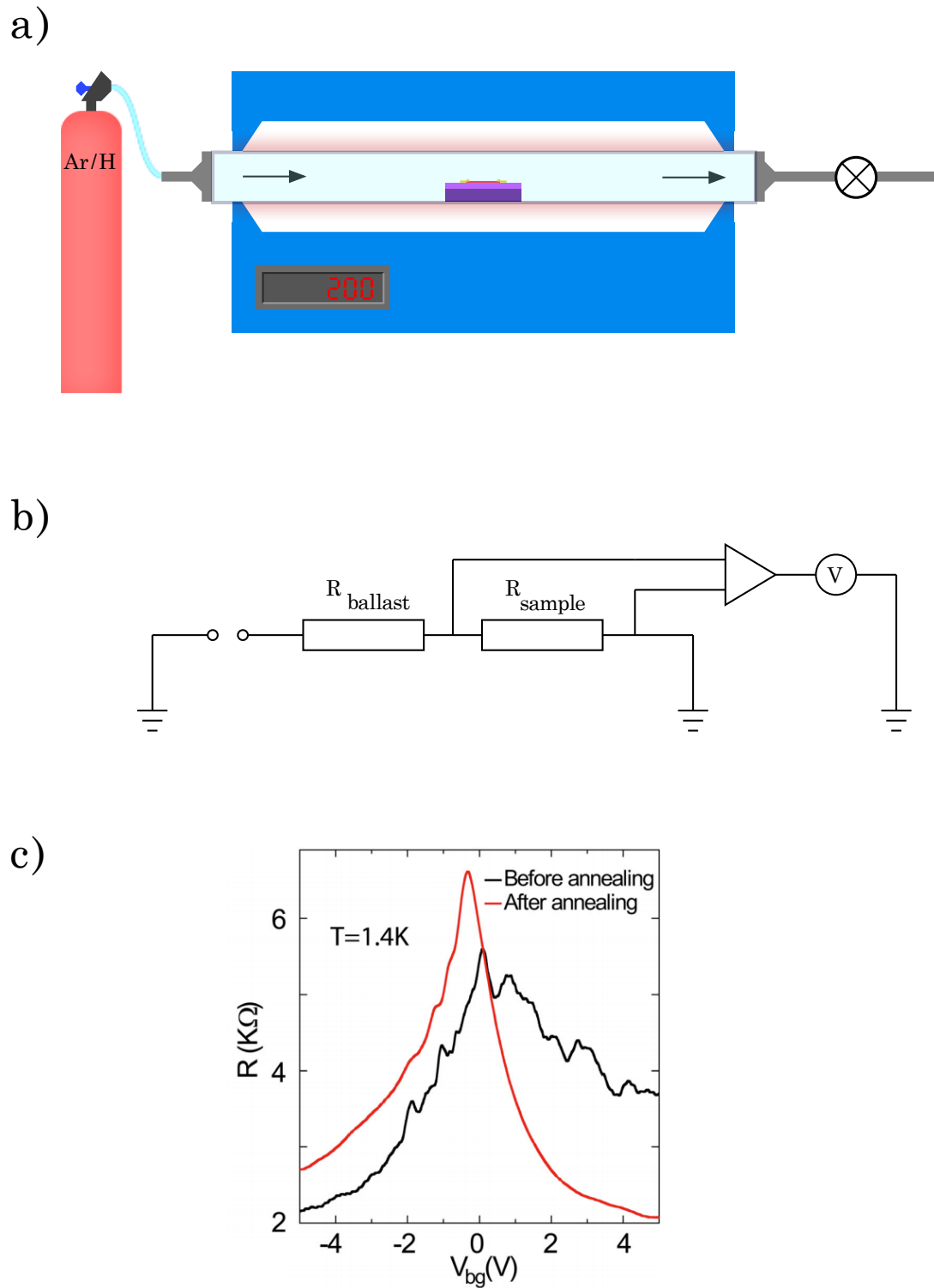


Figure 3.5: Device annealing methods: **a)** Heating in a furnace at 200°C under either a hydrogen/argon atmosphere (pictured) or vacuum. **b)** Electrical circuit for current annealing. **c)** Back gate dependence of resistance for a graphene flake before and after current annealing [7].

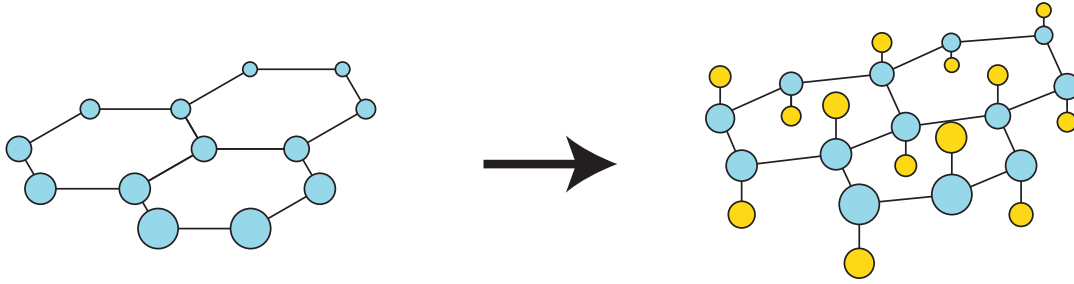


Figure 3.6: Representations of the sp^2 hybridised structure of graphene (left) and the sp^3 hybridised structure of fully fluorinated graphene (right).

fluorine atoms form sp^3 bonds with the carbon atoms as shown in Fig. 3.6. The angle between a carbon atom and two nearest neighbours is reduced from 120° to $\sim 110^\circ$ for the chair configuration of fluorine atoms [12]. In this configuration fluorine atoms on alternating carbon atoms are bonded to opposite sides of the graphene sheet.

3.3 Characterisation of 2D materials

3.3.1 Optical contrast of graphene

Despite being one atomic layer thick, graphene absorbs a relatively large amount of light. The amount absorbed is independent of the wavelength from the infrared to visible. This is due to the linear band structure around the Fermi level and is related to the fine structure constant, $\pi\alpha = 2.293\%$ [13]. The choice of substrate is very important when trying to observe graphene optically; subtle interference effects with the thin dielectric layer of SiO_2 can enhance the contrast of graphene [14]. The optical contrast compared with the substrate increases with number of layers and can be to determine up to three layers as seen in Fig. 3.7 (a, b).

The method used to generate the contrast involves taking optical microscope im-

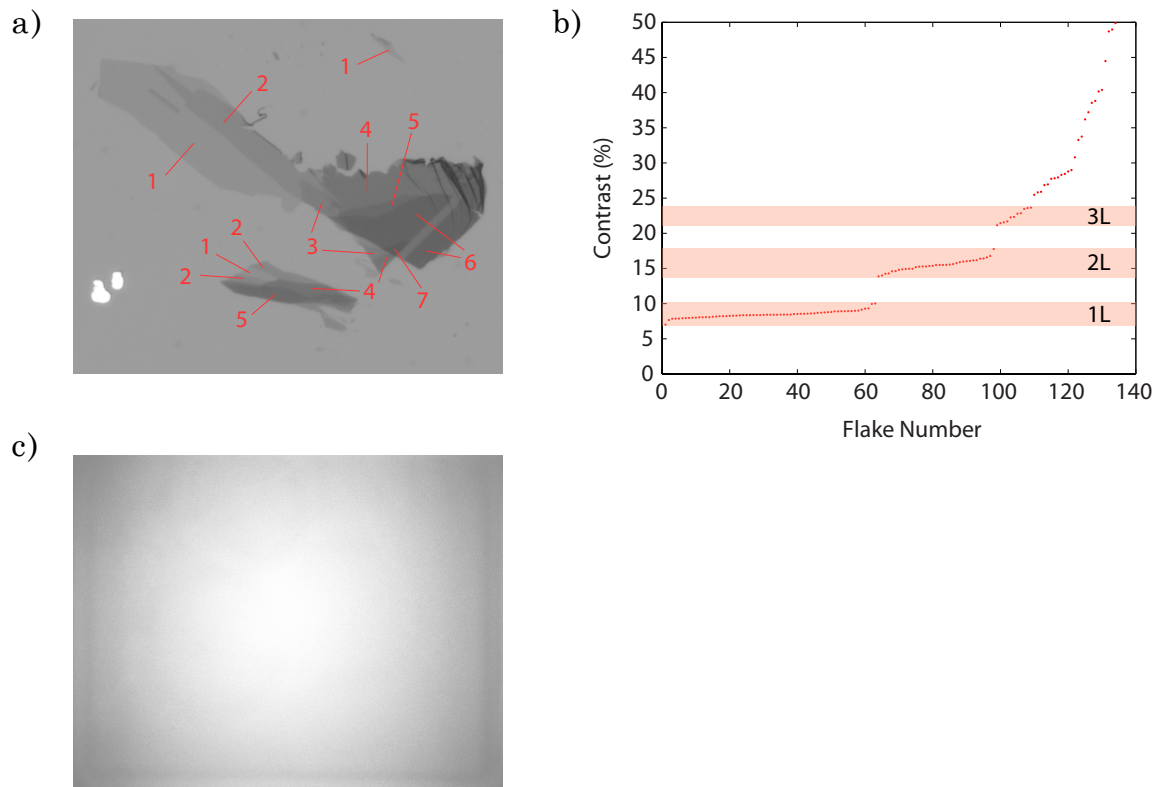


Figure 3.7: a) An example of multiple graphene flakes of different thicknesses; ranked in order of increasing contrast. b) The measured average contrast of over 130 graphene flakes. There are clear plateaus distinguishing up to three layers. c) An example of a vignette that is subtracted from the optical images (the contrast has been modified to exaggerate the effect).

ages of the flakes; making sure that consistent brightness, magnification and exposure settings are used. Then near to each flake a clean region of the substrate with no ‘debris’ is found and photographed with the same settings (this will be referred to as a background image). This can be used to subtract a background from the images of the flakes with the ultimate goal of making the substrate near uniform in pixel colour. The need to subtract a background arises from; a) a vignette effect around the edges of the images due to the optics of the microscope; b) small variations in the height of the substrate and residues on the surface can change the reflection of the light from the surface; c) a difference in the uniformity of the incident light on the substrate. Of these problems only the discrepancies in the height of the substrate cannot be accounted for. Although they can be minimised by taking a background image near the particular flake. A profile of the vignette can be created from the background image by sampling the average pixel colour near the centre of the image. This is then thought to be the ‘correct’ background colour (since graphene is most visible through a green filter only the green pixel value is used). A map of the image is created detailing the difference between each pixel value and the correct colour, Fig. 3.7 (c). After removing the vignette, the next step is to remove the non-uniform lighting of the substrate. One way of doing this is to plot the pixel values of a single row and fit a curve to the data. This can be repeated for each row and column of the image to build up a 3D surface representing the image. After subtraction the background is uniform and contrasts can be measured using the equation:

$$C = \frac{P_{\text{substrate}} - P_{\text{graphene}}}{P_{\text{substrate}}} \times 100, \quad (3.1)$$

where C is the contrast as a percentage and P represents the average pixel value of the green channel of the image for either graphene or the substrate. This method can

give a good estimate up to 3 layers and the method is quick to perform as it can be automated; however it cannot give any detailed information about the flakes such as the stacking order in trilayer flakes. Raman spectroscopy discussed in the next section can give a more accurate determination of the number of layers as well as a wealth of other information.

3.3.2 Determining the number of graphene layers using Raman spectroscopy

In chapter 2.5.2, the processes contributing to the Raman spectrum of graphene were introduced. Here the features of the spectrum that can be used to determine layer thickness are discussed. Fig. 3.8 displays the evolution of the 2D-peak in the Raman spectrum for graphene flakes from single to 4-layer and bulk graphite. For monolayer graphene (Fig. 3.8 (a)) the 2D-band has a symmetric shape and is formed from a single peak. This makes it quite distinctive and easily identifiable from thicker graphene sheets; the intensity of the 2D-peak is also much larger than the G-peak for monolayers. Bi-layer graphene also has a unique shape (Fig. 3.8 (b)), the 2D band becomes a multi-peak structure that can be fitted by 4 Lorentzians. For bilayer, the intensity of the 2D-peak and G-peak is comparable. For tri-layer graphene, Raman spectroscopy can be used to determine the stacking order of the graphene flakes [15]; the peak can be fitted with 6 Lorentzians. The intensity of the G-peak is larger than the 2D-peak. The full width at half maximum (FWHM) of the 2D-band can be used to determine layer number up to trilayer with $\sim 26.3 \text{ cm}^{-1}$ for monolayer, $\sim 52.1 \text{ cm}^{-1}$ for bilayer and $\sim 56.1 \text{ cm}^{-1}$ for trilayer [16].

For accurate determination of thicker flakes a different method is required. For samples on Si/SiO₂ the Raman spectrum accrues a significant amount of background

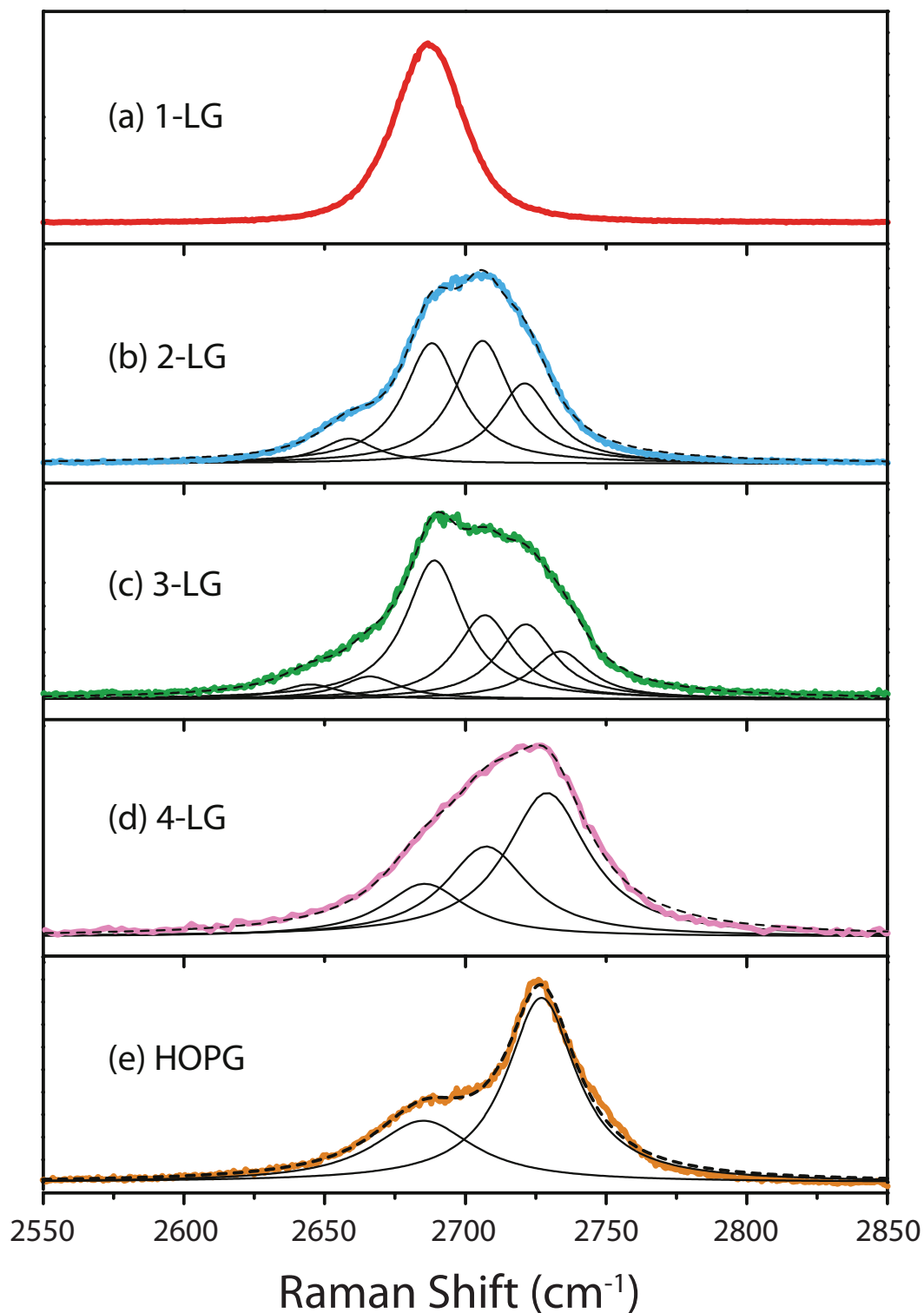


Figure 3.8: Raman spectra for graphene flakes of different layer numbers. The solid black lines are Lorentzian fits to the 2D-peak and the dashed black line is the final fit. Adapted from [17].

noise plus a peak for the silicon. After subtraction of the background the silicon peak can be used as a reference to determine the number of graphene layers. The ratio of the G-band intensity to the Si-peak intensity correlates with layer count. The intensity of the G-band increases with more carbon atoms (layers) and the amount of light reaching the silicon is decreased thus the Si-peak intensity also decreases [18]. Raman spectroscopy can also be used to gain a wealth of other useful information from the graphene such as: an estimate of the number of defects from the ratio of the D and G-peaks [19]; doping level can be identified from the position of the G-mode [20]; a split in the G-peak characterises strain [21].

Raman spectra of MoS₂ and WS₂

MoS₂ and WS₂ share many common properties, their unit cell differs by the substitution of only one chemically similar atom. When comparing the electronic and phononic band structures of the materials they appear at first glance very similar; differing only slightly in energies at the high symmetry points, Fig. 3.9 (a, b). The Raman spectrum of the two are also similar. There are three key Raman modes which can be used to characterise the number of layers of these materials. The E_{2g}^1 and A_{1g} modes are both at the Γ -point and the 2LA(M) mode is at the M-point. A representation of the atomic vibrations of these modes are shown in Fig. 3.9 (d), the $E_{2g}^1(\Gamma)$ mode represents an in-plane shear mode with opposite motion of the chalcogen to the transition metal. The $A_{1g}(\Gamma)$ mode corresponds to out of plane counter oscillations of the chalcogen atoms. Due to the coupling between the (W/Mo)S₂ layers this mode is damped for increasing layer number and so displays a large shift in the Raman spectrum. The 2LA(M) mode is attributed to phonons at the M-point and is activated by disorder, it is a shear mode between adjacent layers. In both MoS₂ [24] and WS₂ [25] for an excitation wavelength

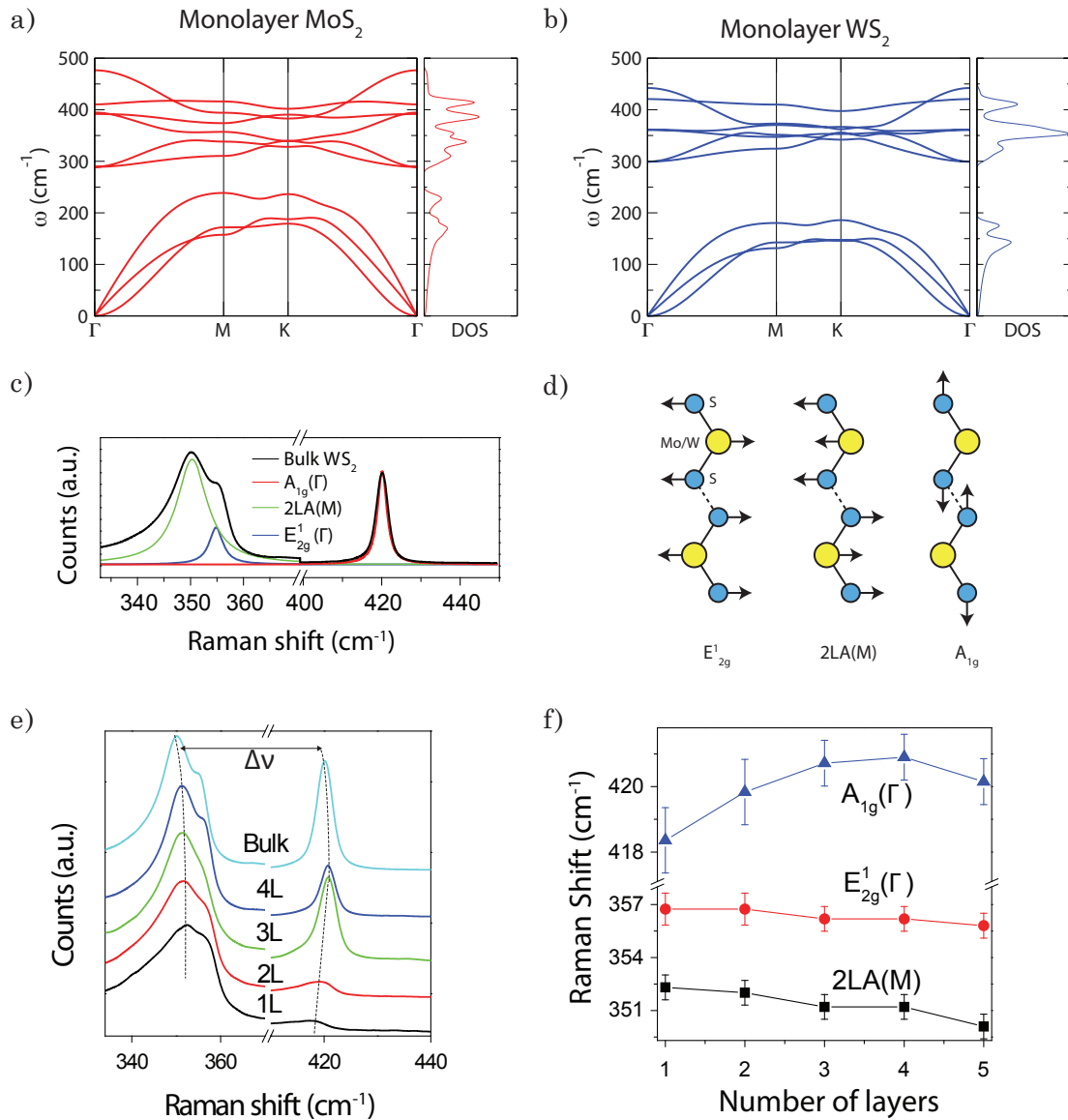


Figure 3.9: Raman characterisation of TMDs. **a)** Phonon dispersion for monolayer MoS₂ (left) **b)** and WS₂ (right), adapted from [22]. **c)** Raman spectrum of bulk WS₂, the peak at 350 cm⁻¹ is fitted to two Lorentzians corresponding to the $E_{2g}^1(\Gamma)$ and $2LA(M)$ modes; the peak at 420 cm⁻¹ corresponds to the $A_{1g}(\Gamma)$ mode [23]. **d)** The vibrational directions of the atoms for the $E_{2g}^1(\Gamma)$ mode (left), the $2LA(M)$ mode (centre) and the $A_{1g}(\Gamma)$ mode (right). **e)** Raman spectrum of WS₂ for increasing number of layers [23]. **f)** Peak positions of the Raman active modes for increasing layer count [23]. All Raman spectra in this figure were taken with a laser wavelength of 532 nm with a spot size of 1.5 μ m and 1 mW incident power.

of 488 nm the E_{2g}^1 and A_{1g} modes will shift apart with increasing layer number. The Raman spectrum for bulk WS_2 with an excitation wavelength of 532 nm is presented in Fig. 3.9 (c). The $E_{2g}^1(\Gamma)$ peak has a shift of 350 cm^{-1} and the $A_{1g}(\Gamma)$ peak has a shift of 420 cm^{-1} . At this excitation wavelength the $E_{2g}^1(\Gamma)$ peak is dwarfed by the 2LA(M) mode. The evolution of the WS_2 Raman spectra with increasing number of layers is shown in Fig. 3.9 (e) and the shift between the $E_{2g}^1(\Gamma)$ and 2LA(M) peaks can be used to determine layer number as shown in Fig. 3.9 (f).

3.4 Electrical characterisation

3.4.1 Graphene and constant current measurements

A quick way to determine the quality of the graphene is to measure its field effect mobility. Typical measurements involve changing the electric field applied perpendicular to the graphene sheet and measuring the resistance of the device. This can be achieved by the use of a global back gate, which modifies the Fermi level of the graphene. Fig. 3.10 (a) displays a typical gate voltage dependence of the resistance along with schematic representations of the band structure indicating the position of the Fermi level. A constant current scheme is typically used to measure the $R(V_g)$ dependence as shown in Fig. 3.10 (b). Applying a negative gate voltage lowers the Fermi level and allows hole transport; while applying a positive gate voltage increases the Fermi level and brings the system into the electronic regime. For a perfect sample at zero gate voltage the Fermi level sits exactly between the conduction and valence band. Despite the density of states of graphene equaling zero here, it still displays sheet conductivity on the order of $4e^2/h$ [26]. If the Dirac peak is shifted from the $V_g = 0$ position (with no gate applied) then it indicates that the sample could be

doped by contaminants such as water; annealing the sample can return the peak close to zero as discussed earlier. To determine the mobility of the system we can model the Si/SiO₂/Graphene heterostructure as a parallel plate capacitor with capacitance per unit area $C_g = C/A = \epsilon_r \epsilon_0 / d$ with the SiO₂ dielectric layer thickness $d = 280$ nm. The capacitance of the system is also related to the applied gate voltage by $C = Q/V_g$ where Q is the charge of the total number of carriers N in the system $Q = Ne$. We can therefore relate the carrier density to the gate voltage.

$$n = C_g V_g / e. \quad (3.2)$$

The gate voltage applied here assumes that the sample is undoped for $V_g = 0$, if the position of the neutrality point is shifted then we can account for this by replacing V_g with $\delta V_g = V_g - V_0$ in Eqn. 3.2. In the Drude model the mobility of the system is given by $\mu = \sigma / ne$ so combining with Eqn. 3.2 gives

$$\mu = \frac{\sigma}{C_g \delta V_g} = \frac{\sigma d}{\epsilon_r \epsilon_0 \delta V_g}. \quad (3.3)$$

3.4.2 TMDs and constant voltage measurements

MoS₂ and WS₂ are often heavily n-doped and due to their large band gaps it is not possible to access the hole transport regime without liquid ionic gating [29] or high work function contacts [30]. The sample resistances are often much higher as well which leads to a transistor behaviour as seen in Fig. 3.10 (c). The current flow through the devices is measured while the back gate is swept using the setup as in Fig. 3.10 (d). This kind of setup is known as constant voltage; the voltage is known and applied directly to the device. The field effect mobility can be extracted from linear region of the $I(V_g)$

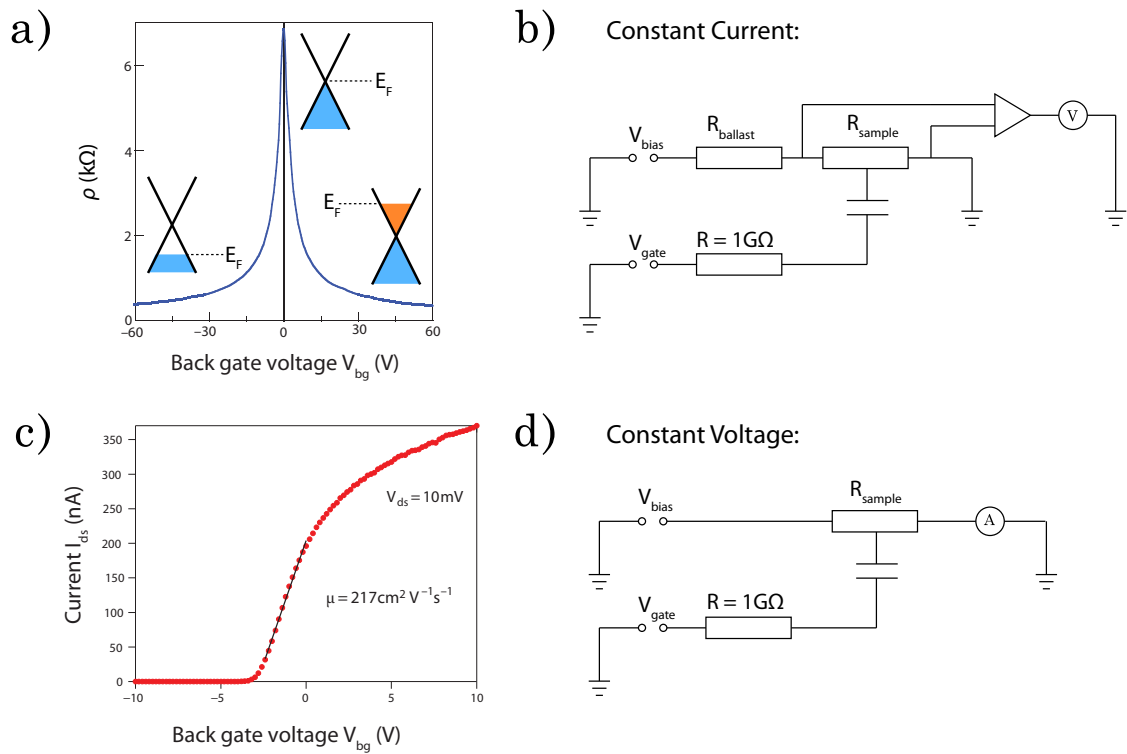


Figure 3.10: **a)** Gate voltage dependence of the resistivity $R(V_g)$ for a monolayer graphene transistor device, adapted from [27]. **b)** Constant current circuit diagram for measuring $R(V_g)$. **c)** Gate voltage dependence of the source-drain current $I(V_g)$ for a monolayer MoS₂ device, adapted from [28]. **d)** Constant voltage circuit diagram for measuring $I(V_g)$.

dependence using a similar analysis to the $R(V_g)$ dependence of graphene. The mobility is given by:

$$\mu = \frac{dI_{sd}}{dV_g} \times \frac{L}{Wc_gV_{sd}}, \quad (3.4)$$

where L and W are the channel length and width respectively. The mobilities of TMDs are generally quite low and can be improved by encapsulating the device in a high- κ dielectric environment such as hafnium-oxide [28].

3.5 Summary

In this chapter an overview of device fabrication procedures and material characterisation was presented. In particular two new methods of suspending 2D materials have been shown which do not involve the wet etching of the oxide layer on the substrate. The first involves the cross-linking of PMMA to create permanently raised structures upon which metallic contacts are deposited. The second uses a high resolution negative tone resist to achieve a similar effect but with a quicker fabrication procedure. These methods of suspending 2D materials have a particular relevance when used in combination with superconducting metals, as the acid used in the traditional wet etching of SiO_2 also etches most superconductors. In addition, a method of removing the background profile from optical microscope images has been discussed which can give good identification of the number of layers of graphene up to tri-layer.

Bibliography

- [1] K. S. Novoselov, A. K. Geim, S. V. Morozov, D. Jiang, Y. Zhang, S. V. Dubonos, I. V. Grigorieva, and A. A. Firsov, *Science* **306**, 666 (2004).
- [2] K. Bolotin, K. Sikes, Z. Jiang, M. Klima, G. Fudenberg, J. Hone, P. Kim, and H. Stormer, *Solid State Communications* **146**, 351 (2008).
- [3] I. Zailer, J. E. F. Frost, V. Chabasseur-Molyneux, C. J. B. Ford, and M. Pepper, *Semiconductor Science and Technology* **11**, 1235 (1996).
- [4] J. K. W. Yang, B. Cord, H. Duan, K. K. Berggren, J. Klingfus, S.-W. Nam, K.-B. Kim, and M. J. Rooks, *Journal of Vacuum Science and Technology B* **27**, 2622 (2009).
- [5] S.-W. Nam, M. J. Rooks, J. K. W. Yang, K. K. Berggren, H.-M. Kim, M.-H. Lee, K.-B. Kim, J. H. Sim, and D. Y. Yoon, *Journal of Vacuum Science and Technology B* **27**, 2635 (2009).
- [6] A. Grigorescu, M. van der Krogt, C. Hagen, and P. Kruit, *Microelectronic Engineering* **84**, 822 (2007).
- [7] T. Khodkov, F. Withers, D. C. Hudson, M. F. Craciun, and S. Russo, *Applied Physics Letters* **100**, (2012).

-
- [8] S. B. Bon, L. Valentini, R. Verdejo, J. L. Garcia Fierro, L. Peponi, M. A. Lopez-Manchado, and J. M. Kenny, *Chemistry of Materials* **21**, 3433 (2009).
- [9] R. R. Nair, W. Ren, R. Jalil, I. Riaz, V. G. Kravets, L. Britnell, P. Blake, F. Schedin, A. S. Mayorov, S. Yuan, et al., *Small* **6**, 2877 (2010).
- [10] F. Withers, S. Russo, M. Dubois, and M. Craciun, *Nanoscale Res. Lett.* **6**, 526 (2011).
- [11] W. Zhang, L. Spinelle, M. Dubois, K. Guérin, H. Kharbache, F. Masin, A. Kharitonov, A. Hamwi, J. Brunet, C. Varenne, et al., *Journal of Fluorine Chemistry* **131**, 676 (2010).
- [12] O. Leenaerts, H. Peelaers, A. D. Hernández-Nieves, B. Partoens, and F. M. Peeters, *Phys. Rev. B* **82**, 195436 (2010).
- [13] K. F. Mak, L. Ju, F. Wang, and T. F. Heinz, *Solid State Communications* **152**, 1341 (2012).
- [14] P. Blake, E. W. Hill, A. H. Castro Neto, K. S. Novoselov, D. Jiang, R. Yang, T. J. Booth, and A. K. Geim, *Applied Physics Letters* **91**, (2007).
- [15] C. Cong, T. Yu, K. Sato, J. Shang, R. Saito, G. F. Dresselhaus, and M. S. Dresselhaus, *ACS Nano* **5**, 8760 (2011).
- [16] Y. Hao, Y. Wang, L. Wang, Z. Ni, Z. Wang, R. Wang, C. K. Koo, Z. Shen, and J. T. L. Thong, *Small* **6**, 195 (2010).
- [17] L. Malard, M. Pimenta, G. Dresselhaus, and M. Dresselhaus, *Physics Reports* **473**, 51 (2009).
- [18] Y. K. Koh, M.-H. Bae, D. G. Cahill, and E. Pop, *ACS Nano* **5**, 269 (2011).

-
- [19] L. G. Cançado, A. Jorio, E. H. M. Ferreira, F. Stavale, C. A. Achete, R. B. Capaz, M. V. O. Moutinho, A. Lombardo, T. S. Kulmala, and A. C. Ferrari, *Nano Letters* **11**, 3190 (2011).
- [20] A. Das, S. Pisana, B. Chakraborty, S. Piscanec, S. K. Saha, U. V. Waghmare, K. S. Novoselov, H. R. Krishnamurthy, A. K. Geim, A. C. Ferrari, et al., *Nat Nano* **3**, 210 (2008).
- [21] T. M. G. Mohiuddin, A. Lombardo, R. R. Nair, A. Bonetti, G. Savini, R. Jalil, N. Bonini, D. M. Basko, C. Galiotis, N. Marzari, et al., *Phys. Rev. B* **79**, 205433 (2009).
- [22] A. Molina-Sánchez and L. Wirtz, *Phys. Rev. B* **84**, 155413 (2011).
- [23] F. Withers, T. H. Bointon, D. C. Hudson, M. F. Craciun, and S. Russo, *Sci. Rep.* **4** (2014).
- [24] H. Li, Q. Zhang, C. C. R. Yap, B. K. Tay, T. H. T. Edwin, A. Olivier, and D. Baillargeat, *Advanced Functional Materials* **22**, 1385 (2012).
- [25] A. Berkdemir, H. R. Gutierrez, A. R. Botello-Mendez, N. Perea-Lopez, A. L. Elias, C.-I. Chia, B. Wang, V. H. Crespi, F. Lopez-Urias, J.-C. Charlier, et al., *Sci. Rep.* **3** (2013).
- [26] K. S. Novoselov, A. K. Geim, S. V. Morozov, D. Jiang, M. I. Katsnelson, I. V. Grigorieva, S. V. Dubonos, and A. A. Firsov, *Nature* **438**, 197 (2005).
- [27] A. K. Geim and K. S. Novoselov, *Nat Mater* **6**, 183 (2007).
- [28] B. Radisavljevic, A. Radenovic, J. Brivio, V. Giacometti, and A. Kis, *Nat Nano* **6**, 147 (2011).

- [29] Y. Zhang, J. Ye, Y. Matsushashi, and Y. Iwasa, *Nano Letters* **12**, 1136 (2012).
- [30] S. Chuang, C. Battaglia, A. Azcatl, S. McDonnell, J. S. Kang, X. Yin, M. Tosun, R. Kapadia, H. Fang, R. M. Wallace, et al., *Nano Letters* **14**, 1337 (2014).

Chapter 4

Atomically thin and flexible beta radiation detectors based on fluorinated graphene

4.1 Introduction

In this chapter it is demonstrated that fluorinated graphene (FG) can be utilised to detect beta radiation. The high energy electrons reaching the device break the carbon-fluorine (CF) bonds; reducing the FG back to graphene in a similar manner to that of electron beam assisted de-fluorination of the FG [1]. During this process the initially insulating devices become increasingly more conductive and the IV characteristic tends towards ohmic behaviour. A strontium-90 (^{90}Sr) radioactive source is used as an emitter of beta particles and the decay process of ^{90}Sr is shown in Fig. 4.1. The ^{90}Sr undergoes beta decay into yttrium-90 (^{90}Y) before beta decaying into zirconium-90 (^{90}Zr); the energy of the electrons is much higher in the second decay process. There is a finite

but extremely small probability that the decay processes emit gamma photons, this can be neglected and ^{90}Sr assumed to be a pure beta particle emitter for the purpose of this chapter.

^{90}Sr is often produced as a fission product of uranium-235. It has a particularly long half-life along with caesium-137 (^{137}Cs); both nearly 30 years [2]. The isotopes can be prominent in nuclear fallout from both weapon detonation and disasters at power stations such as Fukushima and Chernobyl [3, 4, 5]. The fallout can be carried over a large area, thousands of miles away from the original source by unpredictable weather systems. The primary concern with ^{90}Sr and ^{137}Cs over their long half-lives is that they easily accumulate in biological systems taking the place of calcium and potassium respectively [6, 7]. ^{90}Sr specifically is estimated at having a biological half-life of ~ 13 years [8]. This can be of a great concern if it enters the human food chain, via grazing animals and the soil. A prototype CVD grown, fluorographene, beta radiation detector is presented in this chapter which has the potential to be embedded in food packaging or as a wearable personal device; although a multimeter or power source would be required to measure the device. The single use nature due to the CF bonds breaking and the relatively low cost of producing CVD graphene would allow these devices to be disposable. To test the concept, devices are initially made using mechanically exfoliated flakes as will be discussed in the next sections.

4.2 Methods

4.2.1 Fabrication

Monolayer and few layer flakes of FG are obtained by mechanical exfoliation from fluorinated graphite. The graphite is fluorinated by exposing it to an atmosphere of XeF_2

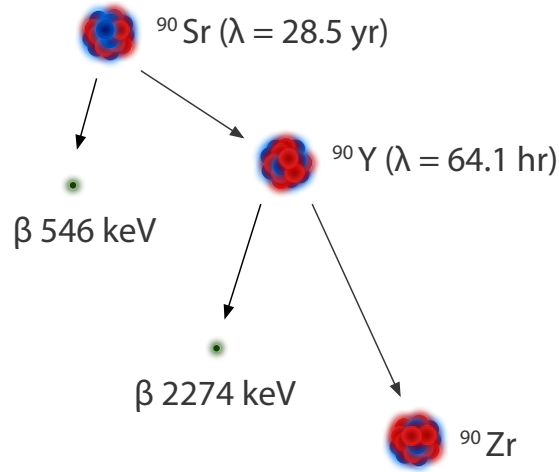


Figure 4.1: Decay Process for ^{90}Sr . The initial decay process into ^{90}Y has a half-life of $\lambda = 28.5$ years and produces almost exclusively β radiation with an energy of 546 keV. These beta processes do not have enough energy to leave the radioactive source; the second decay process into ^{90}Zr produces much higher energy β particles ~ 2.3 MeV. These particles have a high enough energy to leave the source and reach the sample.

at 120°C for 2 hours. At this temperature the XeF_2 decomposes into xenon and atomic fluorine. The fluorine can then disperse between the graphite layers and adsorb onto the surface. The two dimensional sp^2 hybridised structure of the graphene sheets is transformed into a three dimensional sp^3 hybridised structure. This method gives a homogeneous distribution of CF bonds [9, 10]. It is also less harsh than exposing the graphite to a F_2 gas which requires a high temperature and can introduce a number of defects into the material; thus making it difficult to obtaining monolayer flakes of a useful size. The amount of fluorine uptake by the graphite determines the dominant carrier transport mechanism and how developed the band gap becomes [9, 11]. FG ratio of $\text{CF}_{0.28}$ is chosen because of its initially highly insulating behaviour at room temperature. Few layer flakes of FG are identified by optical contrast, which is lower than for pristine graphene [9]. Electron beam lithography techniques are used to pat-

tern two-terminal transistor structures and Cr/Au electrodes are deposited by thermal evaporation with thicknesses 5 nm/50 nm respectively. A false colour scanning electron microscope image of a typical FG device is displayed in Fig. 4.2 (a) and the IV characteristics for an unexposed FG flake are shown in Fig. 4.2 (b). The IV curve is non-linear for ± 7 V with a flat region of no conduction around ± 5 V indicating the presence of a band gap in the material. The measured source-drain current is only ~ 150 pA for a bias voltage of 10 V; this insulating behaviour is typical of the fluorinated samples measured with this concentration of fluorine. The devices are then irradiated with a ^{90}Sr beta source placed such that the incident beam of β^- particles are perpendicular to the FG surface as shown in Fig. 4.2 (c). The exfoliated devices are held under a vacuum on the order of 10^{-2} mTorr and as a consequence the beam of β^- particles has to pass through a 5 mm thick glass window to reach the device, which is almost flush against window. The implications of this will be discussed the following sections. The structure of the fluorinated graphene before and after exposure is shown in Fig. 4.2 (d). The structure of the graphene is not damaged upon exposure to high energy electrons and the lattice returns to the sp^2 hybridised structure [1].

4.2.2 Radioactive source calibration

The activity of the ^{90}Sr source was calibrated using a Geiger counter with a halogen filled tube. Firstly the intensity drop in air is measured by recording the number of electrons impinging on the Geiger counter for different distances, Fig. 4.3 (a). The number of counts per second (cps) decays exponentially with increasing distance as the electrons are scattered off particles in the air. By placing the source directly against the Geiger counter window ~ 1600 cps are recorded. For the purpose of the analysis in Sec. 4.4, this is taken to be the number of electrons leaving the source each second. The

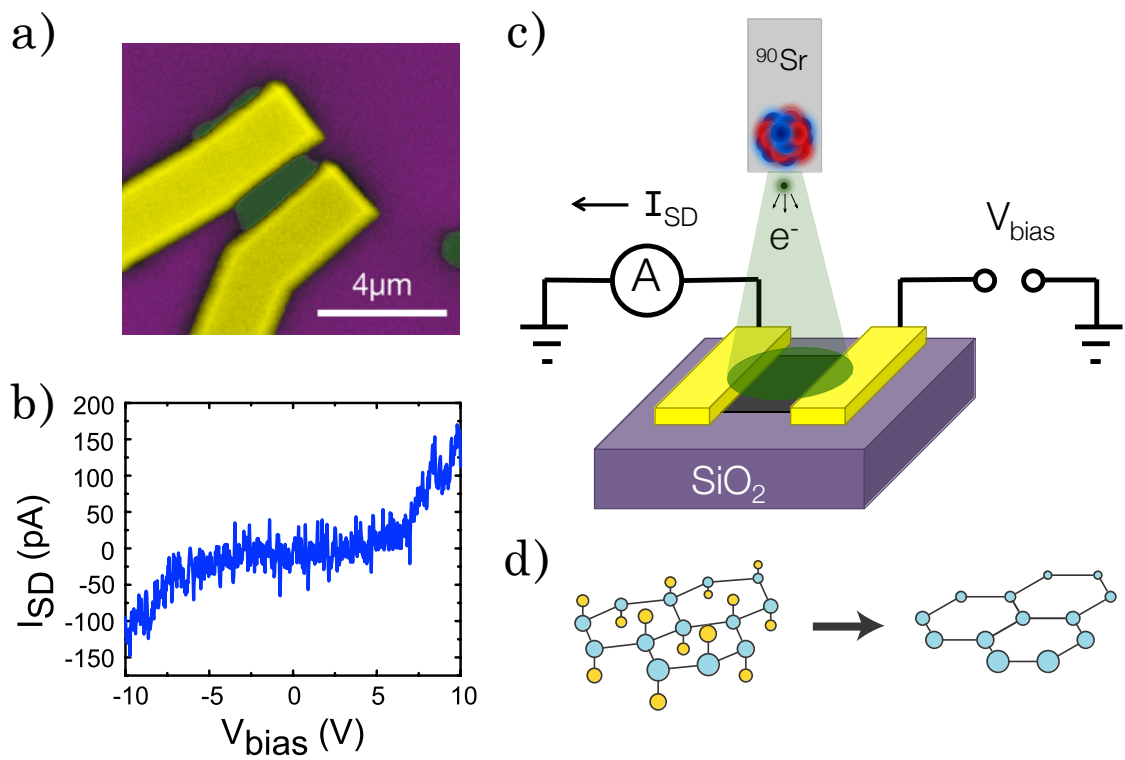


Figure 4.2: a) False colour SEM image of a typical device. Yellow represents the Cr/Au contacts, purple is the SiO₂ substrate and the green areas are FG. b) I_{SD} as a function of bias voltage V_{bias} for a FG flake unexposed to beta radiation. c) Schematic of the experimental setup, the ⁹⁰Sr beta source exposes the surface of the FG flake to β^- particles. d) The structure of fully fluorinated graphene, before (left) and after (right) exposure. The blue atoms represent carbon and the yellow atoms represent fluorine.

actual activity of the radioactive material inside the source is close to 74 kBq, however this accounts for the emissions in all directions radially. The radioactive material is encased in a lead shielding and has a small aperture of ~ 8 mm, covered by $50 \mu\text{m}$ of aluminium foil, this blocks lower energy emissions. These factors lead to the reduction in the number of electrons leaving the source. The second calibration is to determine the emission profile of the beam, Fig. 4.3 (b). In this case the source is kept stationary and the Geiger counter is moved around the source in a circular arc of radius 5 cm. The window of the Geiger counter has a diameter of 13 mm and would capture electrons that are emitted over a range of angles. In order to obtain more accurate results the window is shielded by a thick piece of aluminium (1 mm), with a 1.5 mm hole drilled in the centre. This results in a much sharper profile of the beam as only electrons directly incident are captured. The beam intensity drops to zero at angles greater than $\sim 60^\circ$ and can be fitted by a gaussian distribution. The beam profile is normalised so that it can be used to accurately determine the dose of electrons that reach the sample. Lastly the number of counts through a 5 mm thick piece of glass was measured to replicate the glass window on the measurement setup. This was found to reduce the total to 134 cps.

4.3 Results

To determine whether the effects of beta radiation are actually de-fluorinating the graphene, as opposed to damaging the flake, the effects of the exposure are first measured on a pristine graphene flake. Cr/Au electrodes are contacted to a monolayer flake using the same procedure outlined above for the FG flakes. Fig. 4.4 (a) compares the IV characteristics of a pristine device before exposure (blue curve) and after 12 hours (red curve). This amounts to a dose of $\sim 47 \text{ nC m}^{-2}$. The resistance of the flake does

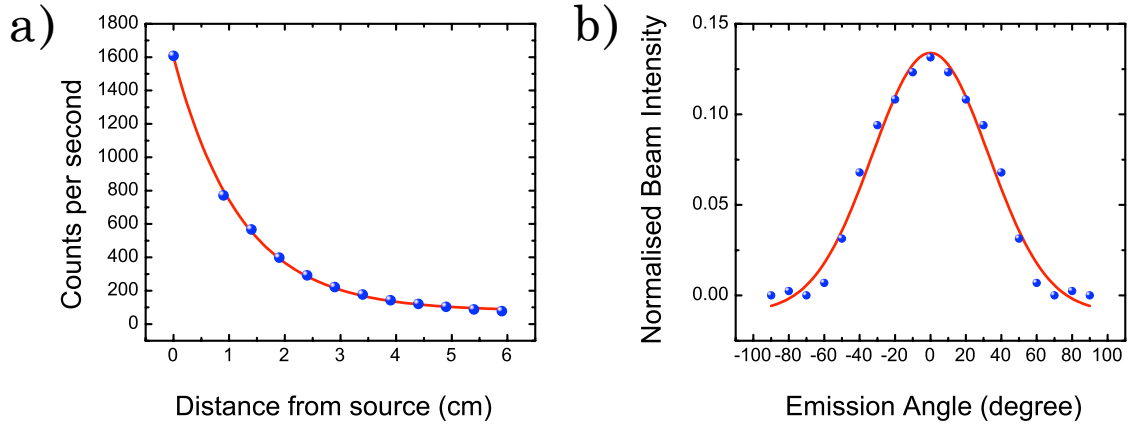


Figure 4.3: Calibration of the Strontium-90 source: **a)** The number of counts recorded on a Geiger counter as a function of distance in air. The counts decrease at an exponential rate with distance. **b)** The normalised profile of the emitted beam from the source, the maximum emission angle is $\sim 60^\circ$.

not noticeably change after exposure indicating that the graphene is not damaged from the beta radiation. The possibility that the beta radiation is damaging the contacts at the Cr/graphene interface can also be ruled out as the linearity of the IV curves are unchanged.

The beta radiation response of the FG device previously shown in Fig. 4.2 (b) is now considered. The sensitivity of the device to beta radiation is evident from Fig. 4.4 (b), which shows IV curves for its initial state (blue curve) and after 30 minutes of exposure (red curve). The resistance of FG flake drops by several GOhm, with the source-drain current at $10 V_{\text{bias}}$ increasing from ~ 150 pA to ~ 1.2 nA. Further time evolution of the IV curves up to 16 hours are displayed in Fig. 4.4 (c). As the exposure time increases, the resistance continues to drop and the curves display increasingly linear behaviour. Despite this improved conduction there still appears to be a region of disordered transport close to zero-bias even after 16 hours of exposure. This suggests

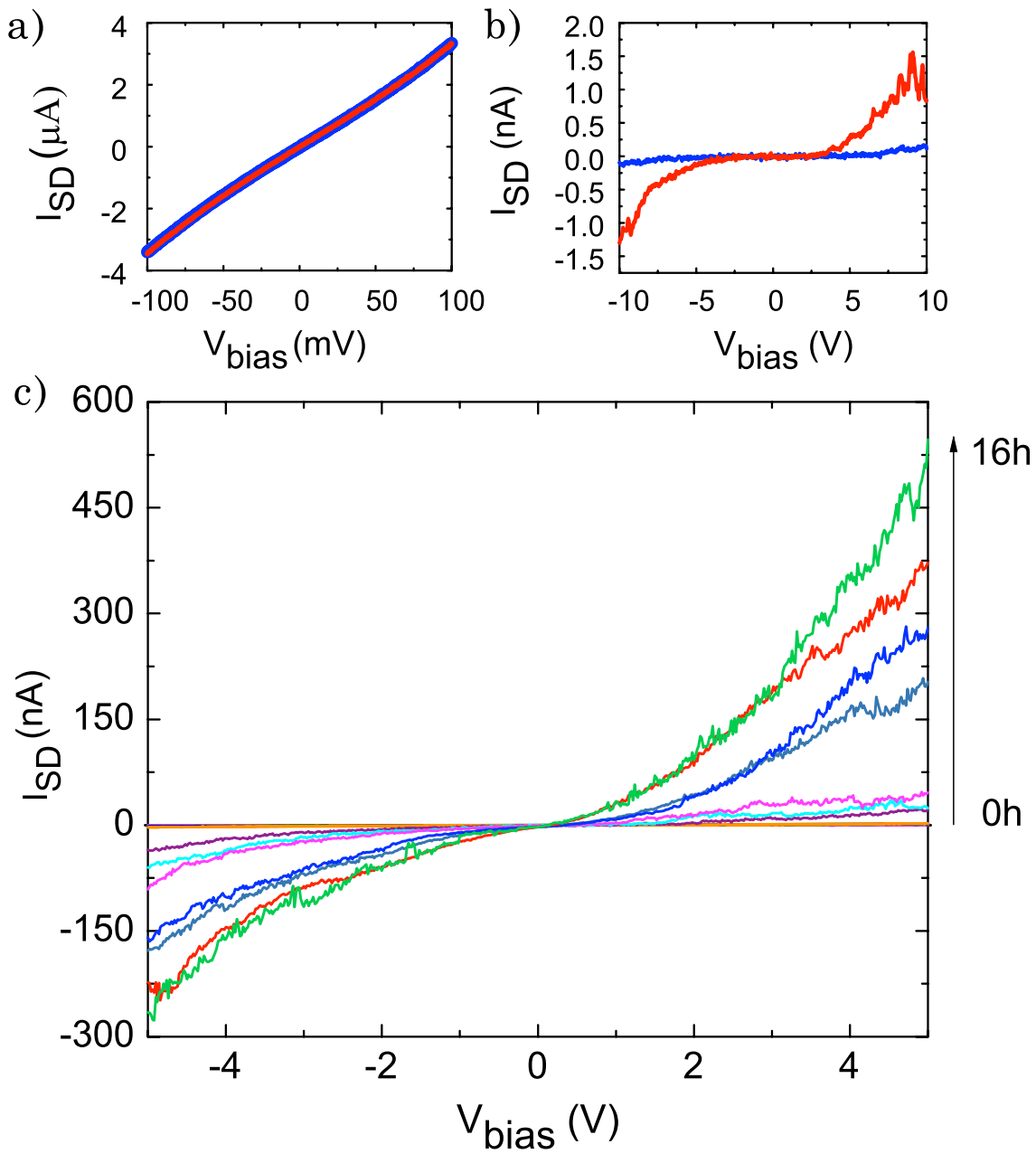


Figure 4.4: IV characteristics before (blue) and after (red) exposure to ^{90}Sr for: **a)** pristine graphene for 12 hours and **b)** FG for 30 minutes. **c)** The evolution of the IV curves for a FG device after exposure for 16 hours.

that there is still some fluorine content on the graphene surface and further exposure is required to fully defluorinate the flake. A similar response to the beta radiation is seen in other devices measured and it is worth noting that the change is permanent; the IV characteristic of the fluorinated graphene does not relax back to its initial unexposed state after the radiation source is removed.

4.4 Discussion and conclusions

The resistance of the device can be estimated from the high-bias (linear) regions of the IV curves in Fig. 4.4 (c). The resistances are plotted logarithmically as a function of exposure time/dose in Fig. 4.5. An estimate of the dose of electrons striking the surface of the FG can be made from the measured emissions from the source (134 cps); leading to a current density of $\sim 1.09 \times 10^{-12} \text{ Cm}^{-2}\text{s}^{-1}$. The equivalent electron beam dose bombarding the device in one hour is equal to $\sim 3.93 \text{ nC m}^{-2}$. By plotting device resistance on a log scale we can see that there are two different defluorination ‘regimes’. Initially the resistance drops sharply (yellow shaded region) from $20 \text{ G}\Omega$ to $2 \text{ G}\Omega$ in only one hour suggesting the device might be useful when a quick response is required. In the second regime (blue shaded region) the rate at which the resistance drops is slower but maintained over a long period of exposure. This suggests that the device can also be used to detect larger quantities of radiation. The inset to Fig. 4.5 is a log-log plot of the data from the higher dose regime scaled to the resistance per square for a device of dimensions $\sim 1 \mu\text{m} \times 1 \mu\text{m}$. A fit to the data reveals a dose of $1.01 \mu\text{C}/\text{m}^2$ required to reduce the resistance of the FG back to that of pristine graphene ($6.4 \text{ k}\Omega/\square$), or 257 hours. The density of CF bonds is $\sim 3 \times 10^{14} \text{ cm}^{-2}$ for $\text{CF}_{0.28}$ and the complete defluorination dose is equivalent to $\sim 6.25 \times 10^{16} \text{ electrons}/\text{cm}^2$. Therefore the probability of a single electron causing a CF bond to break is $\sim 5 \times 10^{-3}$. This corresponds

to a low number of electrons interacting with the device; indeed the maximum electron ionisation cross-section (giving the highest probability of breaking the CF bonds) is centred around 80 eV [12]. The energy of the electrons leaving the source is ~ 2.3 MeV which would have an extremely small cross-section; resulting in a low probability of the CF bond breaking. Therefore in order to break the CF bond, the energy of the β^- particles must be lowered. This could happen when they pass through the glass window for instance. A second more likely reason is interaction with the substrate, in this case SiO_2 . The electrons can be backscattered but only lose a small amount of energy; however secondary electrons emitted from inelastic scattering with the incident particles will have a much lower energy and a greater chance of breaking the CF bonds [1].

4.4.1 CVD fluorinated graphene device

Finally to highlight the possibility of upscaling the device for industrial applications we investigate a large area CVD grown device. The CVD graphene is grown on Cu foil in a two-zone hot walled furnace as described in [13]; it is then subjected to the same fluorination process as the mechanically exfoliated devices in an atmosphere of XeF_2 . The fluorinated CVD graphene is transferred to PET, a transparent and flexible substrate using the standard PMMA supported wet etching of Cu [14]. Contacts to the graphene were made directly using conductive silver paint and the device was exposed to the ^{90}Sr source in air (to simulate real world conditions); at a distance of 10 mm. At this distance the Geiger counter reported a count of 625 emissions per second. A photograph of the device is shown in Fig. 4.6 (a) highlighting the flexibility of the substrate. Fig. 4.6 (b) shows the resistance of the device decreasing with prolonged exposure time. The device was exposed for 130 minutes corresponding to a dose of

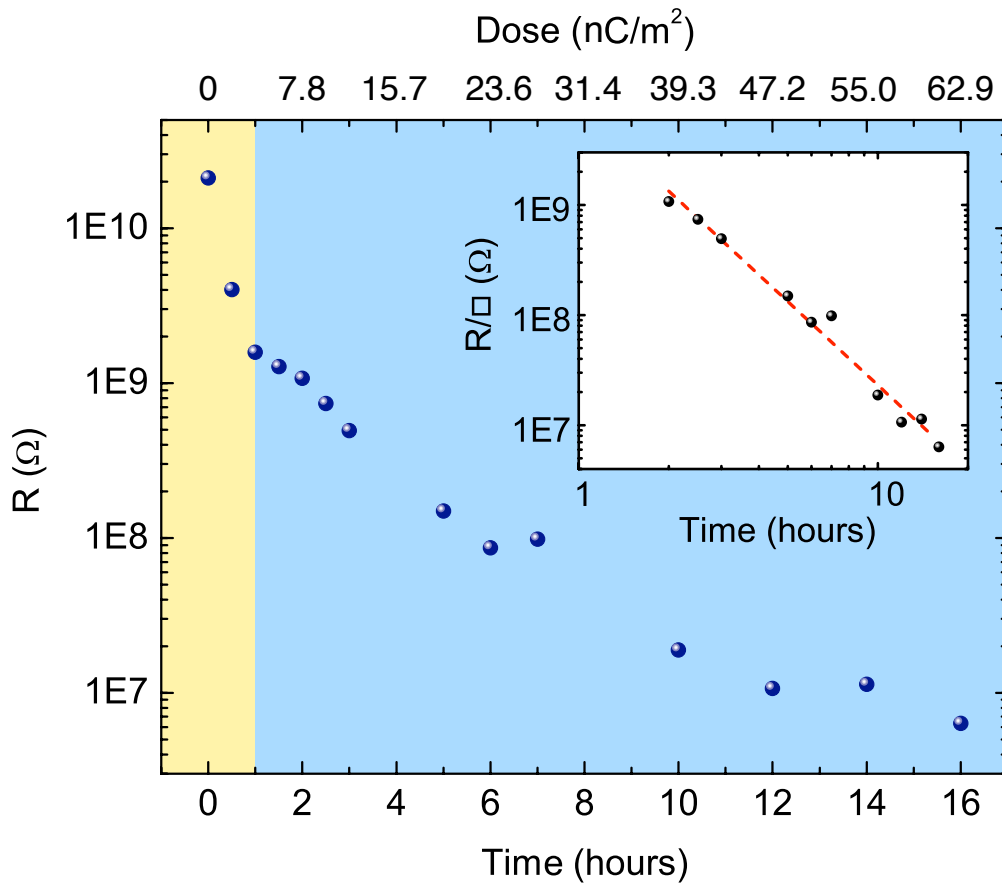


Figure 4.5: The estimated resistance of the sample plotted against the exposure time/dose. The shaded regions indicate regimes with different defluorination rates (yellow higher/blue lower). Inset: A log-log plot of the high dose regime. The dose required to fully defluorinate the graphene is extracted from the fit.

9.9 nC/m².

We now determine the sensitivity of the CVD device and its real world performance by considering its sensitivity as a function of equivalent absorbed radiation dose. Ionising radiation dose is quantified by the total amount of energy absorbed per kilogram of matter, the SI unit being the Gray (Gy) with units of (J/Kg). The issue is further complicated by types of ionising radiation and the type of tissue that is absorbing the radiation. The effective absorbed dose includes a dimensionless weighting factor for both the type of radiation absorbed and the affected tissues. The SI unit of effective dose is the Sievert (Sv) which also has units of (J/Kg) and is given by the following equation [15]:

$$E = \sum_T W_T \sum_R W_R \cdot \bar{D}_{T,R}$$

Here W_T is the tissue weighting factor, W_R is the radiation type weighting factor and $\bar{D}_{T,R}$ is the average absorbed dose in tissue type T with radiation type R. In the case of beta radiation, W_R is 1 and to simplify the discussion we will consider uniform whole body absorption, in which case the tissue weighting factor also sums to 1. The ⁹⁰Sr source undergoes β^- decay into ⁹⁰Y with an average emission energy of 0.546 MeV, electrons with this energy cannot pass through the aluminium shielding of the source. The subsequent β^- decay of ⁹⁰Y produces electrons with an average emission energy of 2.28 MeV, knowing the number of electrons striking the sample per second (508) and taking the average weight of a person to be 75 kg, an estimate of the effective dose is found to be 10 nSv/hr. The sheet resistance of the CVD device drops by $\sim 35 \text{ k}\Omega/\square$ in two hours corresponding to a sensitivity of $1750 \text{ }\Omega/\square$ per nSv. A nano sievert is a small quantity of radiation and a resistance change of $1750 \text{ }\Omega$ is easily detectable. The CVD device while displaying a high sensitivity to ionising radiation; is not as sensitive

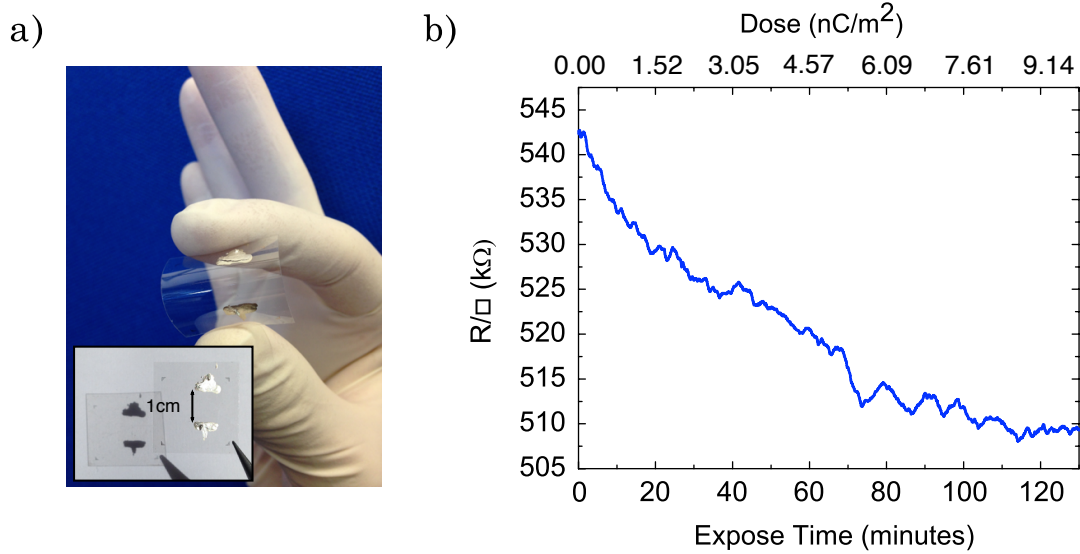


Figure 4.6: CVD grown fluorinated graphene with dimensions $L = 1 \text{ cm} \times W = 0.85 \text{ cm}$: **a)** Photograph of the device on a flexible transparent substrate. **b)** Resistance as a function of exposure time/dose.

as the exfoliated flakes on SiO_2 . This could be explained by the uniformity of the fluorine coverages. The CVD device is much more conductive suggesting there is a pathway for the current to flow easily through the sheet. A Raman study could give some insight into the uniformity of the CVD device.

4.5 Conclusions

The principle of using fluorinated graphene as a beta radiation detector has been successfully demonstrated. Devices made from mechanically exfoliated fluorinated graphene on SiO_2 substrates show a rapid decrease in resistance upon initial exposure to beta radiation; resistance of the device decreases 2 orders of magnitude from 20 $G\Omega$ to 2 $G\Omega$ in only 2 hours. The process causing the decrease in resistance is attributed to a breaking of the carbon-fluorine bonds which reduces the sp^3 hybridised

structure of the FG back into the sp^2 hybridised structure of pristine graphene. The exact process leading to the bond breaking is unknown; the ionising cross-section of the CF bonds has a maximum for electrons of energy 80 eV. The energy of the β^- particles leaving the source is much greater than this suggesting that the incident particles have a extremely small probability of interacting with the bond. Possible explanations for the bond breaking include the β^- particle having lower energy after they have passed through the glass window to the substrate or from secondary electrons after interaction with the SiO_2 substrate. The possibility that the beta radiation is damaging the graphene is ruled out by exposing a pristine graphene device. The resistance of the pristine graphene does not change even after exposure for 12 hours. There is the potential to scale up these devices using CVD grown graphene in conjunction with transparent flexible substrates. Such a device could find a use as a personal dosimeter or embedded within food packaging to confirm the safety product.

Bibliography

- [1] F. Withers, T. H. Bointon, M. Dubois, S. Russo, and M. F. Craciun, *Nano Letters* **11**, 3912 (2011).
- [2] LBNL, LBNL Isotopes Project, <http://ie.lbl.gov/toi/> (Accessed: 14/02/14).
- [3] H. Beck, A. Bouville, B. Moroz, and S. Simon, *Health Phys.* **99**, 124 (2010).
- [4] A. Aarkrog, *Journal of Environmental Radioactivity* **6**, 151 (1988).
- [5] W. F. Libby, *Science* **123**, 657 (1956).
- [6] P. S. Chen, A. R. Terepka, and H. C. Hodge, *Annual Review of Pharmacology* **1**, 369 (1961).
- [7] J. Baarli, K. Madshus, K. Liden, and R. C. McCall, *Nature* **191**, 436 (1961).
- [8] P. Froidevaux, F. Bochud, and M. Haldimann, *Chemosphere* **80**, 519 (2010).
- [9] F. Withers, S. Russo, M. Dubois, and M. Craciun, *Nanoscale Res. Lett.* **6**, 526 (2011).
- [10] W. Zhang, L. Spinelle, M. Dubois, K. Guérin, H. Kharbache, F. Masin, A. Kharitonov, A. Hamwi, J. Brunet, C. Varenne, et al., *Journal of Fluorine Chemistry* **131**, 676 (2010).

-
- [11] F. Withers, M. Dubois, and A. K. Savchenko, *Phys. Rev. B* **82**, 073403 (2010).
- [12] M. Bart, P. W. Harland, J. E. Hudson, and C. Vallance, *Phys. Chem. Chem. Phys.* **3** (2001).
- [13] X. Li, W. Cai, J. An, S. Kim, J. Nah, D. Yang, R. Piner, A. Velamakanni, I. Jung, E. Tutuc, et al., *Science* **324**, 1312 (2009).
- [14] X. Li, Y. Zhu, W. Cai, M. Borysiak, B. Han, D. Chen, R. D. Piner, L. Colombo, and R. S. Ruoff, *Nano Letters* **9**, 4359 (2009).
- [15] ICRP, *ICRP Publication* **103** (2007).

Chapter 5

Towards suspended MoRe Josephson junctions with a graphene weak link

5.1 Introduction

In this thesis the main superconducting metal used is an alloy of molybdenum-rhenium (MoRe) in a 50:50 ratio by weight. This chapter will first discuss the optimal deposition parameters for sputtering MoRe (Sec. 5.2) and then the superconducting properties of MoRe will be characterised (Sec. 5.3). It is found to have a relatively high critical transition temperature and ability to sustain large super currents. In Sec. 5.4 an important trait of the material is discovered. MoRe displays a resistance to hydrofluoric acid (HF), which is a commonly used oxide etchant in the fabrication of micro and nano-mechanical devices. Nearly all superconducting metals are etched by HF so this makes MoRe an attractive option for use with suspended graphene as extremely high mobilities can be obtained in this way [1]. In Sec. 5.5 a supported MoRe Josephson junction with graphene as a weak link will be demonstrated to show that the material is compatible with graphene; finally a brief discussion on some possible experiments that could make use of the suspended Josephson junctions.

5.2 Deposition of superconducting metals

MoRe is deposited onto a Si/SiO₂ substrate by a sputter deposition system with additional e-beam evaporation capabilities for evaporating interface metals. The sputtering conditions and substrate preparation can play a hugely important role. It determines whether the metal adheres to the substrate and the quality of the contact interface with graphene. In this section some of the more important aspects are highlighted.

An example of a failed deposition is shown in Fig. 5.1 (a). The metallic film appears to have grown non-uniformly and in small domains on the regions of PMMA. It is possible to make out the shape of the contact patterned regions where the metal

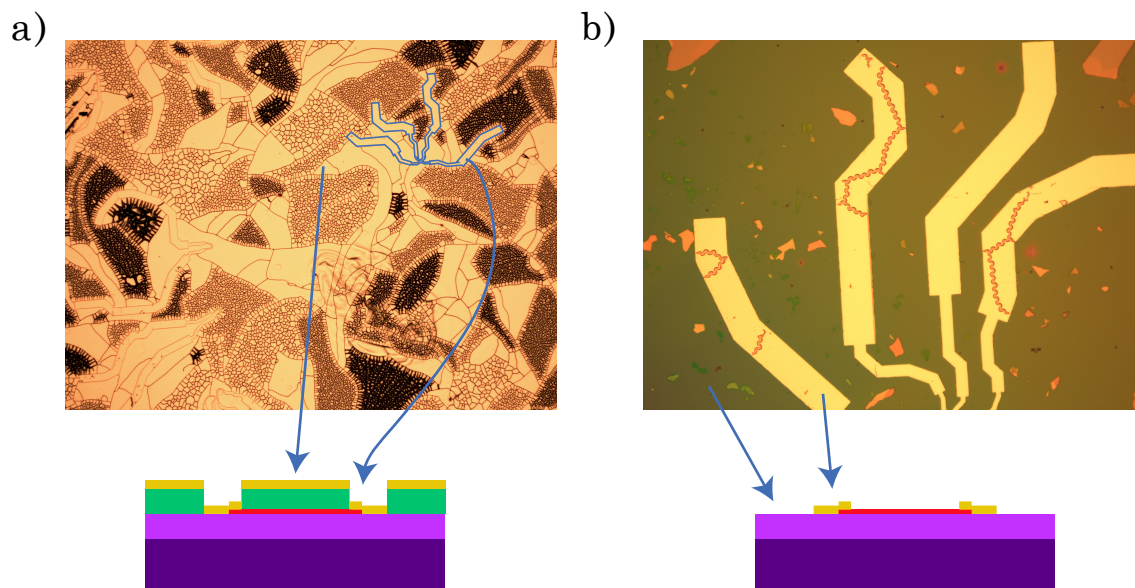


Figure 5.1: a) A 100 nm sputter deposition of MoRe with a 5 nm Pd sticking layer; 300 W power and 3 mTorr gas pressure. The blue outline corresponds to a region where e-beam contacts have been defined. b) Close up of the MoRe leads after lift-off in acetone showing defects. Below the images are side on representations of the current stage in the lithography process.

is directly deposited to the SiO_2 , one such instance is outlined in blue. These look well formed but after lift-off deformations to the metal are also apparent, as seen in Fig. 5.1 (b). A systematic approach was taken to try and find the root cause of the domain formation: the sputtering power was varied from 30 W to 300 W; ambient gas pressure from 3 mTorr to 8 mTorr; different interface metals were used such as Pd, Ti or MoRe directly. In each case the metals are evaporated onto a film of PMMA, which is spun at a high rate (7000 rpm) to achieve a uniform film. The domains formed in each configuration, except for the direct sputtering of MoRe. This suggests there is some strain induced in the MoRe film due to the adhesion layer. The interface metals are thermally evaporated by heating from an incident beam of electrons with energy 10 keV. The rate of deposition is easily controllable by adjusting the current, when the rate of deposition is increased from 0.5 \AA s^{-1} to 1 \AA s^{-1} a uniform sheet of MoRe can be deposited on top of both Ti and Pd. This suggests that a higher deposition rate may lead to a more uniform film of Ti and Pd. In all cases a 5 nm layer of the interface material was deposited. Examples of successful depositions can be seen in Fig. 5.2 (a, inset) and Fig. 5.6 (a).

5.3 Characterisation of MoRe

5.3.1 Thin channels

To characterise MoRe, Hall-bar shaped structures were deposited using e-beam lithography. An optical image of a typical device can be seen in Fig. 5.2 (a, inset). 120 nm of MoRe is sputtered and the width of the channel is 200 nm. These sizes were chosen as they are on the order of the smallest size contacts that will be employed for the graphene based devices; this will test if they can still become superconducting. The

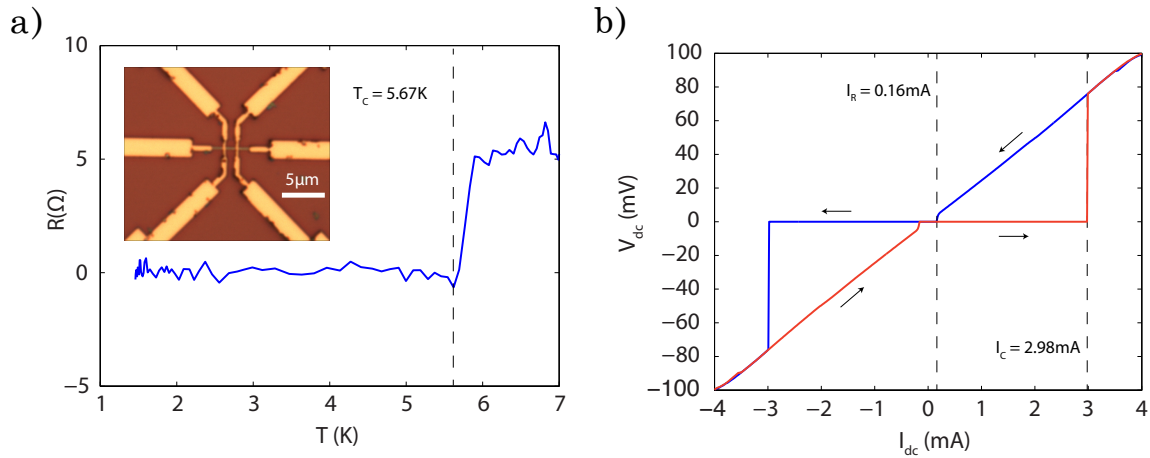


Figure 5.2: Characterisation of a 200 nm wide channel of MoRe: **a)** The temperature dependence of the resistance measured upon cooling the device. The superconducting transition temperature $T_C = 5.67$ K. The inset is an optical image of the channel after successful MoRe deposition. **b)** The VI characteristics of the channel at 250 mK, arrows indicate the direction of the sweeps. The critical current $I_C = 2.98$ mA and the re-trapping current $I_R = 0.16$ mA.

sample was cooled to ~ 250 mK and the resistance of the channel was measured using a low frequency lock-in technique. Fig. 5.2 (a) displays the temperature dependence of the resistance for $T < 7$ K, the critical temperature where the resistance of the device drops to 0Ω is identified as $T_C \sim 5.7$ K. This temperature is high enough that experiments can be performed even in simple non-vacuum probes, directly in the liquid ^4He . The super-current carrying capabilities of the channel are highlighted in Fig. 5.2 (b), a current is passed through the source and drain contacts and the voltage drop measured across the length of the channel. The current is swept over the range of ± 4 mA and there is a large hysteresis between the up and down sweeps; the critical current $I_C = 2.98$ mA and the re-trapping current $I_R = 0.16$ mA.

The narrow channel is able to sustain a large super-current which is related to the expulsion of all magnetic flux up to a high critical magnetic field intensity H_C . To learn more about H_C the device is subjected to a perpendicularly applied magnetic

field up to $B = 10$ T. Superconductors can be considered a perfect diamagnet except for a small penetration depth at the surface so for the following discussion we will assume that $H_C = B_C$. Fig. 5.3 (a) and (b) are colour plots of the voltage drop across the device as a function of the magnetic field and source drain current, down and up sweeps respectively. I_C quickly diminishes with increasing magnetic field but persists up to ~ 8 T. To highlight the critical current value the same data is plotted in Fig. 5.3 (c) and (d) with any positive voltage coloured red, any negative voltage coloured blue, and green when the device shows zero resistance. To get a more accurate value for the critical field a small AC excitation of 10 nA is applied and the zero-bias resistance of the sample is measured as a function of magnetic field, Fig. 5.3 (e). The device begins to enter the normal above after 8 T; also for comparison the extracted values of I_C from Fig. 5.3 (d) are plotted on top. The reduction of I_C to zero corresponds to the increase in the resistance of the channel. From the BCS equations the zero temperature critical field value can be estimated [2]:

$$H_C(T) = H_C(0) \left[1 - \left(\frac{T}{T_C} \right)^2 \right].$$

The estimated temperature dependence of $H_C(T)$ is calculated in Fig. 5.3 (e). To summarise, the MoRe channel displays an ability to carry large super currents of up to 2.98 mA and has a critical field of ~ 8 T. This is also while only having a channel width of 200 nm and means that the material can be used in applications where restricted contact size is important; such as superconducting-nanowire single-photon detectors [3, 4].

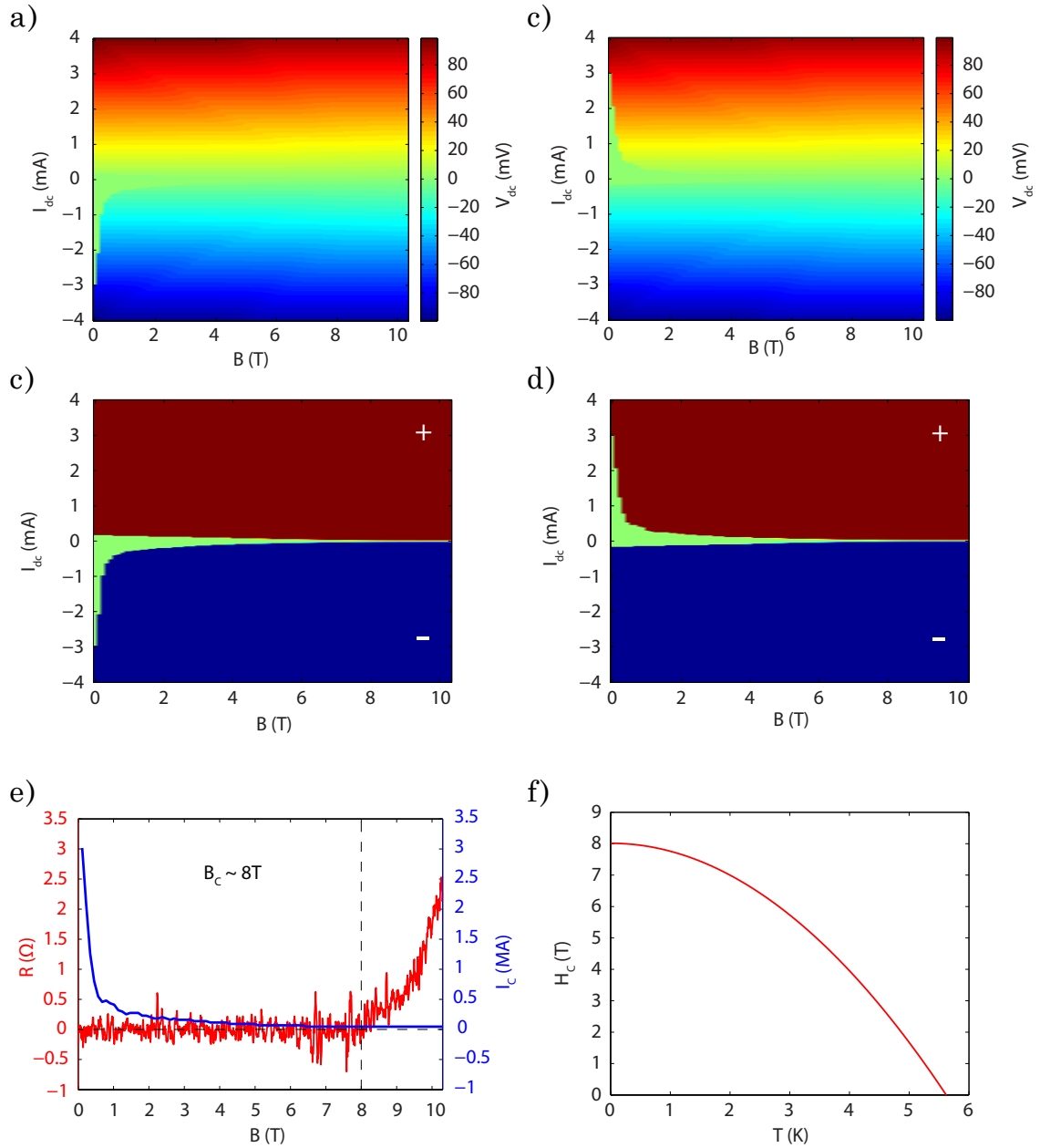


Figure 5.3: Magnetic field dependence of the MoRe Channel: **a)** Downswep and **b)** upswep colour plots of the voltage drop along the length of the channel as a function of source-drain current and magnetic field, $T = 250$ mK. **c)** and **d)** are the same data as above but plotted in a signed binary colour scheme where positive values are red, zero values are green and negative values are blue. In the green regions the resistance of the device is 0Ω . **e)** Left axis: The zero-bias resistance of the channel for increasing magnetic field. The critical field $B_C \sim 8$ T. Right axis: The extracted values of I_C from the upswep measurements. **f)** The computed values of the critical field as a function of temperature.

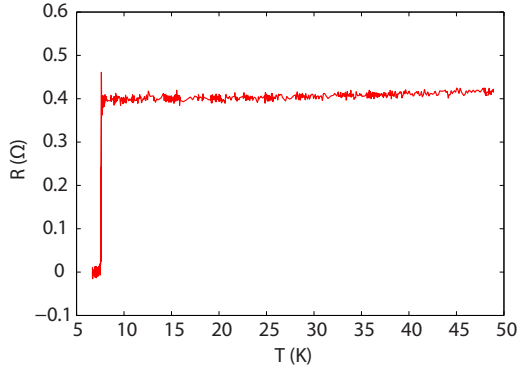


Figure 5.4: Temperature dependence of the resistance for a $250 \mu\text{m} \times 250 \mu\text{m}$ MoRe square with thickness 120 nm. The transition temperature where the resistance drops to 0Ω is $\sim 7.5 \text{ K}$.

5.3.2 Bulk material

To obtain a more accurate result for the transition temperature of the material a large area was deposited with dimensions $250 \mu\text{m} \times 250 \mu\text{m}$ and thickness 120 nm. Fig. 5.4 shows a transition temperature of $\sim 7.5 \text{ K}$ in support of results in [5]. An estimate of the zero temperature energy gap Δ_0 can be obtained from the BCS equation [2]:

$$\Delta_0 = 1.76k_B T_C, \quad (5.1)$$

Δ_0 is found to be 1.14 meV, this value will be used in a later section.

5.4 Resistance to hydrofluoric acid

In chapter 3.1, methods of suspending 2D materials were discussed. If MoRe is able to withstand harsh hydrofluoric acid etching then it opens up the possibility of creating Josephson junctions with a suspended graphene weak link. This could be utilised to explore the vibrational properties of the system while in the superconducting regime. Other benefits include the option to current anneal the device and improve the charge carrier mobility; potentially enhancing the Josephson super current through the graphene. To test the MoRe's resistance to HF, devices with the same Hall-bar

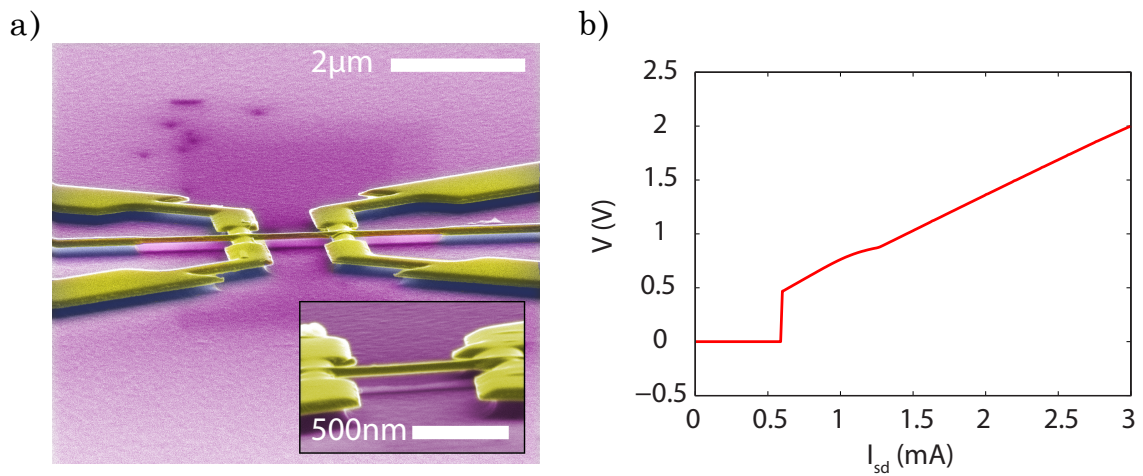


Figure 5.5: a) A false colour SEM image of a MoRe channel after HF etching. b) Voltage-current characteristics for the etched MoRe channel.

configuration as in Sec. 5.3 are placed in HF for 2.5 minutes to etch away 200 nm of SiO_2 . Fig. 5.5 (a) is a false colour SEM image of one of the devices after the etching process, the MoRe remains fully intact and the area of SiO_2 underneath the channel is completely etched. Electrical transport measurements confirm that the MoRe retains the ability to carry a super current after the etching, Fig 5.5 (b). Note that the device that was etched is not the same device as in Sec. 5.3 and therefore has a different critical current value of $I_C = 0.58$ mA. The edges of thin channels of MoRe have been shown to be contaminated by remnants of the lithography processes [5]. This could be one reason for the lower I_C value. It has been shown that by annealing the thin channel the contaminants can be removed and the superconducting properties of the material improved.

5.5 MoRe Josephson junctions with a graphene weak link

Knowing that MoRe can withstand HF etching the next step is to determine if the material is compatible with graphene and able to produce a working Josephson junction. Fig. 5.6 (a) shows an optical microscope image of a typical device. A graphene flake is contacted up to 5 nm/120 nm of Ti/MoRe respectively with varying junction lengths ranging from 100 nm, 150 nm to 200 nm. The devices were measured in a dilution refrigerator reaching a base temperature as low as 30 mK. Attached to the electrical inputs of the insert are room temperature RC filters; there are also low temperature copper powder filters on each of the electrical lines. They are cooled to the helium bath temperature, greatly reducing input noise to the junction. The $R(V_g)$ dependence for the 200 nm device is shown in Fig. 5.6 (b). The fact that the resistance can be modulated with the back gate is evidence that the junction is not shorted, despite not being able to see clearly from optical images. The graphene does not appear to be significantly doped as the charge neutrality point is close to $V_g = 0$ V; however the mobility of the graphene is low, estimated to be $\sim 130 \text{ cm}^2 \text{ V}^{-1} \text{ s}^{-1}$ from the linear region close to $V_g = 0$ V. Fig. 5.6 (c) shows VI characteristics for different gate voltages, the blue curve at $V_g = 0$ V is almost completely linear. The differential resistance as plotted in Fig. 5.6 (d) reveals that the junction does not carry a Josephson super current for low biases but there is a dip in the resistance that suggests proximity induced superconductivity is attempting to form. The lack of super current could be due to the Fermi level in the graphene being close to the neutrality point, where the density of states vanishes. At low energies near the Fermi level the Andreev reflection process at the normal-superconducting interface is of a specular nature rather than the usual

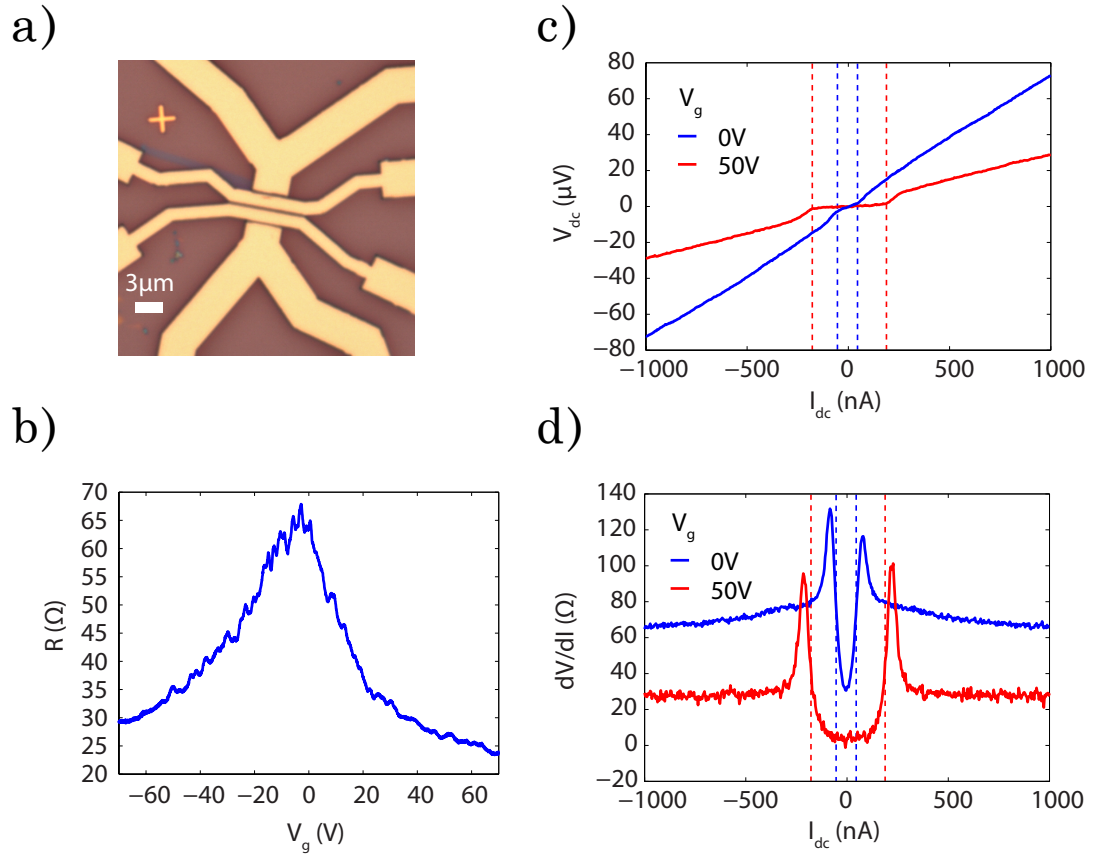


Figure 5.6: Characterisation of a Ti/MoRe (5 nm/120 nm) Josephson junction with graphene weak link of channel length 200 nm: **a)** An optical image of the device with multiple channel lengths (100, 150 & 200 nm). **b)** The gate voltage dependence of the resistance of the at ~ 270 mK. The graphene is electron doped to only a few volts. **c)** The VI characteristics at a gate voltage of 0 V (blue curve) and 50 V (red curve) at $T = 30$ mK. **d)** The differential resistance as a function of the source drain current. The dashed lines are a guide to match the features with the VI curve.

retro-reflection [6]. In charge neutral graphene there exists puddles of inhomogeneous doping [7]; de-phasing of the Cooper pairs at the boundaries between the puddles could inhibit this process [8]. To see if the proximity effect can be induced the carrier density of the graphene is increased by means of a gate voltage. The red curve in Fig. 5.6 (c) corresponds to $V_g = 50$ V. It is clear from the VI characteristics that for current biases up to $\sim I_{SD} = 200$ nA the graphene carries a proximity induced super current. The differential resistance in Fig. 5.6 (d) shows that the resistance drops to almost zero; the finite resistance measured here could be due to voltage drop at the contacts due to less than 100% transparency at the interface. There is a sharp peak feature that appears when the graphene weak link is no longer able to carry a full super current; it is more pronounced at $V_g = 50$ V than $V_g = 0$ V. A potential origin for the peaks is discussed later in this section.

The temperature dependence of the differential resistance is plotted in Fig. 5.7 (a) for temperatures from 280 mK to 13 K. The current is swept over a larger bias range than the measurements at 30 mK; this sees the appearance of extra features which are labeled in the figure. There is a peak that appears around low current biases and at low T (i), the peak vanishes above 1 K and becomes a trough. The lowest resistance of the device is found at this trough and the value of resistance increases gradually with T . Either side of the peak there are two dips (ii) which also disappear above 1 K. There are two shoulders (iii & iv) which are gradually smoothed out as the temperature increases. The shoulder at (iii) shifts in towards the centre with increasing T whereas the shoulder at (iv) lowers in resistance and moves away from the centre with increasing T before disappearing completely; this shoulder most likely corresponds to the superconducting-normal transition in the leads. Fig. 5.7 (b) shows the differential resistance of the sample as a function of a bias voltage rather than

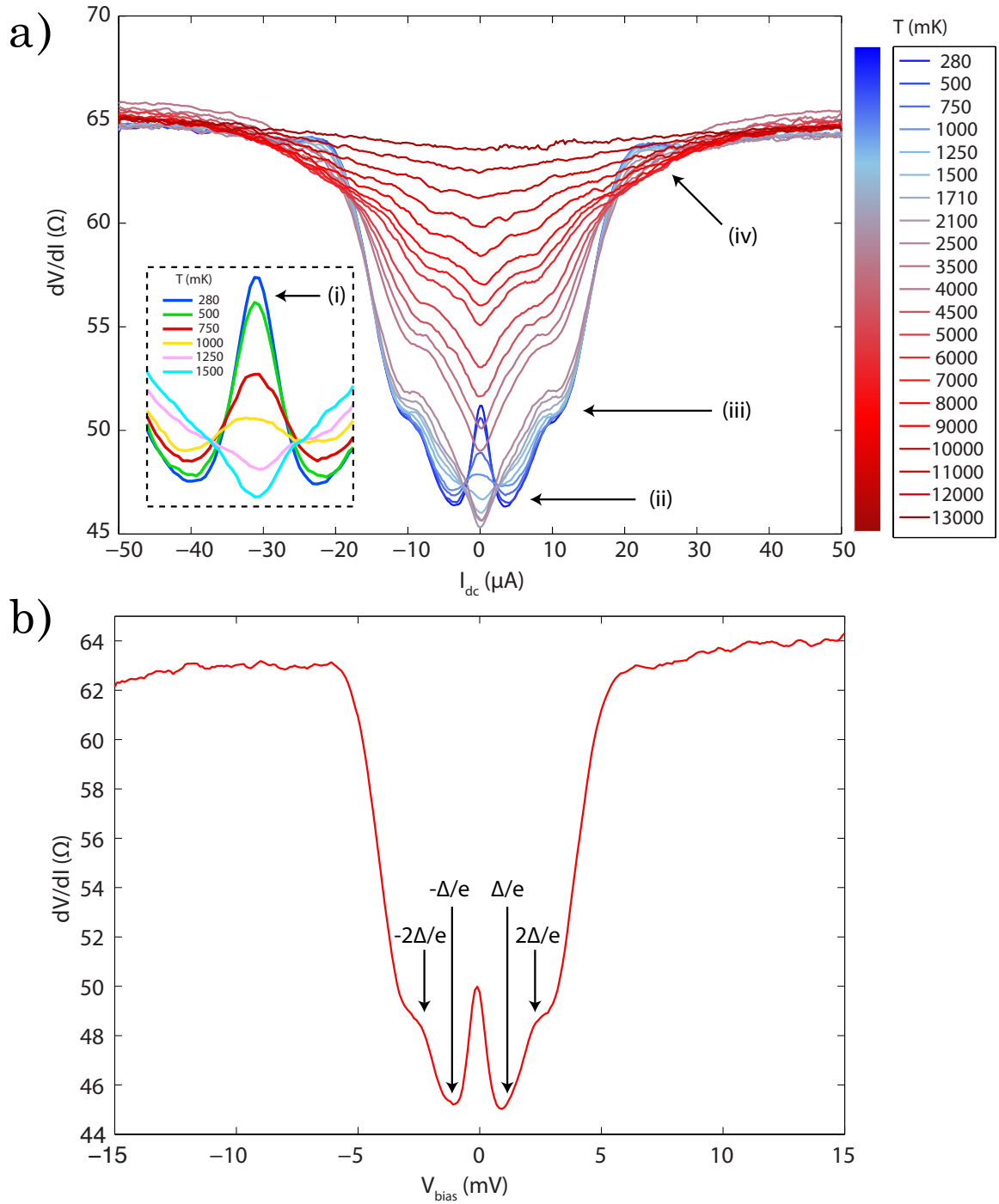


Figure 5.7: a) Temperature dependence of the differential resistance in the bias range $\pm 50 \mu A$. T increases from 280 mK (blue) to 13 K (red). Features of interest are labeled with Roman numerals; the inset is a zoom showing the evolution of the low bias peak that appears for low T . b) The differential resistance as a function of bias voltage for $T = 280$ mK, labelled are the BCS predicted values of the superconducting gap Δ for MoRe. All plots in this figure were taken at $V_g = 0$.

current for 280 mK. The superconducting energy gap of the bulk MoRe at $T = 0$ K as estimated in Sec. 5.3.2 was found to be $\Delta_0 = 1.14$ meV. The positions of Δ (ii) and 2Δ (iii) are marked on the plot. Drops in the resistance at these points are signatures of multiple Andreev reflections [9, 10]; where a bound state between the Cooper pairs of the superconductor and electrons in the normal metal are formed and the conductance increases. The position of the shoulder at (iii) moving towards zero with increasing temperature is consistent with the size of the gap decreasing with T as predicted by BCS theory [2]:

$$\Delta(T) = 1.74\Delta_0 \left(1 - \frac{T}{T_C}\right)^{1/2}, \quad (5.2)$$

this is valid as T approaches T_C . The peak at (i) which is later seen to spit into two parts upon lowering the temperature to 30 mK could be indicative of a sub gap feature.

5.6 Conclusions

In this chapter the ideal growth conditions for MoRe were presented and the subsequent characterisation revealed that MoRe may prove to be an interesting superconductor to use in conjunction with graphene. It has shown a high critical temperature above the boiling point of ^4He while also being able to carry a large super current up to magnetic fields of ~ 8 T. These features could allow the possibility to explore a system where superconductivity and the quantum Hall effect coexist. Previous work on such a system with graphene used niobium for contacts which have a critical field of ~ 4 T [8, 11]; so it may be possible to resolve additional Landau levels with MoRe. A resistance to hydrofluoric acid also presents opportunities to explore new systems. The

mechanical properties of graphene have never been explored in the superconducting regime. Suspending devices for Josephson junctions and superconducting quantum interference devices also have the benefit of being able to anneal the graphene to improve their performance. On supported devices a proximity induced super current was measured in a MoRe-Graphene-MoRe Josephson junction of up to 200 nA. However it required a temperature of $T = 30$ mK and a gate voltage of 50 V to shift the Fermi level away from the neutrality point. The fully developed super current was not seen in charge neutral graphene and at higher temperatures the resistance of the device actually increased around zero bias. These factors suggest that the interface between the graphene and the superconductor are not fully transparent and so further work should look into improving this interface. This could be done by investigating the choice of interface metals between the MoRe and the graphene and their thickness; or by devising a method of cleaning the graphene sheet directly before deposition of metals to remove lithography contaminants.

Bibliography

- [1] K. Bolotin, K. Sikes, Z. Jiang, M. Klima, G. Fudenberg, J. Hone, P. Kim, and H. Stormer, *Solid State Communications* **146**, 351 (2008).
- [2] M. Tinkham, *Introduction to Superconductivity* (McGraw-Hill, New York, 1996).
- [3] A. D. Semenov, G. N. Gol'tsman, and A. A. Korneev, *Physica C: Superconductivity* **351**, 349 (2001).
- [4] G. N. Gol'tsman, O. Okunev, G. Chulkova, A. Lipatov, A. S. K. Smirnov, B. Voronov, and A. Dzardanov, *Appl. Phys. Lett.* **79** (2001).
- [5] M. Aziz, D. C. Hudson, and S. Russo, *Applied Physics Letters* **104**, (2014).
- [6] C. W. J. Beenakker, *Phys. Rev. Lett.* **97**, 067007 (2006).
- [7] J. Martin, N. Akerman, G. Ulbricht, T. Lohmann, J. H. Smet, K. von Klitzing, and A. Yacoby, *Nat Phys* **4**, 144 (2008).
- [8] K. Komatsu, C. Li, S. Autier-Laurent, H. Bouchiat, and S. Guéron, *Phys. Rev. B* **86**, 115412 (2012).
- [9] X. Du, I. Skachko, and E. Y. Andrei, *Phys. Rev. B* **77**, 184507 (2008).

- [10] A. Shailos, W. Nativel, A. Kasumov, C. Collet, M. Ferrier, S. Guéron, R. Deblock, and H. Bouchiat, *EPL (Europhysics Letters)* **79**, 57008 (2007).
- [11] P. Rickhaus, M. Weiss, L. Marot, and C. Schönenberger, *Nano Letters* **12**, 1942 (2012).

Chapter 6

The nature of electronic transport in WS_2 and MoS_2

Note: The WS_2 portion of this chapter is based on the paper by F. Withers, T. H. Bointon, D. C. Hudson, M. F. Craciun and S. Russo, *Scientific Reports* **4**, 4967 (2014) of which the author of this thesis is a co-author. Contributions were made to the fabrication and measurement of devices, some of the figures in this chapter have been modified from the paper. Since then a similar analysis has been performed by the author on MoS_2 suspended devices.

6.1 Introduction

In this chapter WS_2 and MoS_2 transistors are fabricated in order to study the intrinsic electrical properties of the materials. Current research has mainly been focused on MoS_2 and has shown that on SiO_2 substrates; these devices exhibit low mobilities in the range $0.01 - 10 \text{ cm}^2\text{V}^{-1}\text{s}^{-1}$ [1, 2, 3]. It has been shown that the mobility can be improved by encapsulating the device in a high- κ dielectric, this has the effect of screening the charge traps in the SiO_2 substrate [4]. Ultimately though the upper limit to the room temperature mobility has been theoretically calculated to be phonon limited to $410 \text{ cm}^2\text{V}^{-1}\text{s}^{-1}$ [5]. The low mobilities observed in MoS_2 have thus far been attributed to defect states in the SiO_2 [1]. Characterisation of these materials in a low defect environment will therefore reveal the intrinsic properties of the materials. High mobilities have been obtained in graphene by either freely suspending the graphene flake [6] or by transferring the flake on top of hexagonal boron nitride (h-BN) [7]. h-BN is a good choice of substrate as it is atomically flat and has a low concentration of impurities and defects that can act as charge scatterers [8]. In this chapter WS_2 and MoS_2 are studied in low defect environments. It shows that the defects and low mobilities observed are intrinsic to the materials regardless of substrate choice. In Sec. 6.2 WS_2 transistors are fabricated on a h-BN substrate and in Sec. 6.3 MoS_2 transistors are freely suspended between two metallic contacts.

6.2 WS_2

6.2.1 Methods

Transistor structures are fabricated on both SiO_2 and h-BN to measure the properties of the WS_2 in both a high and low defect environment respectively. The devices on

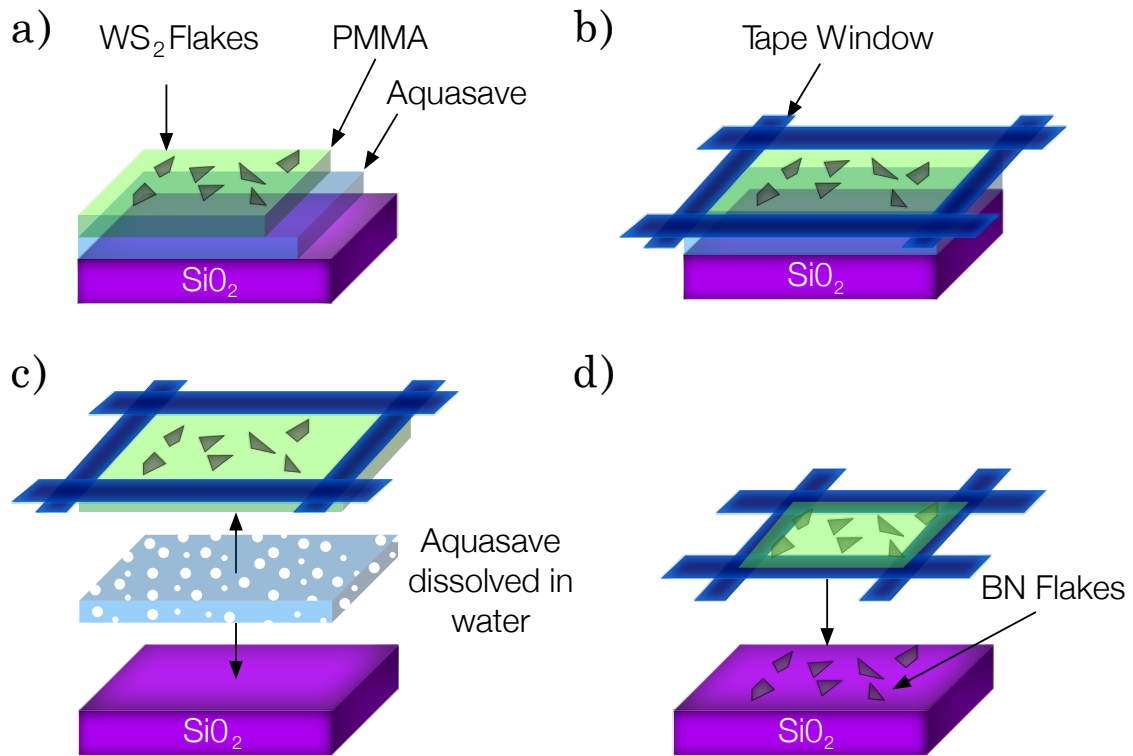


Figure 6.1: The dry transfer process for flakes: **a)** The substrate is prepared by first spinning a water soluble polymer (aquasave) on SiO_2 and then a layer of PMMA. WS_2 flakes are exfoliated onto the PMMA. **b)** A membrane is constructed using tape with a small square hole cut in the centre. The substrate is attached to the tape. **c)** The sample is exposed to water and the aquasave dissolves leaving the PMMA and flakes freely suspended over the hole in the tape. **d)** A second substrate is prepared with boron nitride flakes. The flakes on the membrane can be aligned over the boron nitride using an optical microscope and a height adjustable stage. The substrate is heated to melt the PMMA and complete the transfer process.

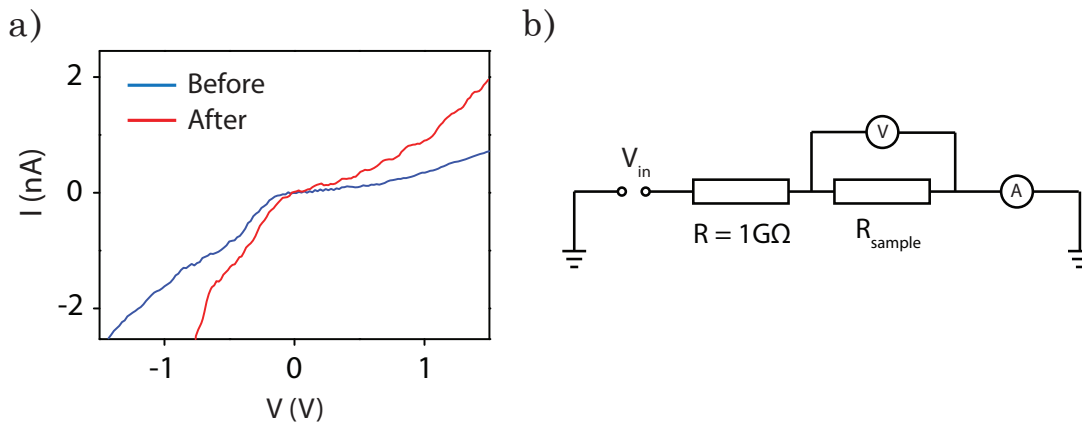


Figure 6.2: a) IV characteristics of a device before and after annealing. b) The circuit setup for annealing, a large $1\text{ G}\Omega$ resistor is placed in series to the device to prevent damage to the flake if the resistance drops sharply.

SiO₂ are fabricated as described in Sec. 3.1.1, to make the h-BN devices a dry transfer method is used to stack the crystals. The process is made possible by a water soluble polymer (aquasave) which is first spin coated onto a Si/SiO₂ substrate. A second layer, of PMMA, is spun on top and subsequently WS₂ flakes are deposited onto the PMMA, Fig. 6.1 (a). The substrate is attached to a piece of tape with a hole cut in the centre, Fig. 6.1 (b). The aquasave is then dissolved in water leaving the PMMA membrane attached to the tape, Fig. 6.1 (c). Flakes of boron nitride are exfoliated on a second Si/SiO₂ substrate; the PMMA membrane can then be aligned under a microscope such that a WS₂ flake is on top of a boron nitride flake. When the two are brought into contact the substrate is heated to melt the PMMA allowing a good contact between the two flakes, Fig. 6.1 (d). For both types of substrate Cr/Au contacts are deposited with a thickness of 5/70 nm respectively. The thickness of the flakes is determined by Raman spectroscopy; the results of which were discussed in Sec. 3.3.2 and compared with results from [9].

Immediately after fabricating the devices it is found that the IV characteristics

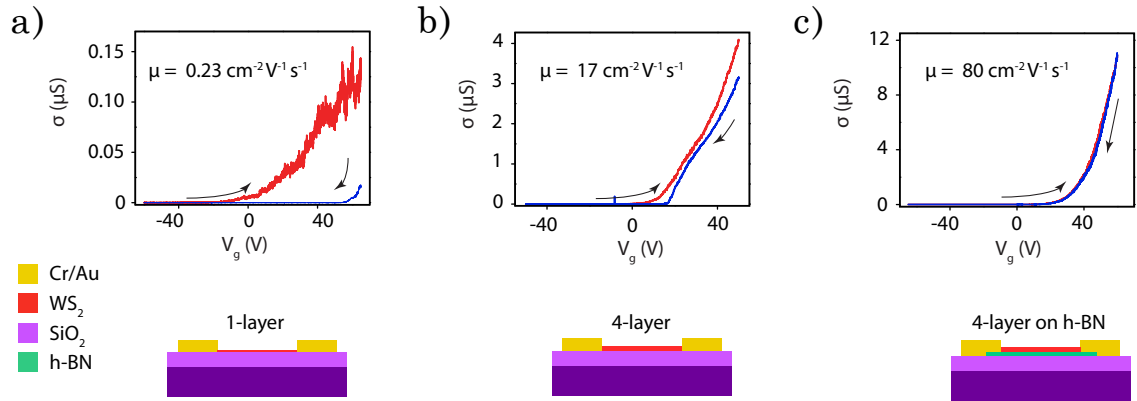


Figure 6.3: Field effect transfer characteristics for **a)** single layer MoS_2 on SiO_2 , **b)** 4-layer MoS_2 on SiO_2 and **c)** 4-layer MoS_2 on h-BN. The device in **c)** has the largest mobility with $\mu = 80 \text{ cm}^{-2}\text{V}^{-1}\text{s}^{-1}$. The mobilities are calculated using the method described in chapter 3.4.2.

are highly non-linear, see the blue curve on Fig 6.2 (a). Annealing as described in Sec. 3.1.3 is employed to improve the quality of the samples, Fig. 6.2 (b) shows the circuit setup for annealing. A high voltage bias (up to 40 V) is applied to the device and on subsequent sweeps a decrease in the resistance of the device is observed, red curve on 6.2 (a). Even after annealing a small Schottky barrier is expected due to the mismatch in the work functions between the chrome contacts and the WS_2 . The annealing process takes place in a ^4He atmosphere and the samples are measured directly after annealing down to temperatures of 4.2 K. If the samples are exposed to air then the non-linear behaviour in the IV curves returns; this suggests that in addition to the Schottky barrier, there may also be a barrier due to oxidation at the interface between the chrome and the WS_2 which is broken down by high voltage bias.

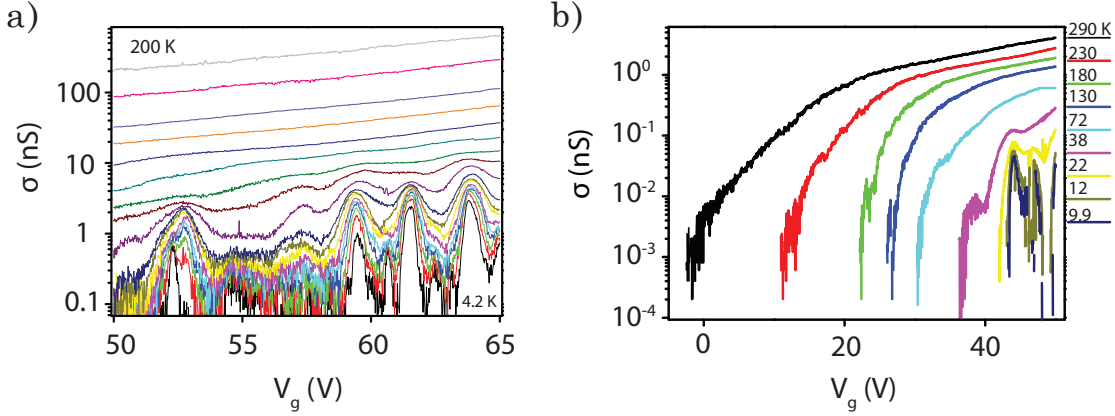


Figure 6.4: **a)** The temperature dependence of $\sigma(V_g)$ for 4-layer WS₂ on h-BN. The temperature range is from 200 K down to 4.2 K over a narrow gate voltage range. **b)** The temperature dependence of $\sigma(V_g)$ for 4-layer WS₂ on SiO₂. An expanded gate voltage range is shown.

6.2.2 Results

Fig. 6.3 displays the room temperature field effect transfer characteristics for (a) monolayer SiO₂/WS₂, (b) 4-layer SiO₂/WS₂ and (c) 4-layer SiO₂/h-BN/WS₂. The mobility of the devices on SiO₂ is always lower than on h-BN and also increases with the number of layers. There is also a large hysteresis in the gate voltage dependence on SiO₂ supported substrates. This can be attributed to the presence of charge traps at the interface with the WS₂ [10, 11]. The device on h-BN does not display any significant hysteresis and so can be said to be largely free of charge traps. The field effect mobility of the devices on h-BN is much larger than on SiO₂; up to two orders of magnitude larger in the extreme cases.

The temperature dependence of the conductivity $\sigma(T)$ for the 4-layer device on h-BN is shown in Fig. 6.4 (a). A narrow gate voltage range is swept, and at a slow speed so that the electronic charge distribution in the device is not changed appreciably from

sweep to sweep. The value of $\sigma(T)$ is suppressed upon lowering the temperature as for semiconductors and there are two different regimes identifiable from the plot. Above 100 K the V_g dependence of the conductance is smooth and increases with V_g ; below 100 K peaks appear in the conductance. These two regimes will be discussed in the section below. A similar behaviour is observed in flakes on a SiO_2 substrate, 6.4 (b) which displays the conductivity for an expanded gate voltage range from 0 V to 50 V.

6.2.3 Discussion

The following analysis will centre on the 4-layer device on h-BN, a semi-log plot of the conductivity for a gate voltage of $V_g = 60.5$ as a function of T^{-1} is shown in Fig. 6.5 (a). The conduction for the high temperature regime down to 100 K can be described by thermally activated transport [12]:

$$\sigma(T) = \sigma_0 \exp(-\delta\epsilon/2k_B T), \quad (6.1)$$

where $\delta\epsilon$ is the activation energy for transport. The activation energy is extracted from the fits in the gate voltage range $50 \text{ V} < V_g < 65 \text{ V}$ and is plotted in 6.5 (b). In this gate voltage range the Fermi energy of the system is shifted close to the conduction band so that the charge carriers are directly injected into the WS_2 from the metal contacts [13]. The extracted energy values of $\delta\epsilon$ are also consistent with voltage bias range associated with the non-linear transport in IV measurements. $\delta\epsilon$ is therefore the energy between the conduction band edge and the Fermi level $\delta\epsilon = E_C - E_F$. The activation energy decreases on average with increasing V_g and there is a smooth dependence suggesting that by sweeping the gate voltage the Fermi level is tuned through sub gap defect states.

To estimate the density of the sub gap states the capacitance of the system can

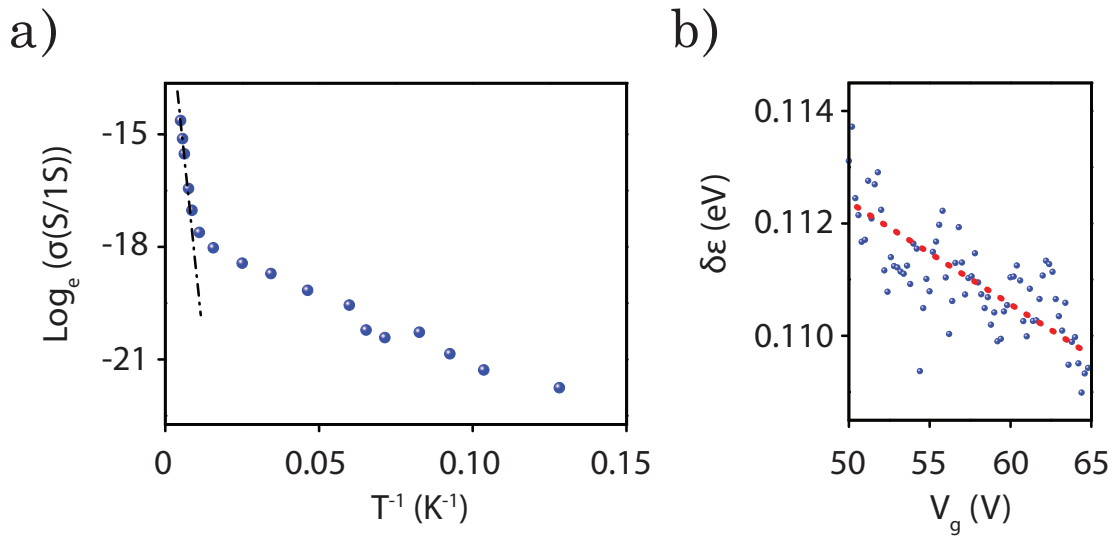


Figure 6.5: Thermally activated transport data: **a)** An Arrhenius plot of the conductivity as a function of T^{-1} for $V_g = 60.5$ V. The fit is consistent with thermally activated transport. The units of S/1S represent a ‘dimensionless conductance’ for purposes of taking a logarithm. **b)** The extracted activation energy for different gate voltages (each point is an average over an 0.2 V range).

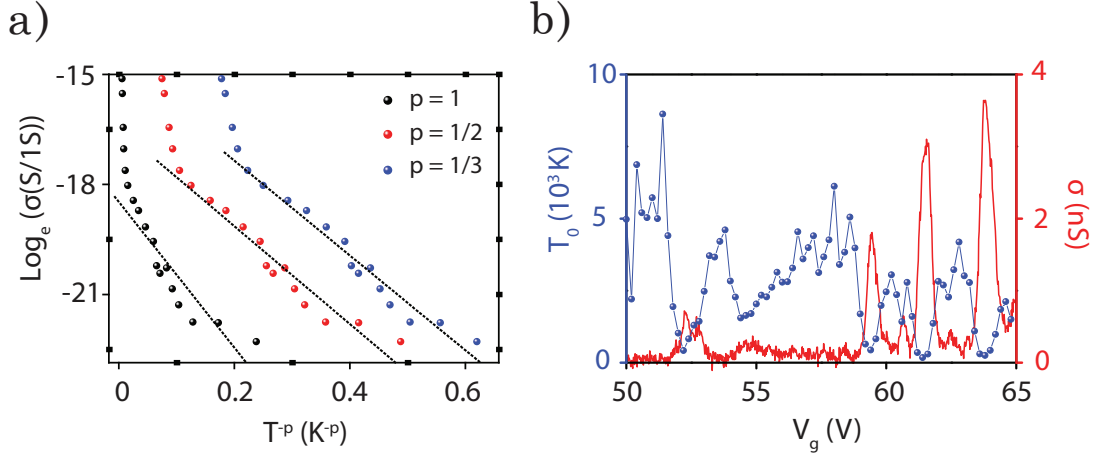


Figure 6.6: a) The $\sigma(T)$ dependence at $V_g = 60.5$ V plotted as a function of T^{-p} , where p takes the value of 1 for NNH, 1/2 for Efros-Shklovskii VRH, 1/3 for Mott VRH in 2D. The best fit was determined to be $p = 1/3$. b) The red curve is a plot of $\sigma(V_g)$ at $T = 4.2$ K; the overlaid blue data points are extracted values of the hopping parameter T_0 .

be modelled as a parallel plate capacitor; the finite density of defect states on the WS₂ ‘plate’ leads to a reduction in the overall capacitance. This can be modelled as two capacitors in series: with the geometrical capacitance per unit area $C_g = \epsilon_0\epsilon_r/d$ determined by the oxide thickness ($d = 280$ nm); and the quantum capacitance per unit area $C_Q = q^2D_c(E)$ related to the density of the defect states $D_c(E)$ [14]. The total capacitance is then related to the shift in the Fermi energy due to the gate voltage extracted from Fig. 6.5 (b) $-dE_F/dV_g = 1.5 \times 10^{-4}e = e\frac{C_gC_Q}{C_g+C_Q}$ [2, 14]. Since the geometrical capacitance is known, the quantum capacitance can be obtained from this relation and is found to be $C_Q = 0.8 \text{ Fm}^{-2}$. This gives an estimate for the density of defect states $D_c(E) = 3.12 \times 10^{37} \text{ J}^{-1}\text{m}^{-2}$.

Fig. 6.6 (a) shows fits for conductivity in the low temperature regime (below 100 K). The data is plotted as a function of T^{-p} with p a critical exponent. For $p = 1$ the fit would describe nearest neighbour hopping and for $p = 1/2$, Efros-Shklovskii variable

range hopping (VRH). However the statistically best fit is found to be $p = 1/3$ which describes non-interacting Mott VRH in 2D as the dominant transport mechanism. As discussed in chapter 2.4.2, the conductivity has a specific temperature dependence given by [12]:

$$\sigma = \sigma_0 \exp \left[(-T_0/T)^{-1/3} \right], \quad (6.2)$$

where $T_0 = \frac{13.8}{k_B D_c \xi^2}$ is the hopping parameter. It is related to the localisation radius of the electron wave function ξ , and the density of states within the forbidden gap D_c . The hopping parameter can be extracted from the temperature dependence and is plotted for the gate voltage range in Fig. 6.6 (b). A conductance trace at 4.2 K is also overlaid, showing a clear correlation between T_0 and peaks in the conductance. The value of the hopping parameter varies from ≈ 100 K to ≈ 4000 K over a narrow gate voltage range (50.5 V to 52 V). Using the previously calculated density of the defect states ($D_c(E)$), ξ can be estimated from the extracted fit values of T_0 . ξ increases from 1.8 nm in regions of low conductance up to 17 nm where there are peaks in the conductance. This can be interpreted as sub gap impurity states having a narrow bandwidth of energy within the gap.

The differential conductance as a function of source drain bias and gate voltage at 4.2 K is shown in the top panel of Fig. 6.7 (a). The positions of the peaks shift, with the application of a source drain bias as can be seen in the inset for Fig. 6.7 (a). This suggests that the sub gap transport occurs through inhomogeneous charge puddles and localised states in the WS₂. Coulomb blockade can be ruled out as the origin of the peaks in the $\sigma(V_g)$ data. The associated charging energy estimated from the stability diagram would be around $E_C = 40 - 50$ meV with a diameter of $d \sim \frac{e^2}{4\epsilon_0\epsilon_r E_C} \sim 20 - 40$ nm. The dimensions of the 4-layer WS₂ sample on h-BN ($L =$

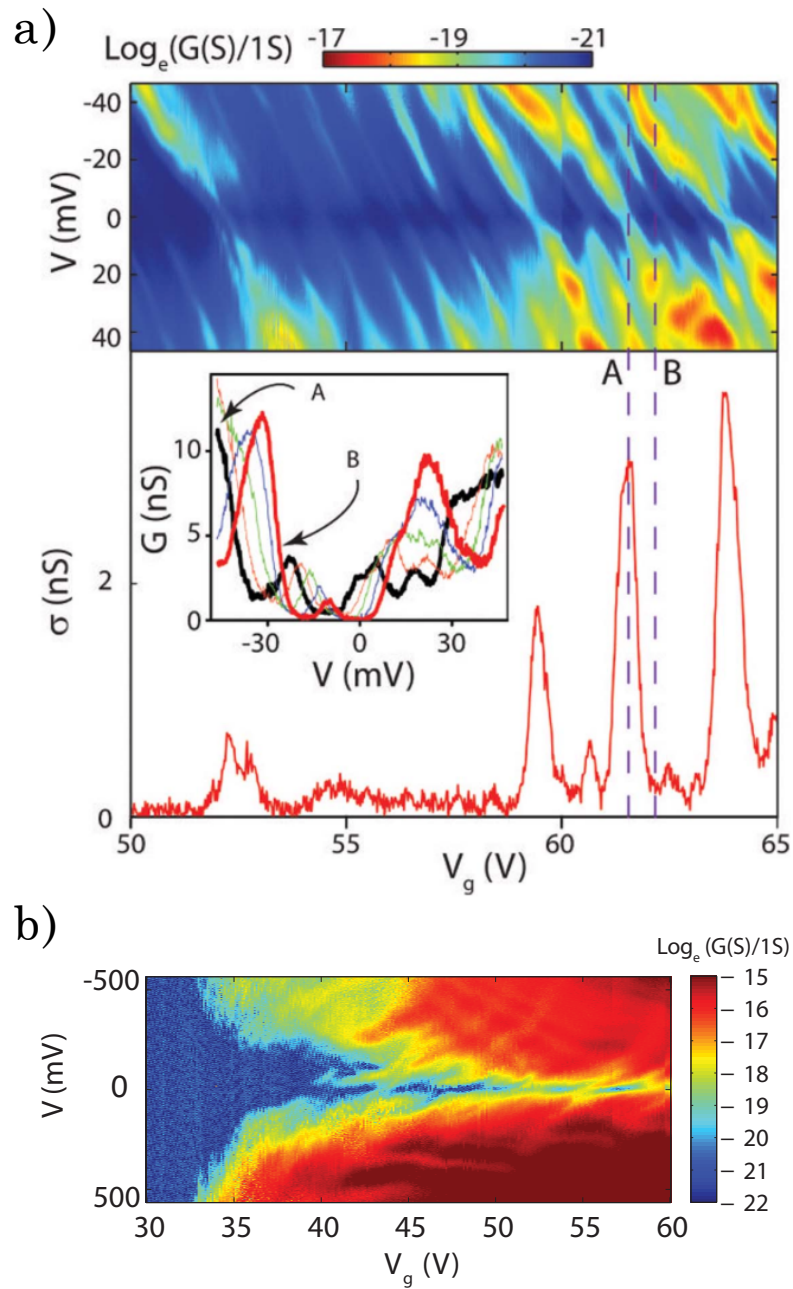


Figure 6.7: a) 4-layer WS_2 on h-BN. Top panel: A stability diagram of the differential conductance as a function of source drain voltage and gate voltage at $T = 4.2$ K. Bottom panel: $\sigma(V_g)$ at $T = 4.2$ K. Inset: Conductance traces as a function of source drain voltage, from the regions labeled A (61.5 V) up to B (62 V) on the main panel. b) 4-layer WS_2 on SiO_2 , differential conductance as a function of source drain voltage and gate voltage at $T = 4.2$ K

350 nm \times $W = 1500$ nm) would encompass many charging regions of diameter d , with $(L * W/d)$ corresponding to around 100 – 1000 charging regions. This would manifest itself as many overlapping Coulomb diamonds in the stability diagram which were not observed in the measurements. An origin for the conductance peaks is hinted at by noting that they decrease in amplitude for temperatures below ~ 20 K, this behaviour has been observed in other semiconducting systems [15, 16] and describes inelastic tunnelling through the sub gap impurity states in the WS₂. The low temperature transport behaviour presented in this section was observed in other flakes regardless of the aspect ratio of the flakes; the number of layers of WS₂; and the dielectric environment as seen in Fig. 6.7 (b) which shows a similar stability diagram for a 4-layer WS₂ on SiO₂. It is clear then that the impurity states that contribute to the conductance in WS₂ on h-BN are intrinsic to the crystal itself; therefore in a defected dielectric environment such as SiO the conductivity will be determined by the intrinsic impurities in addition to the charge traps that exist at the dielectric interface.

6.3 MoS₂

The low temperature conductivity in MoS₂ on SiO₂ has been well studied [1, 2], with claims that the transport is due to resonant tunnelling through localised states that arise from the SiO₂ charge trap states. To expand upon the previous argument for WS₂, flakes of MoS₂ are freely suspended to investigate the electrical transport properties in absence of any substrate. The suspension method used was with HF acid as described in Sec. 3.1.2 and a false colour SEM image of a typical device is shown in Fig. 6.8 (a).

The temperature dependence of $I(V_g)$ was measured for a monolayer device in the gate voltage range 0 V to 50 V, Fig 6.8 (b). The current decreases with temperature, corresponding to a decrease in the conductivity and the extracted mobilities plotted in

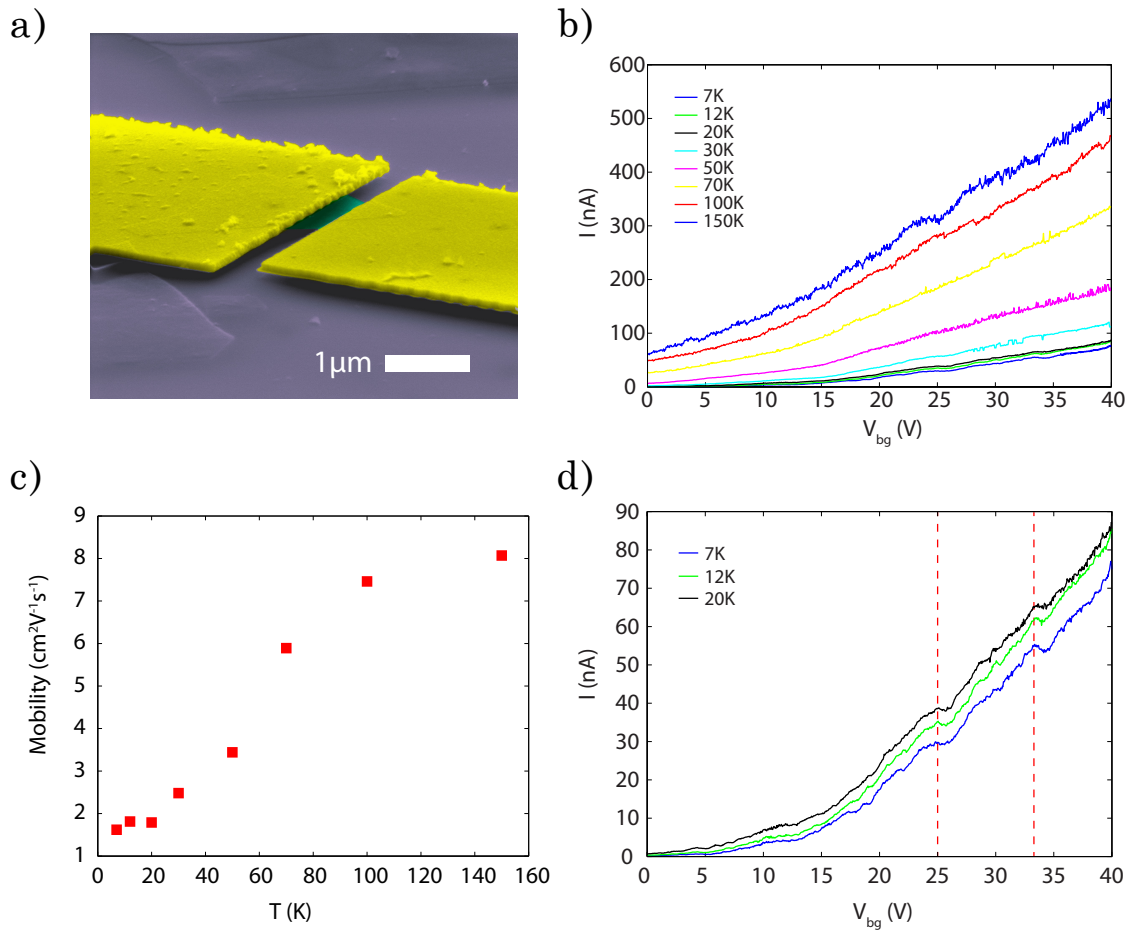


Figure 6.8: Suspended MoS_2 : **a)** A false colour SEM image of a suspended MoS_2 flake: purple is the etched SiO_2 ; yellow is the Au contacts; and green is the flake. **b)** An overview of the field effect transfer characteristic for a range of temperatures. The device is biased at $V_{SD} = 500$ mV. **c)** Mobility values extracted from the $I(V_g)$ curves at different temperatures. **d)** A closer look at the low temperature $I(V_g)$ curves. There appears to be repeatable features up to 20 K, two of which are identified by the dashed lines.

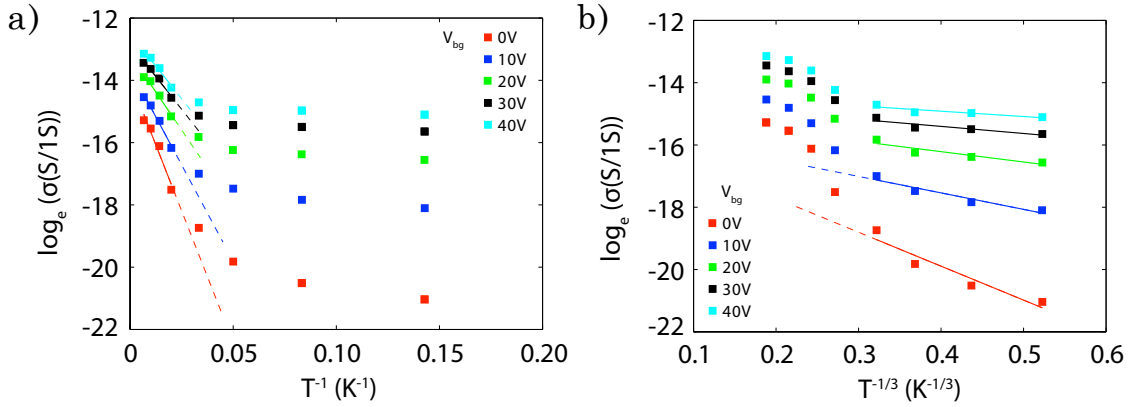


Figure 6.9: Hopping data: **a)** The conductivity data for different gate voltages plotted in terms of thermally activated transport (T^{-1}). Dashed lines are a guide for the eyes to see where the data deviates from the fit. **b)** Conductivity data for different gate voltages plotted in terms of Mott VRH ($T^{-1/3}$).

Fig 6.8 (c) drop from $\sim 8 \text{ cm}^2\text{V}^{-1}\text{s}^{-1}$ at 150 K to $\sim 1.5 \text{ cm}^2\text{V}^{-1}\text{s}^{-1}$ at 7 K. A closer look at the low temperature regime ($< 20 \text{ K}$), Fig 6.8 (c) reveals similar features as compared to the WS₂ devices, there are some small peaks in $I(V_g)$ that appear at recurrent gate voltages for each temperature. However the onset for non-interacting Mott VRH is at a much lower temperature, around 20 K as opposed to 100 K for the WS₂. Fig. 6.9 (a) shows that the conductivity can be described as thermally activated transport down to $\sim 20 \text{ K}$ fitted by Eqn. 6.1 while Fig. 6.9 (b) is a fit to Mott VRH, Eqn. 6.2 for temperatures below $\sim 20 \text{ K}$. To convincingly argue this point for the MoS₂ sample and obtain a more accurate fit; additional data over the specified temperature ranges are required.

6.4 Conclusions

The low temperature transport properties of MoS_2 and WS_2 have been measured in a substrate free environment and on a low impurity dielectric environment respectively to determine the intrinsic nature of the charge carriers. WS_2 transistors on h-BN display a higher mobility than devices on SiO_2 and also do not exhibit a hysteresis in the field-effect transfer characteristics which indicates a lack of charge traps at the interface between the WS_2 and h-BN. At high temperatures in the range $100\text{ K} < T < 200\text{ K}$ the charge carriers in WS_2 are thermally activated and below 100 K they contribute to the conduction by Mott VRH. The suspended MoS_2 exhibits thermally activated transport down to $\sim 20\text{ K}$ and Mott VRH below. In both materials in the Mott VRH regime there is the appearance of peaks to the conductance. These correspond to narrow bands of defect states within the band gap as seen by an increase in the size of the electron wave function localisation radius when the Fermi level is swept through the bands. The presence of the impurity states in MoS_2 and WS_2 in the absence of a disordered environment leads to the conclusion that the impurity states are intrinsic to the crystals. This could be due to sulphur vacancies [17]. Recently the quality of CVD grown MoS_2 has been shown to be improved by annealing in a sulphur atmosphere [18], it may also be possible to improve the quality of exfoliated flakes from mined crystals in this way.

Bibliography

- [1] S. Ghatak, A. N. Pal, and A. Ghosh, *ACS Nano* **5**, 7707 (2011).
- [2] A. Ayari, E. Cobas, O. Ogundadegbe, and M. S. Fuhrer, *Journal of Applied Physics* **101**, (2007).
- [3] W. Bao, X. Cai, D. Kim, K. Sridhara, and M. S. Fuhrer, *Applied Physics Letters* **102**, (2013).
- [4] B. Radisavljevic, A. Radenovic, J. Brivio, V. Giacometti, and A. Kis, *Nat Nano* **6**, 147 (2011).
- [5] K. Kaasbjerg, K. S. Thygesen, and K. W. Jacobsen, *Phys. Rev. B* **85**, 115317 (2012).
- [6] K. Bolotin, K. Sikes, Z. Jiang, M. Klima, G. Fudenberg, J. Hone, P. Kim, and H. Stormer, *Solid State Communications* **146**, 351 (2008).
- [7] C. R. Dean, A. F. Young, I. Meric, C. Lee, L. Wang, S. Sorgenfrei, K. Watanabe, T. Taniguchi, P. Kim, and K. L. Shepard and J. Hone, *Nat Nano* **5**, 722 (2010).
- [8] G.-H. Lee, Y.-J. Yu, C. Lee, C. Dean, K. L. Shepard, P. Kim, and J. Hone, *Applied Physics Letters* **99**, (2011).

-
- [9] A. Berkdemir, H. R. Gutierrez, A. R. Botello-Mendez, N. Perea-Lopez, A. L. Elias, C.-I. Chia, B. Wang, V. H. Crespi, F. Lopez-Urias, J.-C. Charlier, et al., *Sci. Rep.* **3** (2013).
- [10] P. Shah, M. Amani, M. Chin, T. O'Regan, F. Crowne, and M. Dubey, *Solid-State Electronics* **91**, 87 (2014).
- [11] D. J. Late, B. Liu, H. S. S. R. Matte, V. P. Dravid, and C. N. R. Rao, *ACS Nano* **6**, 5635 (2012).
- [12] B. I. Shklovskii and A. L. Efros, *Electronic Properties of Doped Semiconductors*, vol. Vol. 45 (Springer Series in Solid State Sciences, Berlin, 1984).
- [13] S. Das, H.-Y. Chen, A. V. Penumatcha, and J. Appenzeller, *Nano Letters* **13**, 100 (2013).
- [14] D. K. Schroder, *Semiconductor Material and Device Characterization, 3rd Edition* (Wiley-IEEE Press, 2006).
- [15] A. Yakimov, N. Stepina, and A. Dvurechenskii, *Physics Letters A* **194**, 133 (1994).
- [16] A. K. Savchenko, V. V. Kuznetsov, A. Woolfe, D. R. Mace, M. Pepper, D. A. Ritchie, and G. A. C. Jones, *Phys. Rev. B* **52**, R17021 (1995).
- [17] H.-P. Komsa, S. Kurasch, O. Lehtinen, U. Kaiser, and A. V. Krasheninnikov, *Phys. Rev. B* **88**, 035301 (2013).
- [18] K.-K. Liu, W. Zhang, Y.-H. Lee, Y.-C. Lin, M.-T. Chang, C.-Y. Su, C.-S. Chang, H. Li, Y. Shi, H. Zhang, et al., *Nano Letters* **12**, 1538 (2012).

Chapter 7

Conclusions and proposals for future work

While this thesis is called ‘Two dimensional atomically thin materials and hybrid superconducting devices’, it has barely scratched the surface of what this topic could entail. To summarise the results of the thesis, fluorinated graphene has been successfully demonstrated as a beta radiation detector. A device was made from mechanically exfoliated fluorinated graphene; it showed a rapid decrease in resistance upon initial exposure to beta radiation; from 20 G Ω to 2 G Ω in only 2 hours. The process causing the decrease in resistance is attributed to a breaking of the carbon-fluorine bonds which reduces the sp^3 hybridised structure of the FG back into the sp^2 hybridised structure of pristine graphene. The beta radiation is not thought to damage the graphene; this is ruled out by exposing a pristine graphene device and noting that the IV characteristics do not change even after exposure for 12 hours. A CVD grown graphene sheet was fluorinated and transferred to a transparent, flexible substrate. Such a device could find a use as a personal dosimeter or embedded within food packaging to confirm the safety product.

Molybdenum rhenium has been shown to have a high transition temperature $T_C = 7.5$ K and a high critical field of ~ 8 T. These features could allow the possibility to explore a system where superconductivity and the quantum Hall effect coexist at the same time. Previous work on such a system with graphene as a weak link used niobium for contacts. The critical field in this system was found to be ~ 4 T [1, 2], MoRe may prove to be a better choice of superconductor for such an experiment.

MoRe displays a resistance to hydrofluoric acid, allowing the suspension of graphene between two superconducting electrodes. The mechanical properties of graphene have never been explored in the superconducting regime. The ability to anneal suspended devices to achieve higher mobilities may also enhance the superconducting proximity effect. On supported devices a proximity induced super current was measured in MoRe-Graphene-MoRe Josephson junction of up to 200 nA. However it required a temperature of $T = 30$ mK and a gate voltage of 50 V to shift the Fermi level away from the neutrality point. The fully developed super current was not seen in charge neutral graphene, this was explained by the de-phasing of the injected electrons from the superconductor at the boundaries between electron and hole puddles. The Josephson super current was also not seen at higher temperatures, this suggests that the interface between the graphene and the superconductor are not fully transparent and so further work should look into improving this interface. If these factors can be overcome then the experiments mentioned briefly in chapter 1, involving the Cooper pair splitter and the Josephson quantum electron pump may be viable.

Finally the temperature dependence of the conductivity is measured for suspended MoS₂ and for WS₂ on a hexagonal boron nitride substrate. WS₂ transistors on h-BN display a higher mobility than devices on SiO₂ and also do not exhibit a hysteresis in the field-effect transfer characteristics. This indicates a lack of charge traps at the interface

between the WS₂ and h-BN. At high temperatures the dominant hopping mechanism contributing to the conductivity in both MoS₂ and WS₂ is thermally activated with temperature dependence T^{-1} . At low temperature the conductivity is dominated by Mott variable range hopping with the temperature dependence $T^{-1/3}$ for 2D transport. The presence of the impurity states in MoS₂ and WS₂ in the absence of a disordered environment leads to the conclusion that the impurity states are intrinsic to the crystals; the impurities could be due to sulphur vacancies [3]. The quality of CVD grown MoS₂ has been shown to be improved by annealing in a sulphur atmosphere [4], it may also be possible to improve the quality of exfoliated flakes from mined and CVD grown crystals in this way.

Bibliography

- [1] P. Rickhaus, M. Weiss, L. Marot, and C. Schönenberger, *Nano Letters* **12**, 1942 (2012).
- [2] K. Komatsu, C. Li, S. Autier-Laurent, H. Bouchiat, and S. Guéron, *Phys. Rev. B* **86**, 115412 (2012).
- [3] H.-P. Komsa, S. Kurasch, O. Lehtinen, U. Kaiser, and A. V. Krasheninnikov, *Phys. Rev. B* **88**, 035301 (2013).
- [4] K.-K. Liu, W. Zhang, Y.-H. Lee, Y.-C. Lin, M.-T. Chang, C.-Y. Su, C.-S. Chang, H. Li, Y. Shi, H. Zhang, et al., *Nano Letters* **12**, 1538 (2012).